Design and Analysis of Optimal Ascent Trajectories for Stratospheric Airships

A DISSERTATION

SUBMITTED TO THE FACULTY OF THE GRADUATE SCHOOL

OF THE UNIVERSITY OF MINNESOTA

BY

Joseph Bernard Mueller

IN PARTIAL FULFILLMENT OF THE REQUIREMENTS

FOR THE DEGREE OF

Doctor of Philosophy

Professor Yiyuan J. Zhao

August, 2013

Acknowledgements

Without a doubt, I have been blessed with amazing opportunities and extraordinary people in my life. The *pursuit* of this Ph.D. has been an endeavor that has pushed my limits in many ways. I am grateful for the opportunity and for the people who have helped me along the way.

I would first like to extend my sincere gratitude to my advisor, Professor Yiyuan Zhao. When I met Yiyuan in 1995 as a student in his Flight Mechanics course, he immediately stood out to me as a deeply intelligent, thoughtful, and above all, compassionate person. Several years after I graduated, it was Yiyuan who encouraged me to pursue a Ph.D. His belief in me was contagious, and for that I am truly thankful. His guidance, insight and patience have been instrumental to my growth as a student, and are greatly appreciated.

My thanks also go to Professor William Garrard. He has served as a second advisor to me throughout this program, and has been a mentor to me for many years. I sincerely appreciate his guidance, his sage advice, and the many opportunities that he has given.

I extend my thanks to all of my committee members, including Professor Mihailo Jovanovic and Professor Demoz Gebre, for their time and valuable feedback.

Thanks go to all of the people and organizations that contributed to the funding of this research. This includes our Aerospace Engineering Department, the National Science Foundation, the Minnesota Space Grant, and the Doctoral Dissertation Fellowship program.

Thanks to my colleagues at Princeton Satellite Systems, for their support and encouragement as I worked towards this degree.

Thanks to my family and friends for their constant support and faith. My parents and siblings have always been a source of strength, which has helped me more than they know.

And finally, I am deeply grateful to my wife, Jessica, and to our three children. Their sacrifice and loving support over the last several years has humbled me. I will carry this gratitude with me always.

Dedication

This thesis is dedicated to my wife, Jessica, and to my three children, Allison, Dominick and Austin. You renew my strength and give me joy.

Abstract

Stratospheric airships are lighter-than-air (LTA) vehicles that have the potential to provide a long-duration airborne presence at altitudes of 18-22 km. Designed to operate on solar power in the calm portion of the lower stratosphere and above all regulated air traffic and cloud cover, these vehicles represent an emerging platform that resides between conventional aircraft and low Earth-orbiting (LEO) satellites.

A particular challenge for airship operation is the planning of ascent trajectories, as the slow moving vehicle must traverse the high wind region of the jet stream. Due to the large changes in wind speed and direction across altitude and the susceptibility of airship motion to wind, the trajectory must be carefully planned, preferably optimized, in order to ensure that the desired station be reached within acceptable performance bounds of flight time, energy consumption, and lateral excursion. This thesis develops optimal ascent trajectories for stratospheric airships, examines the structure and sensitivity of these solutions, and presents a strategy for onboard guidance.

Optimal ascent trajectories are developed that utilize wind energy to achieve minimum-time and minimum-energy flights. The airship is represented by a three-dimensional point mass model, and the equations of motion include aerodynamic lift and drag, vectored thrust, added mass effects, and accelerations due to mass flow rate, wind rates, and Earth rotation. A representative wind profile is developed based on historical meteorological data and measurements. Trajectory optimization is performed by first defining an optimal control problem with both terminal and path constraints, then using direct transcription to develop an approximate nonlinear parameter optimization problem of finite dimension. Optimal ascent trajectories are determined using SNOPT for a variety of upwind, downwind, and crosswind launch locations. Results of extensive optimization solutions illustrate definitive patterns in the ascent path for minimum time flights across varying launch locations, and show that significant energy savings can be realized with minimum-energy flights, compared to minimum-time time flights, given small increases in flight time.

The performance of the optimal trajectories are then studied with respect to solar energy production during ascent, as well as sensitivity of the solutions to small changes in drag coefficient and wind model parameters. Results of solar power model simulations indicate that solar energy is sufficient to power ascent flights, but that significant energy loss can occur for certain types of trajectories. Sensitivity to the drag and wind model is approximated through numerical simulations, showing that optimal solutions change gradually with respect to changing wind and drag parameters and providing deeper insight into the characteristics of optimal airship flights.

Finally, alternative methods are developed to generate near-optimal ascent trajectories in a manner suitable for onboard implementation. The structures and characteristics of previously developed minimum-time and minimum-energy ascent trajectories are used to construct simplified trajectory models, which are efficiently solved in a smaller numerical optimization problem. Comparison of these alternative solutions to the original SNOPT solutions show excellent agreement, suggesting the alternate formulations are an effective means to develop near-optimal solutions in an onboard setting.

Contents

3 Modeling 10

List of Tables

List of Figures

Chapter 1

Introduction

1.1 Airships

Using buoyancy as the primary source of lift, airships are essentially controllable balloons. The first airship flights date back to the middle and late 19th century. Today, new airship designs boast lighter materials and more powerful engines, but the basic principles remain the same.

The hull of the airship is filled with a light gas, making the entire vehicle lighter-than-air. While the density of the vehicle is less than that of the surrounding atmosphere, the vehicle rises. This continues until the "pressure altitude" is reached, where the two densities are equal. Modern airships use a pressure regulation system, filling internal bags called ballonets with air at low altitudes. This equivalently regulates the vehicle density to be close to that of the ambient air, enabling controlled flight anywhere between the ground and pressure altitude [1].

Historically, airship structural designs have fallen into three general categories, based on the type of hull: rigid, semi-rigid, and non-rigid [1]. In rigid designs, like the German Zeppelins, the hull is composed of a solid structure. Airships with non-rigid hulls are also referred to as pressurized airships, because the flexible hull requires a slightly higher (about 1%) internal pressure to maintain its shape. A semi-rigid airship has a pressurized hull along with some additional internal structure. In order to maintain the stratospheric altitude of $20 - 22$ km with buoyancy, the airship must be designed with an overall vehicle density of $0.06 - 0.08$ kg/m^3. This requires the hull surface density to be extremely low, so that only pressurized, non-rigid designs remain viable. This is evidenced in recent work by Lee [2] and Schmidt [3, 4].

1.2 Applications of Stratospheric Airships

With the capability to maintain a fixed geographic station at much lower altitudes than LEO or geostationary satellites, the stratospheric airship has the potential to provide improved performance for a variety of long-term missions: wireless telecommunications service; remote sensing for weather monitoring and general scientific study; and imaging surveillance for traffic, border security, military operations and search and rescue missions. The recognition of this potential is evident in the recent widespread research and development of stratospheric airship platforms by academic, military and industrial institutions around the world.

In 2008, the Missile Defense Agency (MDA) contracted with Lockheed Martin to design and build unmanned airships to be operated continuously at high altitudes around the U.S. coastline for missile defense. In 2006, Edwards Air Force Base issued research studies to evaluate the use of high-altitude airships to perform data relay functions between the ground station and aircraft, which would replace an expensive ground-based network of microwave antennas. DARPA has an ongoing program called ISIS (Integrated Sensor is Structure), in which stratospheric airships are being developed as an imaging and surveillance platform.

1.3 Challenges in Airship Trjajectory Planning

Because they operate in the low density region of the stratosphere, airships must displace a large volume of air to achieve neutral buouyancy. The resulting design requires a large helium-filled hull, which can nonetheless be utilized for harnessing solar energy by the integration of thin-film solar cells along the top and sides [5, 3]. Recent advances in lightweight materials and energy storage technologies have sparked serious interest in the stratospheric airship concept [6]. Several institutions have developed low and mid-altitude prototypes or testbeds [7, 2]. In recent years, numerous studies have been performed on airship design and feasibility [8, 9, 5, 10, 3, 4], and a variety of methods have been proposed for trajectory tracking and feedback control design [11, 12, 13, 14, 15]. This widespread interest is reflective of the potential benefits in performance and cost that airships can offer over alternative systems.

The unique attributes of the airship also create some inherent challenges in their design and operation. With a large surface area to mass ratio, the airship flight dynamics are strongly influenced by the wind. The success of long-endurance station-keeping missions hinges on the ability of the airship to generate and store more energy than it consumes on a daily basis. This places challenging requirements on the design and construction of the vehicle, and also requires that the airship plan and follow energy efficient flight trajectories.

A particular challenge for airship operation is the planning of ascent trajectories. Indeed, the slow moving vehicle must traverse the high wind region of the jet stream. Due to the large changes in wind across altitude and the susceptibility of airship motion to wind, the trajectory must be carefully planned, preferably optimized, in order to ensure that the desired station be reached within acceptable performance bounds of flight time, energy consumption, and lateral excursion. However, very few studies have been conducted in this area to date.

Furthermore, airships fly at much lower airspeeds than traditional fixed-wing aircraft, which reduces maneuverability, and they are restricted by stringent constraints on thrust, power, and rate of climb. These unique flight characteristics combined with the mission-critical nature of the airships flight capabilities lead to an important new problem: to develop optimal flight plans for autonomous airships that incorporate knowledge of the current wind conditions.

1.4 Research Contributions

The aim of this thesis is to present the a complete study of modeling, optimization and guidance for stratospheric airships. The main contributions are as follows:

- The development and characterization of optimal ascent trajectories for stratospheric airships for minimum-time and minimum-energy flights
- Sensitivity analysis of optimal solutions with respect to variations in drag and wind model characteristics
- Modeling of solar irradiance exposure during ascent flights that account for time of day, time of year, geographic latitude, altitude, and inertial orientation of the airship.
- Modeling of predicted wind profiles that are suitable for use in trajectory planning
- The development of an ascent guidance method that is amenable for onboard implementation. This method enables computationally efficient re-planning of the optimal trajectory subject to changes in the predicted wind profile.

In this paper, I conduct a systematic study of optimal ascent trajectories of stratospheric airships. I first develop a dynamic model of the airship that is suitable for trajectory optimization studies. I then develop a problem formulation and consider the scenario of fixed initial and final positions, which illustrates the range of solutions between minimum-time and minimum-energy flights. I then extend this formulation to study optimal trajectories over a range of initial conditions. This provides crucial insights into the effect of wind gradients, and reveals a general strategy for selecting the launch location.

1.5 Organization

The dissertation is organized as follows:

- Chapter 2 discusses previous work related to the topics of airship guidance and control.
- Chapter 3 defines the airship equations of motion and environmental models used for planning.
- Chapter 4 develops the optimal control problem formulations.
- Chapter 5 discusses the numerical solution methods that are used to solve the optimal control problems.
- Chapter 6 presents the numerical solution results.
- Chapter 7 provides an analysis of the optimal solutions in the context of closed-loop simulations.
- Chapter 8 discusses robust planning techniques to mitigate the effects of uncertain wind conditions.
- Chapter 9 presents the conclusions of this work.
- Chapter 10 discusses recommendations for future research.

Chapter 2

Related Work

2.1 Overview

Although airships have been flying for over 100 years, the concept of autonomous airships sustained at high altitudes has only emerged in the last 10-15 years. Prior research has focused on high-level feasibility and sizing studies [3, 2], models of seasonal wind patterns and solar power [2], vehicle dynamics modeling and feedback control design [16]. Only a few instances of optimal flight planning for any type of airship appear in the literature [16, 2, 17]. In 2004, Zhao et. al. [16] was the first to explore optimal flight planning for stratospheric airships. In 2009, Mueller et. al. [17] developed optimal ascent trajectories for a range of flight objectives and launch geometries.

2.2 Design and Feasibility Studies

Stratospheric airships represent an extremely challenging systems engineering design problem. In order to remain neutrally buoyant at 65,000 feet, the overall vehicle density must be less than that of the sparse atmosphere at that high altitude, which is just 0.09 kg/m^3. Development of lightweight materials has therefore been a key technology driver. In addition, their intended application as a long endurance platform requires a renewable energy source, typically thin-film solar cells, and high energy-density systems for energy storage. As a result of these core technical challenges, several design and feasibility studies have been conducted to explore the potential of various high-altitude airship configurations.

In [8], the authors applied shape optimization techniques to develop low-drag contours for airship hulls. [10] developed a dual-hull configuration which uses only thrust vectoring control to regulate pitch and yaw motion, with roll passively stabilized. In [5], a general sizing and feasibility assessment for high-altitude airships was conducted. A model of the power and propulsion system was developed and wind profiles at U.S. east and west coasts were evaluated for different seasons to derive vehicle sizing and power system requirements. The author later studied the feasibility of airships for exploration of other planets and moons [18]. A comprehensive study of station-keeping requirements for a notional high-altitude airship was presented in [3, 4]. The authors evaluated wind data over selected geographic regions, developed a model to compute available power, and used the wind data to derive power requirements. The study identified limitations with the use of time-averaged power analysis, and concluded that insufficient power-available conditions can occur when wind speeds peak during the sun-abated winter months.

2.3 Feedback Control Methods for Airships

The problem of feedback control for airships deals primarily with rejection of wind disturbances and trajectory tracking. A number of different feedback control methods have been developed for airships in recent years. Although the vehicle size, control actuators, and flight envelope may be different for each case, the fundamentals of the control problem remains the same.

A popular method used by many authors is that of back-stepping control. In this method, a recursive control design strategy is employed that ultimately provides desired characteristics to the closed-loop system. [15] developed reduced-order models across multiple phases of flight and developed feedback control laws with back-stepping methods. [19] also applied a back-stepping control design, and focused on the airship hover stabilization problem, using a quaternion formulation for the kinematic equations. In [11], a back-stepping approach was again used, and global asymptotic stability is shown with Lyapunov methods.

Several other methods have also been used. In [14], a simple proportional feedback law was used to control speed, altitude and ground-track errors, and a rapidly exploring random tree method is used to verify algorithm performance subject to bounded wind disturbances. [20] presented a study of dynamic inversion, back-stepping, and sliding mode control techniques applied to global non-linear control of autonomous airships. [12] generated dynamically feasible trajectories for airships in which preliminary 3D trajectories for the point mass were created, and open-loop controls required to track the trajectory were then derived from the dynamic constraints. [4] used loop-shaping methods to develop inner and outer loop control laws for a notional high-altitude airship configuration. A detailed investigation of turbulence and wind-gust effects on control performance was performed, which found a significant increase in the control power.

2.4 Trajectory Planning Methods for Airships

Although numerous feedback control methods for airships are found in the literature, relatively few studies have been conducted for airship trajectory optimization.

Ref. [21] generates paths of minimum distance that follow a prescribed set of waypoints, subject to kinematic constraints, and Ref. [22] computes helices as candidate paths for ascent that maintain trim conditions. However, neither of these studies account for the wind. In Ref. [23], minimum energy and minimum time trajectories are computed using a wind model of stacked homogeneous layers. This approach ignores the dynamics of the vehicle, assuming only vertical control is used to enable the airship to traverse between wind layers, with horizontal motion governed completely by the wind.

In Ref. [16], optimal control problems were formulated for selected scenarios using a three degree-of-freedom (DOF) point mass model [24], and numerical solutions were developed to find optimal trajectories in the presence of horizontal winds. While representing the first work of this type, this initial study was limited in scope to high-altitude station transitions and station-keeping. In a recent paper [2], optimal ascent trajectories were designed for the Korean stratospheric airship, with both minimum-time and minimum-energy solutions, and the enforcement of a convex horizontal excursion constraint to keep the flight path within national borders. It is one of the few comprehensive publications of a stratospheric airship model, incorporating wind-tunnel test data, CFD analysis, and prototype flight data. However, it also has some important restrictions; namely, it does not consider the possibility of open initial or final positions, and it defines a performance index for the minimum-energy case that does not reflect the true energy consumption of the vehicle.

Chapter 3

Modeling

3.1 Fundamentals of Airship Operation

While the airship does share many common attributes with traditional aircraft, several properties are fundamentally different. The unique properties of airships must be understood in order to develop meaningful models and problem formulations.

The buoyancy force acting on the airship is equivalent to the weight of displaced air, so

$$B = U_H \rho(h) g$$

where U_H is the entire volume of the airship, and $\rho(h)$ is the altitude-dependent atmospheric density. The weight of the airship is

$$W = [m_0 + m_a(h)]g$$

where m_0 includes the mass of the solid airship structure, payload and Helium, while $m_a(h)$ represents the changing mass of air inside the ballonets.

In order to achieve static buoyancy, or zero net lift, the air mass inside the airship must change with altitude according to:

$$m_a(h) = U_H \rho_a(h) - m_0 \tag{3.1}$$

The ceiling altitude, or pressure altitude, occurs when the ballonets fully deflate, at which $m_a(h) = 0$, or

$$\rho_a(h) = m_0/U_H$$

The rate at which air enters or leaves the ballonets is constrained by the capabilities of the fans in the pressure regulation system. This translates into imposed limits on the rate of ascent or descent, in order to maintain neutral buoyancy. I make the assumption that neutral buoyancy is maintained throughout the flight. This is standard practice for pressurized airship configurations, which were briefly introduced in Section 1.1. By maintaining neutral buoyancy, the airship can hover at any altitude, with the capability to change altitude through forward flight. The pressure regulation system expels air from the ballonets during ascent to become lighter with the lightening air. Similarly, it draws air into the ballonets during descent to become heavier. Thus, the maximum attainable rate of climb with neutral buoyancy depends upon the achievable volume flow rate of the pressure system.

In addition, the required thrust and power change with flight condition, according to:

$$\begin{aligned} T_{req} &= D = \frac{1}{2}\rho(h)V^2U_H^{2/3}C_{Do} \qquad (3.2) \\ P_{req} &= \frac{T_{req}V}{\eta} \qquad (3.3) \end{aligned}$$

where $q = \frac{1}{2}\rho(h)V^2$ is the dynamic pressure, $S_{ref} = U_H^{2/3}$ is the standard aerodynamic reference area for airships, and η is the combined efficiency of the propeller and motor.

3.2 Baseline Design

The baseline airship design used for all subsequent analysis is a semi-rigid configuration with a pressurized hull and additional structure for housing the payload and onboard systems, which include avionics, propulsion, power generation, and energy storage. In these configurations, the pressure regulation system causes the vehicle density to closely match the ambient density, so that the net static lift is nearly zero. In other words, the buoyancy force closely matches the weight throughout the flight envelope.

The baseline design configuration is summarized in Table 3.1. The hull is modeled as an ellipsoid that is symmetric about the longitudinal axis. The dimensions and aerodynamic properties are chosen to closely match those in Lee [2] to enable a meaningful comparison of the optimal trajectories. This design configuration, in terms of geometric dimensions and operating constraints, is found to be consistent with the authors' experience in feasibility studies of high-altitude airships.

Table 3.1: Baseline Airship Design Parameters

Design Parameter	Symbol	Value
Pressure Altitude	h_p	24 km
Length	l	200 m
Diameter	d	50 m
Volume	U_H	261,800 m^3
Surface Area	S	25,300 m^2
Drag Coefficient	C_{Do}	0.04
Maximum Airspeed	$V_{\max}$	30 m/s
Maximum Flight Path Angle	$\gamma_{\max}$	30 deg
Maximum Thrust	$T_{\max}$	10 kN
Maximum Propulsion Power	$P_{\max}$	100 kW
Maximum Climb Rate	$\dot{h}_{\max}$	10 m/s
Added mass coefficient, x-axis	k_1	0.082
Added mass coefficient, y, z-axes	k_2	0.860

3.3 Equations of Motion

1 Kinematic Equations

The position of the airship is described in the topocentric local coordinate system ENU with unit vectors $[\mathbf{e}, \mathbf{n}, \mathbf{u}]$, pointing east, north, and up respectively. Figure 3.1 illustrates the topocentric coordinates along with the Earth-centered inertial coordinates IJK with unit vectors $[\mathbf{I}, \mathbf{J}, \mathbf{K}]$. Note that ℓ is the Earth-relative longitude, and the Earth rotates around the $\mathbf{K}$ vector at the rate of ω_E. Here, λ is the latitude, ℓ is the longitude, R is the Earth radius, and h is the airship altitude, exaggerated for clarity.

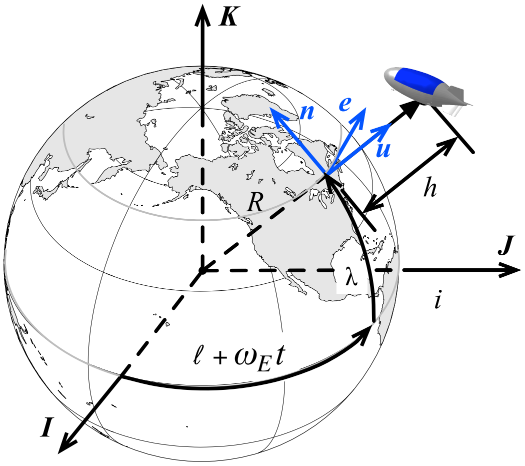

Figure 3.1: Topocentric Coordinate System

Derivation of airship equations involves three velocity concepts: inertial velocity, Earth-relative or local velocity, and wind-relative velocity. Considering the rotation of the Earth, the inertial velocity is found by:

$$\mathbf{V}_I = \mathbf{V}_L + \mathbf{E} \tag{3.4}$$

where $\mathbf{E} = \omega_E(R + h)\cos\lambda\mathbf{e}$. If the Earth rotation is assumed zero, then $\mathbf{E} = 0$ and $\mathbf{V}_I = \mathbf{V}_L$, meaning that the local frame becomes the inertial frame. We include the Earth rotation terms throughout this derivation in order to examine the size of the resulting acceleration terms. In addition, although the spherical-Earth effects are small considering the ranges involved in this study, including them in the equations of motion leads to a general-purpose model suitable for ascent and station-transfer planning over extremely large distances.

To obtain the inertial velocity, we differentiate the position vector with respect to the inertial IJK frame and express the result in the ENU frame. The position of the airship is:

$$\mathbf{r} = (R + h)\mathbf{u} \tag{3.5}$$

The inertial velocity $\mathbf{V_I}$ is then given as:

$$\begin{aligned} \mathbf{V}_I &= \dot{\mathbf{r}} \;=\; \dot{h}\mathbf{u} + \mathbf{\Omega} \times \mathbf{r} \\ &= (\dot{\ell} + \omega_E) \cos\lambda\,(R + h)\,\mathbf{e} + \dot{\lambda}\,(R + h)\,\mathbf{n} + \dot{h}\mathbf{u} \end{aligned} \tag{3.6}$$

where the angular velocity $\mathbf{\Omega}$ with respect to the inertial IJK frame is given by:

$$\begin{aligned} \mathbf{\Omega} &= (\dot{\ell} + \omega_E)\mathbf{K} - \dot{\lambda}\mathbf{e} \\ &= -\dot{\lambda}\mathbf{e} + (\dot{\ell} + \omega_E) \cos\lambda\mathbf{n} + (\dot{\ell} + \omega_E) \sin\lambda\mathbf{u} \end{aligned} \tag{3.7}$$

and ω_E is the angular rate of the Earth.

An important consideration in this paper is the effect of steady-state horizontal winds. The horizontal wind velocity vector is defined as:

$$\begin{aligned} \mathbf{W} &= W \sin\psi_W\mathbf{e} + W \cos\psi_W\mathbf{n} \\ &= W_E\mathbf{e} + W_N\mathbf{n} \end{aligned} \tag{3.8}$$

where W is the total wind speed, ψ_W is the heading, and W_E, W_N are the east and north components, respectively. Figure 3.2 illustrates the relationship between the horizontal wind vector, the airspeed velocity vector, and the local (Earth-fixed) velocity of the airship. The wind-relative velocity vector is defined by the airspeed V, the flight path angle γ, and the heading ψ. We distinguish the local and inertial velocity components with the L and I subscripts, respectively.

From Figure 3.2, the velocity with respect to the local ENU frame is determined as:

$$\mathbf{V}_L = \mathbf{V} + \mathbf{W} \tag{3.9}$$

$$= V \sin\gamma\mathbf{u} + (V \cos\gamma \sin\psi + W_E)\mathbf{e} + (V \cos\gamma \cos\psi + W_N)\mathbf{n} \tag{3.10}$$

$$= V_L \sin\gamma_L\mathbf{u} + V_L \cos\gamma_L \sin\psi_L\mathbf{e} + V_L \cos\gamma_L \cos\psi_L\mathbf{n} \tag{3.11}$$

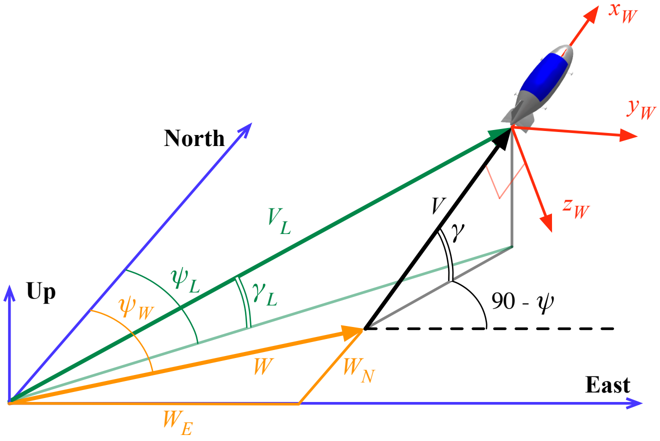

Figure 3.2: Airship Velocity in the Local and Wind-Relative Frames

Equating Eq. (3.6) and Eq. (3.4) and using Eq. (3.10), we obtain the following kinematic relationships:

$$\begin{aligned} \dot{\ell} \cos\lambda(R+h) &= V\cos\gamma\sin\psi + W_E = V_L\cos\lambda_L\sin\psi_L && (3.12)\\ \dot{\lambda}(R+h) &= V\cos\gamma\cos\psi + W_N = V_L\cos\lambda_L\cos\psi_L && (3.13)\\ \dot{h} &= V\sin\gamma = V_L\sin\lambda_L && (3.14) \end{aligned}$$

As shown in Figure 3.2, the wind frame (xyz) is attached to the body of the airship, and is rotated from the ENU frame through the flight path angle γ and heading angle ψ. Note that the bank angle ϕ is assumed zero; the justification for this assumption is provided later in this section. The rotation matrix is therefore:

$$\begin{bmatrix} \mathbf{x} \\ \mathbf{y} \\ \mathbf{z} \end{bmatrix} = \begin{bmatrix} \cos\gamma\sin\psi & \cos\gamma\cos\psi & \sin\gamma \\ \cos\psi & -\sin\psi & 0 \\ \sin\gamma\sin\psi & \sin\gamma\cos\psi & -\cos\gamma \end{bmatrix} \begin{bmatrix} \mathbf{e} \\ \mathbf{n} \\ \mathbf{u} \end{bmatrix} = C \begin{bmatrix} \mathbf{e} \\ \mathbf{n} \\ \mathbf{u} \end{bmatrix} \tag{3.15}$$

2 External Forces

The external forces acting on the airship include aerodynamic lift (L) and drag (D), thrust (T), weight (W) and buoyancy (B). We also consider a generic lateral force N, which may be generated by any means, such as rolling the lift vector through a small angle ϕ, or applying lateral thrust, for example. A free-body diagram of the forces in the $x - z$ plane is shown in Figure 3.3.

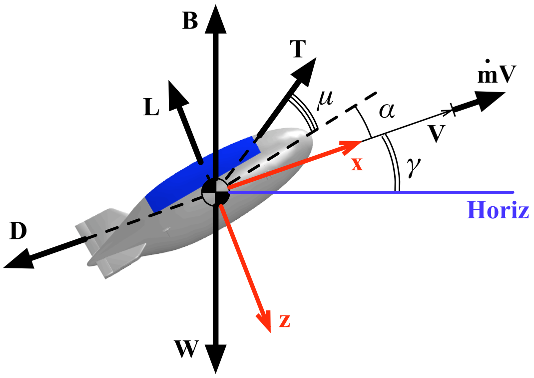

Figure 3.3: External Forces Acting on the Airship

It is important to note here that the total mass of the airship changes significantly during ascent as the internal ballonets contract. A small additional thrust, $\dot{m}V$, can be produced by ejecting air from the ballonets. The mass flow rate $\dot{m}$ is found by differentiating Eq. (3.1) with respect to time:

$$\dot{m} = U_H \dot{\rho}(h) = U_H \frac{\partial \rho}{\partial h} \dot{h}$$

Although the resulting force created by this mass flow will be small compared to the propeller thrust, it is included in this model in order to examine the potential for exploiting this momentum transfer in trajectory planning. The practical considerations of implementation and net benefits should be evaluated in more fully in the context of a vehicle design study.

The sum of forces in the wind-relative frame is:

$$\begin{aligned} \Sigma\mathbf{F} &= [(B-W)\sin\gamma + T\cos(\alpha+\mu) - D]\,\hat{x} \\ &\quad + N\hat{y} + [(W-B)\cos\gamma - L - T\sin(\alpha+\mu)]\,\hat{z} \end{aligned} \tag{3.16}$$

where the lift and drag forces are defined as $L = qU_H^{2/3}C_L(\alpha)$ and $D = qU_H^{2/3}C_D(\alpha)$, respectively. The lift and drag coefficients from Lee [2] are used, and are assumed to vary only with angle of attack.

3 Dynamics

The equations of motion are described by equating the time derivative of the momentum vector with the sum of external forces.

$$\Sigma \mathbf{F} = \frac{d}{dt}\left(M\mathbf{V}_I\right) \tag{3.17}$$

For an airship, we must use a mass tensor M to account for the different effects of added mass in each axis. This phenomena is based on the fact that any object accelerating through a fluid must also accelerate some of the surrounding fluid. For traditional aircraft, the mass of the surrounding fluid is negligible compared to the mass of the vehicle. For airships, however, the added mass effect is significant and must be included. The mass tensor is defined as:

$$M = m[I] + \begin{bmatrix} k_1 & 0 & 0 \\ 0 & k_2 & 0 \\ 0 & 0 & k_3 \end{bmatrix} \rho(h)U_H = \begin{bmatrix} m + m_{ax} & 0 & 0 \\ 0 & m + m_{ay} & 0 \\ 0 & 0 & m + m_{az} \end{bmatrix} \tag{3.18}$$

where k_1, k_2, k_3 are added mass coefficients that can be derived from the geometry of the vehicle [25], and m is the scalar total mass of the airship structure and internal gas. For an airship that is symmetric about the x axis, $k_2 = k_3$. where the mass flow rate $\dot{m}$ is found by differentiating Eq. (3.1) with respect to time:

$$\dot{m} = U_H\dot{\rho}(h) = U_H\frac{\partial \rho}{\partial h}\dot{h}$$

The time rate of change of the mass is included in the derivation, because the total mass of the airship changes significantly with altitude as the internal ballonets expand and contract with air. This ejection of air during ascent has the effect of providing a small additional thrust, and is described in further detail below.

The total inertial acceleration is the acceleration of the airship with respect to the local ENU frame, plus the acceleration of the ENU frame in inertial space, plus the Coriolis acceleration. Using the notation $(\frac{d\cdot}{dt})_A$ to denote a derivative taken with respect to frame A, the inertial acceleration expressed in the wind frame is:

$$\left(\frac{d\mathbf{V}_I}{dt}\right)_I = \left(\frac{d\mathbf{V}_L}{dt}\right)_L + \omega_{L/I} \times \mathbf{V}_L + \left(\frac{d\mathbf{E}}{dt}\right)_I \tag{3.19}$$

Now define $\mathbf{V} = [V, 0, 0]^T$ to be the expression of the wind-relative velocity vector in the wind frame. Also, let $\omega_{W/L}$ be the angular rotation of the wind frame with respect to ENU, and let $\omega_{L/I}$ be the angular velocity of ENU with respect to the inertial frame. The first two terms of Eq. (3.19) are then expanded as follows:

$$\left(\frac{d\mathbf{V}_L}{dt}\right)_L = \left(\frac{d\mathbf{V}}{dt}\right)_W + \omega_{W/L} \times \mathbf{V} + \left(\frac{d\mathbf{W}}{dt}\right)_L \tag{3.20}$$

$$\left(\frac{d\mathbf{E}}{dt}\right)_I = \left(\frac{d\mathbf{E}}{dt}\right)_L + \omega_{L/I} \times \mathbf{E} \tag{3.21}$$

where the angular velocities and the wind velocity derivative are defined as:

$$\omega_{L/I} = \omega_E \left(\cos\lambda \mathbf{n} + \sin\lambda \mathbf{u}\right) \tag{3.22}$$

$$\omega_{W/L} = -\dot{\psi} \sin\gamma \mathbf{e} + \dot{\gamma}\mathbf{n} + \dot{\psi}\cos\gamma \mathbf{u} \tag{3.23}$$

$$\left(\frac{d\mathbf{W}}{dt}\right)_L = \dot{\mathbf{W}} = \dot{W}_E \mathbf{e} + \dot{W}_N \mathbf{n} \tag{3.24}$$

$$\left(\frac{d\mathbf{E}}{dt}\right)_L = \dot{\mathbf{E}} = \omega_E \left(\dot{h}\cos\lambda - (R+h)\sin\lambda\dot{\lambda}\right)\mathbf{e} \tag{3.25}$$

The wind rate terms are simply the product of the wind gradient across altitude and the altitude rate, e.g. $\dot{W}_E = \frac{\partial W_E}{\partial h}\dot{h}$. The resulting expression for the inertial acceleration is:

$$\left(\frac{d\mathbf{V}_I}{dt}\right)_I = \left(\frac{d\mathbf{V}}{dt}\right)_W + \omega_{W/L} \times \mathbf{V} + \omega_{L/I} \times \mathbf{V}_L + \left(\frac{d\mathbf{W}}{dt}\right)_L + \left(\frac{d\mathbf{E}}{dt}\right)_L + \omega_{L/I} \times \mathbf{E} \tag{3.26}$$

Consider the diagram in Figure 3.4 to illustrate the physical nature of the force associated with the changing mass. As the airship ascends, air is blown out of the ballonets to maintain neutral buoyancy. It is assumed that the air exits the airship at a velocity equal and opposite to the current airspeed, so that it has zero velocity with respect to the surrounding air. Consider now the change in linear momentum experienced by the airship over a time interval dt. The original system has mass $m(h) + dm$ and flies at velocity $V + dV$. The new system after ejecting the air has the airship with mass $m(h)$ and velocity V, and the lost mass $-dm$ with velocity $-V$ relative to the airship. The inertial velocity of the ejected air is $V - V = 0$. In the absence of external forces, linear momentum must be conserved. We therefore have:

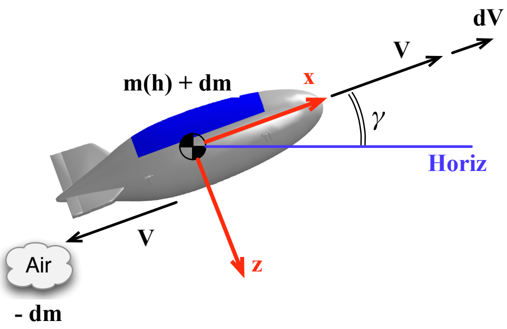

Figure 3.4: Conservation of Linear Momentum

$$(m(h) + dm)\,(V + dV) - dm\,(V - V) = m(h)V \tag{3.27}$$

Neglecting second order differential terms, then dividing by dt and including forces in the x direction, the above expression leads to:

$$\Sigma F_x = m(h)\frac{dV}{dt} + V\frac{dm}{dt} \tag{3.28}$$

which is consistent with Eq. (3.17). The effect is similar in principle to the thrust produced by a rocket, although clearly much smaller in magnitude. Note that the velocity V here is the airspeed velocity, which is always positive, and the mass flow rate is always negative during ascent, so that the additional force due to mass flow rate is always positive in the x direction during ascent.

4 Complete Equations of Motion

The complete equations of motion of the airship include the rate of change of its geographic position, provided in the kinematic Eqs. (3.12) through (3.14), and the rate of change of its wind-relative velocity. The velocity vector derivative is found by differentiating Eq. (3.4) with respect to the inertial frame, and expressing the result in the wind frame.

Expanding Eq. (3.26) with Eq. (3.16) and Eq. (3.17), we obtain the following expressions for the time-rate of change of the wind-relative velocity components:

$$\dot{V} = \frac{(B-W)\sin\gamma + T\cos\alpha - D - U_H\dot{\rho}V}{m+m_{ax}} - \dot{W}_x - a_{Ex} \tag{3.29}$$

$$\dot{\gamma} = \frac{(B-W)\cos\gamma + T\sin\alpha + L}{(m+m_{az})V} + \frac{\dot{W}_z + a_{Ez}}{V} \tag{3.30}$$

$$\dot{\psi} = \frac{N}{(m+m_{ay})V\cos\gamma} - \frac{\dot{W}_y + a_{Ey}}{V\cos\gamma} \tag{3.31}$$

where the wind rate terms in the wind frame are

$$\dot{W}_x = \dot{W}_E\cos\gamma\sin\psi + \dot{W}_N\cos\gamma\cos\psi \tag{3.32}$$

$$\dot{W}_y = \dot{W}_E\cos\gamma - \dot{W}_N\sin\gamma \tag{3.33}$$

$$\dot{W}_z = \dot{W}_E\sin\gamma\sin\psi + \dot{W}_N\sin\gamma\cos\psi \tag{3.34}$$

The additional acceleration due to the rotation of the Earth is:

$$\mathbf{a}_E = \begin{bmatrix} a_{Ex} \\ a_{Ey} \\ a_{Ez} \end{bmatrix} = \omega_{L/I} \times \mathbf{V}_L + \left(\frac{d\mathbf{E}}{dt}\right)_L + \omega_{L/I} \times \mathbf{E} \tag{3.35}$$

The expanded form of the acceleration terms due to rotation of the Earth are:

$$\begin{aligned} a_{Ex} &= \omega_E \left\{ (W_E + V)\left(\sin\lambda\cos\gamma\cos\psi - \cos\lambda\sin\gamma\right) - 2W_N \sin\lambda\cos\gamma\sin\psi \right\} \\ &\quad + \omega_E^2 (R+h)\cos\lambda(\cos\gamma\cos\psi\sin\lambda - \sin\gamma\cos\lambda) \end{aligned} \tag{3.36}$$

$$\begin{aligned} a_{Ey} &= \omega_E \left\{ -W_E \sin\lambda\sin\psi - 2W_N \sin\lambda\cos\psi + V\left(\cos\lambda\sin\gamma\cos\psi - \sin\gamma\cos\psi\left(1-\cos^2\psi\right)\right)\right\} \\ &\quad - \omega_E^2 (R+h)\cos\lambda\sin\psi\sin\lambda \end{aligned} \tag{3.37}$$

$$\begin{aligned} a_{Ez} &= \omega_E \left\{ W_E\left(\sin\lambda\sin\gamma\cos\psi + \cos\lambda\cos\gamma\right) - 2W_N \sin\lambda\sin\gamma\sin\psi \right\} \\ &\quad + \omega_E \left\{ V\left(\cos\lambda\sin\psi\left(1+\sin^2\gamma\right) - \sin\lambda\sin\gamma\cos\gamma\sin\psi\cos\psi\right)\right\} \\ &\quad + \omega_E^2 (R+h)\cos\lambda(\sin\gamma\cos\psi\sin\lambda + \cos\gamma\cos\lambda) \end{aligned} \tag{3.38}$$

5 Dimensional Scaling

In order to effectively use any numerical optimization routine, it is important to first scale the variables of the problem. Simply put, the objective is to scale all of the variables so that they are neither very small nor very large. In this problem, a common set of dimensional scalings are applied for time, length, velocity and acceleration. The characteristic scales are defined as:

$$d_c = \frac{R}{k^2}, \quad V_c = \frac{\sqrt{gR}}{k}, \quad t_c = \frac{1}{k}\sqrt{\frac{R}{g}} \tag{3.39}$$

where R is the Earth radius, g is the gravitational acceleration, and $k > 0$ is a scaling constant, chosen to provide a balanced scaling of variables throughout the dynamics and constraint equations. Note that the scales are consistent, such that $V_c = d_c/t_c$ and

$g = V_c/t_c$. The normalized variables are defined as:

$$\bar{V} = \frac{V}{V_c}, \quad \bar{h} = \frac{h}{d_c}, \quad \tau = \frac{t}{t_c} \tag{3.40}$$

$$\bar{W}_E = \frac{W_E}{V_c}, \quad \bar{W}_N = \frac{W_N}{V_c} \tag{3.41}$$

$$\bar{T} = \frac{T}{U_H \rho(h_0) g}, \quad \bar{\rho}(\bar{h}) = \frac{\rho(h)}{\rho(h_0)} \tag{3.42}$$

and the normalized lift and drag forces are expressed as:

$$\bar{L} = \frac{L}{U_H \rho(h) g} = AC_L(\alpha)\bar{V}^2 \tag{3.43}$$

$$\bar{D} = \frac{D}{U_H \rho(h) g} = AC_D(\alpha)\bar{V}^2 \tag{3.44}$$

where $A = d_c/(2U_H^{1/3})$. Additionally, the normalized time derivative is related to the original time derivative as follows:

$$(\ )' = \frac{d(\ )}{d\tau} = t_c \frac{d(\ )}{dt} = t_c\dot{(\ )} \quad \Rightarrow \quad (\ )' = \frac{1}{k}\sqrt{\frac{R}{g}}\dot{(\ )}$$

After some algebra, the complete set of equations can now be written in non-dimensional form as follows:

$$\bar{V}' = \frac{1}{1+k_1}\left\{\frac{\bar{T}\cos(\alpha+\mu) - \frac{\partial\bar{\rho}}{\partial\bar{h}}\sin\gamma\bar{V}^2}{\bar{\rho}(\bar{h})} - AC_D(\alpha)\bar{V}^2\right\} - \frac{\partial\bar{W}_x}{\partial\bar{h}}\bar{V}\sin\gamma - \bar{a}_{Ex} \tag{3.45}$$

$$\gamma' = \frac{1}{1+k_2}\left\{\frac{\bar{T}\sin(\alpha+\mu)}{\bar{\rho}(\bar{h})\bar{V}} + AC_L(\alpha)\bar{V}\right\} + \frac{\partial\bar{W}_z}{\partial\bar{h}}\sin\gamma + \bar{a}_{Ez}/\bar{V} \tag{3.46}$$

$$\ell' = \frac{\bar{V}\cos\gamma\sin\psi + \bar{W}_E}{\cos\lambda(\bar{R}+\bar{h})} \tag{3.47}$$

$$\lambda' = \frac{\bar{V}\cos\gamma\cos\psi + \bar{W}_N}{(\bar{R}+\bar{h})} \tag{3.48}$$

$$\bar{h}' = \bar{V}\sin\gamma \tag{3.49}$$

6 Assumptions

We first discuss the omission of bank angle in these equations. Traditional aircraft turn by banking, which rotates the lift vector to create lateral acceleration. However, this form of turning is not necessarily the best option for airships, for at least three reasons. First, airships produce much less dynamic lift than traditional aircraft, as airships rely primarily on buoyancy for the lifting force. Second, the combination of the weight and buoyancy forces creates a natural stabilizing moment about the roll axis, as the center of buoyancy is located above the center of gravity. This stabilizing moment must be overcome in order to hold a non-zero bank angle over time. To perform this maneuver aerodynamically would require large control surfaces, which, for the stratospheric airship, would bring a significant increase weight and drag. Third, the types of payloads for station-keeping missions will likely be Earth-pointing or zenith pointing. Large bank angles would tend to violate these payload pointing requirements for fixed mounted payloads, whereas pure yaw maneuvers would pose no problem. It is therefore reasonable to consider other mechanisms for turning that do not rely on bank angle, such as differential thrust to turn with sideslip, or pure lateral thrust. The inherent roll limitation is evidenced in [2], where bank angle is used as a control input, but with a limit of only 5 deg. As a consequence of these practical airship design constraints, we assume bank angle remains sufficiently close to zero such that it can be ignored in the equations of motion.

In this paper, we assume that the airship regulates internal pressure to maintain zero static lift ($B = W$) throughout the flight envelope. The longitudinal control inputs are angle-of-attack α, thrust T, and thrust vector angle μ. We choose the lateral control input to be heading ψ, and enforce bounds on $\dot{\psi}$. The states of the system are the wind-relative velocity V, flight path angle γ, and the geographic position $[\ell, \lambda, h]$. Therefore, the state equations for the system include the kinematic expressions, Eqs. (3.12) through Eqs. (3.14), and the longitudinal velocity derivatives, Eqs. (3.29) and (3.30).

To summarize, this formulation of the airship equations of motion includes the point mass kinematic equations for a spherical Earth, steady-state horizontal winds that vary with altitude, longitudinal dynamics governed by lift, drag and vectored thrust, mass variation with altitude, the effects of added mass, and virtual accelerations due to wind variations and Earth rotation. This formulation is more general than the model provided in Lee [2], in that it includes Earth rotation and mass variation across altitude. Also note that the dynamic relationship of $\dot{\psi}$ with the other states and controls, given in Eq. (3.31), can be used as a time varying constraint if desired. However, for this study we impose constant bounds on $\dot{\psi}$.

3.4 Environment Models

The stratospheric airship must fly through a wide range of flight conditions, from 0 to 30 m/s airspeed, and from sea-level to about 21 km altitude. Across this altitude range, the atmospheric density and steady-state wind velocity change considerably. The subsections below describe the models used to approximate the atmospheric density and wind across altitude. A model of the solar power generated during flight is provided in Section 3.5.

1 Atmospheric Density

During its ascent, the atmospheric density drops by a factor of 16, from 1.225 to about 0.075 kg/m^3. I assume the atmospheric density changes with altitude according to the standard atmosphere model [26]. A third order polynomial is fit to the standard atmosphere data over an altitude range of 0 to 23 km. The altitude is normalized prior to fitting to obtain better numerical accuracy. The polynomial expression is given as:

$$\rho(h) = \rho(0)\left[c_0 + c_1(h/d_c) + c_2(h/d_c)^2 + c_3(h/d_c)^3\right] \tag{3.50}$$

where d_c is a dimensional scaling parameter, defined in Eq. (3.39). Using $d_c = 15,891.915$ km and $\mathbf{c} = [-0.11159,\ 0.71537,\ -1.45854,\ 0.99523]^T$ gives a maximum error of 2.6% and a mean error of 0.84%.

2 Horizontal Wind Model

The average wind velocity also changes considerably with altitude, although with much less predictability than that of the density variation. The general trend is that windspeed gradually increases during ascent through the troposphere, reaching a peak in the jet-stream altitude range of 10-15 km. It then gradually decreases again to reach a minimum speed in the lower portion of the stratosphere, generally between 18-25 km. The actual wind profile changes with geographic location and the time of year, and is also effected by the 11-year solar cycle.

In general, wind velocity can be split into steady-state and time-varying components. While the actual winds encountered during flight cannot be predicted exactly, steady-state horizontal winds are known to follow specific trends with altitude, geographic position, and the time of year. Typical wind behavior can be adequately characterized based upon meteorological data, which provides a mechanism for design-phase planning. In addition, weather balloons and other instruments can be used immediately prior to flight, for pre-flight and onboard planning.

The 1993 horizontal wind model (HWM93), produced by the Naval Research Laboratory (NRL), uses a combination of historical meteorological data and measurements from radar and rocket sounding experiments to develop an analytic emperical model [27]. A FORTRAN program of the HWM93, available on the NRL website[28], was used to generate wind profiles over altitude at select times and geographic locations. In this paper, we use the HWM93 to model the average wind profile at the coordinates of 118^o $0.0'$ W, 35^o $0.0'$ N. This is located at the southern end of Edwards AFB, approximately 100 km north of Los Angeles. The variation of the east component of wind across altitude is shown in Figure 3.5 for four different times of year. The north component of the wind is not shown, as it the maximum speed is under 1 m/s. This is representative of the typical wind profile observed in the continental U.S., with the peak speeds occurring in the jet-stream altitude range of 10-15 km, and with the wind directed primarily eastward.

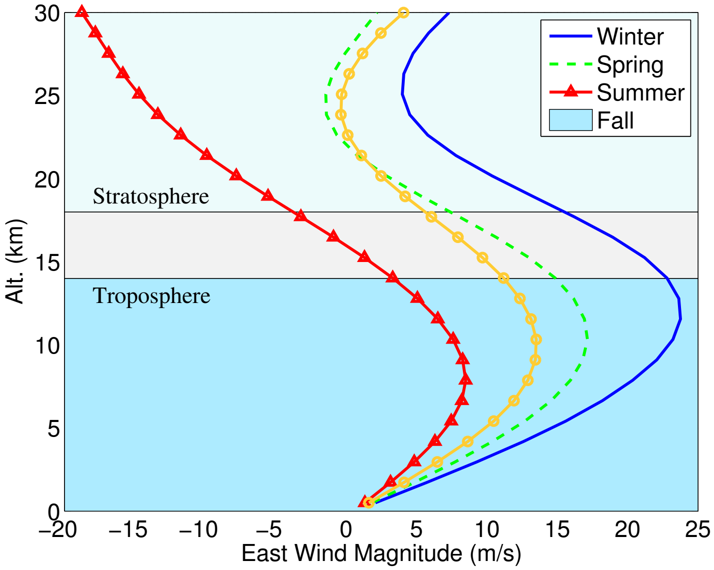

Figure 3.5: HWM93 Wind Profile over Southern California

The wind velocity may be modeled purely as a function of altitude, as shown in Figure 3.5, or the variation across latitude and longitude may also be considered. If the trajectory is restricted to a small enough region in the local horizontal plane, then it is reasonable to use a model that has only altitude dependence. However, the trajectory must traverse a large horizontal distance, the wind profile may change considerably across this distance and so a 3-dimensional profile ought to be used.

3 Wind Model with Altitude Dependence Only

The east and north components of the wind are fit to the HWM93 data using 7th order polynomials. As before, the polynomial is fit after normalizing the altitude and velocity with constant scaling parameters. The expression for the east wind approximation is:

$$W_E(h) = V_c \left[c_{e0} + c_{e1}(h/d_c) + c_{e2}(h/d_c)^2 + \ldots + c_{e7}(h/d_c)^7\right] \tag{3.51}$$

The north wind is found with the same polynomial expression, but with the $\mathbf{c}_n$ coefficients. Using $d_c = 15,891.915$ km and $V_c = 395.04$ m/s, we obtain the following coefficients for the winter season wind model:

$$\mathbf{c}_e = [-0.16235, 0.8355, -1.64017, 1.60473, -0.8928, \; 0.20646, 0.09708, \; 0.00246]^T \tag{3.12}$$

$$\mathbf{c}_n = [-0.00103, 0.0050, -0.00789, 0.00459, -0.0010, -0.00085, 0.00047, -0.00015]^T \tag{3.13}$$

The approximations match the original model with a maximum error of 0.4% in the east component, and 1.1% in the north component.

3.5 Solar Power Generation Model

One of the fundamental design features of stratospheric airships is that they can use hull-mounted thin film solar cells to generate sufficient power for sustained flight. Solar power is converted into electricity, which is used to operate the payload, electric motors and avionics, and to charge batteries. The process of performing this power management is not trivial, and is undoubtedly one of the most challenging design aspects of these airships. Although the power management system cannot be easily modeled, it is possible to develop a general model for the total solar power available to the airship.

The available solar power depends upon a variety of factors. This includes factors beyond our control (the time of year, time of day, and geographic location), vehicle design factors (the solar cell coverage area and hull geometry), and lastly, operational factors (airship orientation). This section provides a model for computing the total solar power that can be captured by the hull-mounted solar cells as a function of hull geometry, latitude, time, airship orientation, and altitude. A similar model is presented in Wang et.al. [29], but it provides no way to model the significant variation in received solar flux across altitude.

It is also important to note that the efficiency of the solar cells in absorbing and converting solar energy is not included in the model presented here. Thus, solar cell efficiency may be treated completely independently of this model.

1 Hull Geometry

The airship hull is modeled as a prolate ellipsoid, with a finite number of solar panels distributed symmetrically over a fractional area of the top surface. The ellipsoid has semi-major axis a in the body-frame x direction, and semi-minor axes b in the body-frame y, z directions. The curved solar array along the top of the hull is modeled as a finite number of flat panels. Each panel is located at an angular position (α_i, β_j) where α is measured about the y-axis, and β about the x-axis. The size of the solar panel is given by the extreme angular positions, so that $\alpha_{\min} \leq \alpha_i \leq \alpha_{\max}$ for $i = \{1, \ldots, M\}$ and $\beta_{\min} \leq \beta_j \leq \beta_{\max}$ for $j = \{1, \ldots, N\}$.

Approximating each panel as a rectangle, inspection of the geometry shows the elemental area to be:

$$\delta A_{i,j} = b \cos\theta_i \delta\beta \times \frac{l(\theta_i)}{\cos(\alpha_i - \tau_i)} \delta\alpha \tag{3.54}$$

where

$$\begin{aligned} \tau_i &= \tan^{-1}\left(\frac{b^2 \sin\alpha_i}{a^2 \cos\alpha_i}\right) && (3.55) \\ \theta_i &= \tan^{-1}\left(\frac{b \sin\alpha_i}{a \cos\alpha_i}\right) && (3.56) \\ l(\theta_i) &= \sqrt{b^2 \cos^2\theta_i + a^2 \sin^2\theta_i} && (3.57) \end{aligned}$$

The normal vector for each panel in the body frame is:

$$\mathbf{n}_{i,j} = (\sin\tau_i)\mathbf{x} + (\cos\tau_i \sin\beta_j)\mathbf{y} + (-\cos\tau_i \cos\beta_j)\mathbf{z} \tag{3.58}$$

Consider the airship having the full top half of the hull covered with solar cells. When the sun is directly overhead, the exposed cross-sectional area is the area of the exposed ellipse, πab. This is of course less than the full surface area of the top-half. For an ellipsoid with $a > b$, the surface area is given as:

$$S = 2\pi b \left(b + a \sin^{-1}(e)/e\right)$$

where $e = \sqrt{1-(b/a)^2}$. Dividing the cross-sectional area by the surface area of the top half, we can determine the total amount of cosine loss due to curvature of the hull. The total loss simplifies to:

$$\eta_C = \frac{1}{b/a + \sin^{-1}(e)/e} \tag{3.59}$$

This is a particularly useful formula as it is non-dimensional, requiring only the ratio of semi-minor to semi-major axes, b/a. For the baseline configuration considered in this paper, $b/a = 0.25$ and $\eta_C = 0.62$. Thus, 38% of the effective solar cell area is lost immediately due to the curvature of the hull.

2 Sun Vector

The sun vector is defined by its azimuth ϕ_s and elevation γ_s, which change smoothly with time from dawn to dusk. In the *ENU* frame, the coordinates of the unit sun vector are:

$$\mathbf{s} = (\cos\gamma_s \sin\phi_s)\mathbf{e} + (\cos\gamma_s \cos\phi_s)\mathbf{n} + (\sin\gamma_s)\mathbf{u} \tag{3.60}$$

The azimuth and elevation can be expressed as follows:

$$\begin{aligned} \gamma_s &= \sin^{-1}\left(\cos h \cos d \cos\lambda + \sin d \sin\lambda\right) && (3.61)\\ \phi_s &= \sin^{-1}\left(-\frac{\sin h \cos d}{\cos\gamma_s}\right) && (3.62) \end{aligned}$$

where h is the local hour angle, starting from 0 at noon and varying through 2π over 24 hours. The sun's declination d varies with the time of year. In degrees, it can be expressed as:

$$d = -23.45\cos\left(\frac{360}{365}(t_d + 10)\right)$$

with $0 \leq t_d \leq 365$ representing the time of year in days.

Let C be the rotation matrix that rotates from the *ENU* frame to the airship body frame. Assuming zero bank angle, C is defined as:

$$C = \begin{bmatrix} \cos\gamma\sin\psi & \cos\gamma\cos\psi & \sin\gamma \\ \cos\psi & -\sin\psi & 0 \\ \sin\gamma\sin\psi & \sin\gamma\cos\psi & -\cos\gamma \end{bmatrix} \tag{3.63}$$

The sun vector in the body frame is then just $C\mathbf{s}$.

3 Solar Flux Through All Panels

The total solar flux at any time for the airship is:

$$F = \sum_{i,j} F_{i,j} \tag{3.64}$$

where $F_{i,j}$ is the flux at panel (i, j). The solar flux at any time for panel $(i, j))$ is:

$$F_{i,j} = I\delta A_{i,j}\cos\zeta_{i,j} \tag{3.65}$$

where I is the local solar irradiance, and $\zeta_{i,j}$ is the solar incidence angle for panel (i, j). This is the angle between the normal vector of the panel and the sun vector, which can be written as:

$$\cos\zeta i, j = (C\mathbf{s}) \cdot \mathbf{n}_{i,j} \tag{3.66}$$

We must ignore negative fluxes. Therefore, the expression becomes:

$$F_{i,j} = \begin{cases} I(h)\delta A_{i,j}\cos\zeta_{i,j} & \gamma_s > 0,\ -\frac{\pi}{2} \le \zeta i, j \le \frac{\pi}{2} \\ 0 & \text{else} \end{cases} \tag{3.67}$$

An illustration is provided in Figure 3.6, showing the path of the sun through the day and the relative orientation of one panel. Sun locations at hours 11 and and 18 are shown as examples to illustrate the changing azimuth and elevation angle. This figure assumes a northern latitude, as the sun traverses the southern sky.

Note that $I \approx 1,350\ \mathrm{W/m^2}$ outside of the atmosphere, and it drops to $I \approx 1,000\ \mathrm{W/m^2}$ at the Earth's surface due to energy being absorbed by the atmosphere. We develop

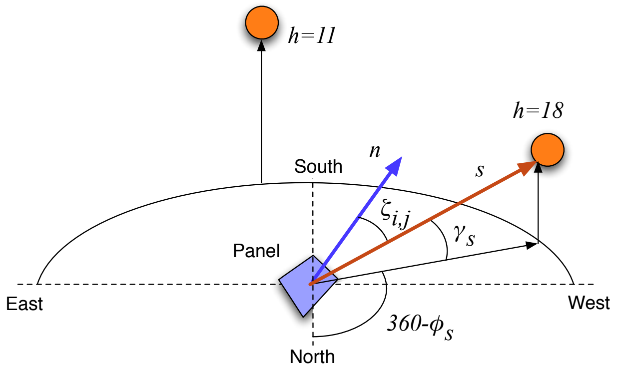

Figure 3.6: Sun Position with Respect to Solar Panel

a rough model here to approximate the change in I across altitude, so that the loss at altitude h is proportional to the accumulated mass of the atmosphere above that altitude. The expression is:

$$I(h) = 1350 - 350\left[\frac{\int_h^{50\text{km}} \rho(h)dh}{Q}\right]$$

where $Q = \int_0^{50\text{km}} \rho(h)dh$ is the integrated density up to 50 km, above which there is negligible atmospheric mass. Using the standard atmosphere, we find $Q \approx 10,340$ kg/m^2. Note that this does not account for lower sun elevation angles when sunlight must go through more of the atmosphere. A plot of the resulting irradiation dependence with altitude is shown in Figure 3.7.

We can now illustrate the solar flux model in an example. Consider an airship at 35 deg latitude, and consider two orientations, one with the it heading east, the other with it heading north. We use the solar flux model to compute a normalized solar intensity over a 24 hour period, at 4 different times of the year. We define the normalized solar intensity as $F/(IS_P)$, where F is the total flux received, I is the solar irradiation constant (outside the atmosphere) and S_P is the total area of the panels. In this example $S_P = S/2$ as the entire top half of the hull is covered with panels. If our panel were a flat plate, the peak intensity would be 1.0, but using our curved hull with $b/a = 0.25$,

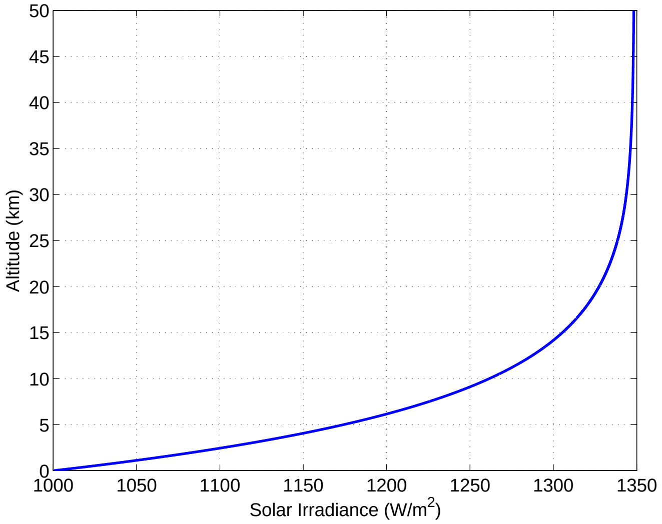

Figure 3.7: Irradiance Variation with Altitude

the peak intensity is 0.62 (see Eq. (3.59). The results of the sample analysis are shown in Figure 3.8.

Figure 3.8: Normalized Solar Intensity for East-West and North-South Orientations at Winter, Spring/Fall, Summer, for 0 Deg and 30 Deg Pitch Angles

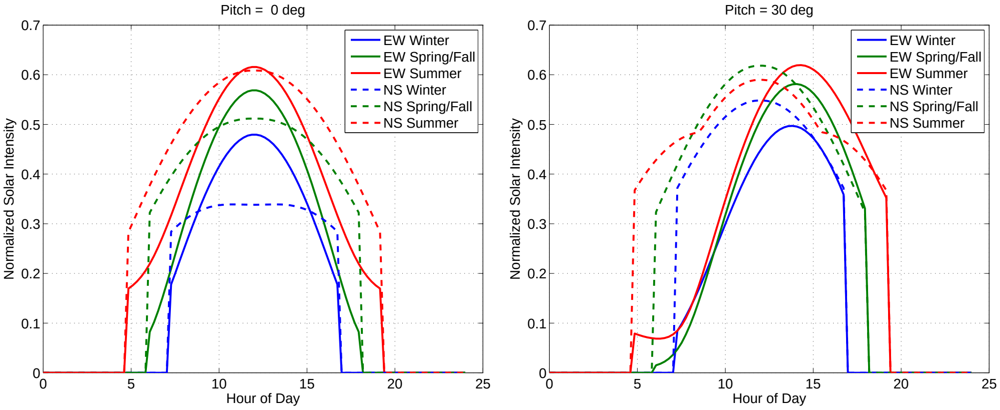

For both plots, we see the intensity jumping up at the dawn hour and jumping back to zero at dusk, the times of which depend on the season. Consider the 0 deg pitch case first. Here, the plots are symmetric about the noon hour, as we would expect. In every season, the north-south (NS) orientation starts and finishes the day with a larger intensity than that of the east-west (EW). This is because with a NS orientation, the long side of the vehicle (with a larger area) is exposed to the sun at these times of the day. For the summer time, the peak intensity of 0.62 is nearly achieved, as the sun elevation reaches about 80 deg at this latitude. For the winter time, the intensity does not climb much during the day as the sun elevation only reaches about 31.5 deg at noon.

Now consider the 30 deg pitch case. Here, the intensity is asymmetric about the noon hour for the east-west orientations. This is due to the positive pitch angle, which obstructs the top half of the hull from view of the sun in the morning. This clearly illustrates the potential for the airship attitude to have a significant impact on its power generation capability.

4 Remarks

Analyzing the separate contributions of this model, we see that the total solar flux on the airship depends upon several different factors:

1. The geographic latitude and altitude
2. The time of year and time of day
3. The size and shape of the airship hull
4. The placement of solar cells on the hull surface
5. The orientation of the airship hull

The latitude and altitude are dictated by the mission or application. For long endurance missions, the time of year will impact the solar flux to greater degrees at larger latitudes. The size and shape of the hull, and the choice of where to place solar cells, are design decisions that should be explored in order to best accommodate the expected conditions for the mission. For example, if it is expected that the majority of the airship's flight in the northern hemisphere would involve station-keeping against a westerly wind, then solar panel placement should be biased towards the southern side of the hull to maximize energy production. The final influence is the orientation of the airship hull with respect to the sun. The solar flux model may be included in the trajectory optimization phase in order to develop flight plans that provide improved energy production.

It is also interesting to consider the tradeoff associated with choosing the solar cell coverage for the vehicle. In some cases, it may be known that a particular orientation will be flown a majority of the time, due to a high confidence that the wind direction stays within a certain small range. Under such conditions, the solar cell coverage may be greatly biased to one side of the vehicle. Otherwise, the coverage may need to be symmetric to ensure a sufficient solar cell area is available for any possible orientation. In either case, the question remains as to how much of the hull should be covered in solar cells. Adding a solar cell adds cost and mass, both for the cell itself and the wiring to connect it. Clearly it is not desirable to add a cell if it will not receive sufficient solar power. Combining the solar generation model presented here with a historical, statistical wind model, one could develop a Monte Carlo simulation to study the energy production associated with different candidates of solar cell coverage geometries.

Chapter 4

Problem Formulations

We now consider the formulation of trajectory optimization problems for various types of airship flights. Let the state vector $\mathbf{x}(t)$ and control vector $\mathbf{u}(t)$ be defined as:

$$\begin{aligned}\mathbf{x}(t) &= [V,\, \gamma,\, \ell,\, \lambda,\, h]^T && (4.1)\\ \mathbf{u}(t) &= [T,\, \alpha,\, \mu,\, \psi]^T && (4.2)\end{aligned}$$

The airship dynamic model is described by the system of nonlinear differential equations given in Eqs. (3.12)-(3.14) and Eqs. (3.29)-(3.30), which can be expressed as:

$$\dot{\mathbf{x}}(t) = f\left(\mathbf{x}(t), \mathbf{u}(t), t\right) \tag{4.3}$$

The optimization problem is to choose a control history $\mathbf{u}(t)$ that minimizes a scalar performance index, J, subject to the equations of motion over some time interval $[t_0, t_f]$, and other constraints that may be enforced on the states and controls. Specifically, we enforce constant bounds on the states, controls, and control rates, and impose both path constraints χ and terminal constraints $\mathbf{\Psi}$ on the state. The problem is summarized as:

$$\begin{aligned} \min_{\mathbf{u}(t),t_f} \quad & J(\mathbf{x}(t),\mathbf{u}(t),t) \\ \text{Subject to} \quad & \dot{\mathbf{x}}(t) = f\left(\mathbf{x}(t),\mathbf{u}(t),t\right),\ \mathbf{x}(t_0) \in \mathbf{X}_0 \\ & \mathbf{x}_L \le \mathbf{x}(t) \le \mathbf{x}_U,\ t > t_0 \\ & \mathbf{u}_L \le \mathbf{u}(t) \le \mathbf{u}_U \\ & \dot{\mathbf{u}}_L \le \dot{\mathbf{u}}(t) \le \dot{\mathbf{u}}_U \\ & \chi(\mathbf{x}(t)) \le 0 \\ & \mathbf{\Psi}(\mathbf{x}(t_f)) = 0 \end{aligned} \tag{4.4}$$

where $\mathbf{X}_0$ represents an allowable set of initial states. The path constraints include bounds on the climb rate and power, as given below:

$$\chi_1 = V\sin\gamma - \dot{h}_{\max} \le 0 \tag{4.5}$$

$$\chi_2 = TV - P_{\max}\eta \le 0 \tag{4.6}$$

The terminal constraint enforces a final desired position (ℓ_f, λ_f, h_f) and speed (V_{Lf}) to be achieved.

$$\mathbf{\Psi}_1 = \ell(t_f) - \ell_f = 0 \tag{4.7}$$

$$\mathbf{\Psi}_2 = \lambda(t_f) - \lambda_f = 0 \tag{4.8}$$

$$\mathbf{\Psi}_3 = h(t_f) - h_f = 0 \tag{4.9}$$

$$\mathbf{\Psi}_4 = (V\cos\gamma\cos\psi + W_N)^2 + (V\cos\gamma\sin\psi + W_E)^2 - V_{Lf}^2 = 0 \tag{4.10}$$

Two fundamentally different types of optimal ascent trajectories are considered: minimum time and minimum energy. Within the context of feedback control design, the term “energy” is indeed often referred to as the total control effort, $\int u^2(t)dt$. However, this is not necessarily meaningful for airship trajectory planning, as it does not reflect the true energy expenditure of the airship during flight. The total energy consumption of the airship during the trajectory is the integral of the required power:

$$E = \int_{t_0}^{t_f} \frac{VT}{\eta} dt \tag{4.11}$$

I consider only the power required for propulsion, ignoring any power required for payload and/or systems operation, as these are expected to be small in comparison and are not affected by the trajectory. It is reasonable to assume the efficiency remains constant throughout the flight, allowing it to be disregarded in the performance index. We can now define the performance index as

$$J = K_t t_f + K_p \int_{t_0}^{t_f} VT dt \tag{4.12}$$

where K_t and K_p are non-negative weighting coefficients that enable the problem to be cast as pure minimum time ($K_t = 1, K_p = 0$), pure minimum energy, ($K_t = 0, K_p = 1$), or a blend of both objectives ($K_t > 0, K_p > 0$).

It is important to note that a more comprehensive model of the airship flight power requirement would include the power required to operate the pressure regulation system, which must blow air out of the ballonets during ascent. Providing a more accurate power model would help to design more realistic trajectories for the minimum energy problem. In addition, it may be worthwhile to model the maximum air flow rate as a constraint. This would allow the buoyancy and weight to be modeled separately, with mass as a state, so that neutral buoyancy conditions are only achieved when the pressure regulation system can expel or intake air fast enough.

Chapter 5

Numerical Solution Methods

The optimal control problem described above can only be solved numerically. An effective method for developing a numerical solution is to transform this dynamic optimization problem into a parameter optimization problem. We use a collocation approach, discretizing the dynamic equations so that both the states and controls become decision variables over a finite number of nodes [30, 31, 32]. We then solve the problem numerically using SNOPT, which is a sequential quadratic programming (SQP) tool that exploits the sparsity structure of the Jacobian matrix [33].

Define the time interval $t \in [t_0, t_f]$ over N nodes, so that $t_k = t_0 + \bar{\tau}_k t_f$, where:

$$0 = \bar{\tau}_1 < \bar{\tau}_2 < \bar{\tau}_3 < \ldots \bar{\tau}_{N-1} < \bar{\tau}_N = 1$$

The state and control vectors at time t_k are now defined as $\mathbf{x}_k \in \mathbb{R}^{N_S}$ and $\mathbf{u}_k \in \mathbb{R}^{N_C}$, respectively. The vector of decision variables is composed of the states and controls over all nodes, as well as the final time t_f, so that $\mathbf{X} \in \mathbb{R}^{N_D}$ with $N_D = N(N_S + N_C) + 1$.

$$\mathbf{X} = \left[\mathbf{x}_1^T, \mathbf{x}_1^T, \mathbf{u}_2^T, \mathbf{u}_2^T, \ldots \mathbf{x}_N^T, \mathbf{u}_N^T, t_f\right] \tag{5.1}$$

We can now use Simpson's rule to integrate the dynamic equations. The original dynamic constraint is: $\dot{\mathbf{x}}(t) = \mathbf{f}(\mathbf{x}(t), \mathbf{u}(t), t)$. Applying Simpson's rule to the discrete system, we have:

$$\dot{\mathbf{x}}_k \approx \frac{\mathbf{x}_{k+1} - \mathbf{x}_k}{\Delta t_k} = \frac{1}{6}\left[\mathbf{f}_k + 4\mathbf{f}_{mk} + \mathbf{f}_{k+1}\right] \tag{5.2}$$

where

$$\mathbf{f}_k = \mathbf{f}(\mathbf{x}_k, \mathbf{u}_k) \tag{5.3}$$

$$\mathbf{f}_{mk} = \mathbf{f}(\mathbf{x}_{mk}, \mathbf{u}_{mk}) \tag{5.4}$$

$$\mathbf{x}_{mk} = \frac{1}{2}(\mathbf{x}_k + \mathbf{x}_{k+1}) - \frac{1}{8}(\mathbf{f}_{k+1} - \mathbf{f}_k)\Delta t_k \tag{5.5}$$

$$\mathbf{u}_{mk} = \frac{1}{2}(\mathbf{u}_k + \mathbf{u}_{k+1}) \tag{5.6}$$

$$\Delta t_k = (\bar{\tau}_{k+1} - \bar{\tau}_k)t_f \tag{5.7}$$

These equations of motion provide a set of nonlinear constraint equations, $\mathbf{C}_\mathbf{f}(\mathbf{X}) = 0$. Rearranging Eq. (5.2), the k^{th} set of equations are given as:

$$\mathbf{C}_{\mathbf{f},k} = \mathbf{x}_{k+1} - \mathbf{x}_k - \frac{1}{6}\left[\mathbf{f}_k + 4\mathbf{f}_{mk} + \mathbf{f}_{k+1}\right]\Delta t_k = 0, \qquad k \in [1, N-1] \tag{5.8}$$

The performance index, originally defined in Eq. (4.12), is now equivalently defined as:

$$J(\mathbf{X}) = K_t t_f + K_p \sum_{k=1}^{N-1} T_k V_k \tag{5.9}$$

The parameter optimization problem is to choose a decision vector $\mathbf{X}$ that minimizes the above performance index, subject to a set of nonlinear constraints of the form $\mathbf{l} \leq \mathbf{C}(\mathbf{X}) \leq \mathbf{u}$, where $\mathbf{l}$ and $\mathbf{u}$ are fixed lower and upper bounds, respectively. The full set of constraints includes the equations of motion, the control rate limits, path constraints on climb rate and power, and the terminal constraints ($\mathbf{C}_\mathbf{t}$). The problem can now be stated as:

$$
\begin{aligned}
\min_{\mathbf{X}} \quad & J(\mathbf{X}) \\
\text{Subject to} \quad & \mathbf{f}_L \leq \mathbf{C}_{\mathbf{f}}(\mathbf{X}) \leq \mathbf{f}_U \\
& \mathbf{c}_L \leq \mathbf{C}_{\mathbf{c}}(\mathbf{X}) \leq \mathbf{c}_U \\
& \mathbf{p}_L \leq \mathbf{C}_{\mathbf{p}}(\mathbf{X}) \leq \mathbf{p}_U \\
& \mathbf{t}_L \leq \mathbf{C}_{\mathbf{t}}(\mathbf{X}) \leq \mathbf{t}_U \\
& \mathbf{X}_L \leq \mathbf{X} \leq \mathbf{X}_U
\end{aligned}
\tag{5.10}
$$

where $\mathbf{X}_L$ and $\mathbf{X}_U$ are the lower and upper bounds on the decision variables across all nodes, $\mathbf{C}_{\mathbf{c}} \in \mathbb{R}^{(N-1)N_C}$ is the set of rate limits on N_C controls, $\mathbf{C}_{\mathbf{p}} \in \mathbb{R}^{NN_P}$ is the set of N_P path constraints over N nodes, and $\mathbf{C}_{\mathbf{t}} \in \mathbb{R}^{N_T}$ is the set of N_T terminal constraints. Here, $N_P = 2$ for path constraints on climb rate and power, and $N_T = 4$ for terminal constraints on latitude, longitude, altitude, and inertial airspeed. The bounds on the initial state are included in $\mathbf{X}_L, \mathbf{X}_U$.

The k^{th} set of dynamic constraints are given in Eq. (5.8). Because these are equality constraints, we have $\mathbf{f}_L = \mathbf{f}_U = 0$. The k^{th} set of control rate bounds, expressed as $\mathbf{c}_{L,k} \leq \mathbf{C}_{\mathbf{c},k} \leq \mathbf{c}_{U,k}$, are given as:

$$
\begin{bmatrix} \dot{T}_{\min} \\ \dot{\alpha}_{\min} \\ \dot{\mu}_{\min} \\ \dot{\psi}_{\min} \end{bmatrix}
\leq
\begin{bmatrix} (T_{k+1} - T_k)/\Delta t_k \\ (\alpha_{k+1} - \alpha_k)/\Delta t_k \\ (\mu_{k+1} - \mu_k)/\Delta t_k \\ (\psi_{k+1} - \psi_k)/\Delta t_k \end{bmatrix}
\leq
\begin{bmatrix} \dot{T}_{\max} \\ \dot{\alpha}_{\max} \\ \dot{\mu}_{\max} \\ \dot{\psi}_{\max} \end{bmatrix}, \qquad k \in [1, N-1]
\tag{5.11}
$$

The k^{th} set of path constraints are taken from Eq. (4.5) and Eq. (4.6), so that $\mathbf{p}_{L,k} \leq \mathbf{C}_{\mathbf{p},k} \leq \mathbf{p}_{U,k}$ is equivalent to:

$$
\begin{bmatrix} \dot{h}_{\min} \\ 0 \end{bmatrix}
\leq
\begin{bmatrix} V_k \sin \gamma_k \\ T_k V_k \end{bmatrix}
\leq
\begin{bmatrix} \dot{h}_{\max} \\ P_{\max} \end{bmatrix}, \qquad k \in [1, N]
\tag{5.12}
$$

Finally, the terminal constraints are taken from Eq. (4.7) through Eq. (4.10). As with the dynamics, these are enforced as equality constraints, so $\mathbf{t}_L = \mathbf{t}_U = 0$.

For numerical solutions, we discretize the problem over 60 nodes and use SNOPT to compute optimal trajectories for various sets of initial conditions and cost functions.

Chapter 6

Numerical Solution Results

For all problems considered, the target position is fixed at 35^o latitude, -118^o longitude, and 21.334 km altitude. We impose an additional terminal constraint that the final Earth-relative velocity be less than 10 m/s. The airship is initialized in level flight at 1 m/s airspeed, and at an altitude of 710 meters to match the local elevation. The initial heading is open. The scaling parameters and constants are defined in Table 6.1, and the bounds on state variables, control inputs, control rates, climb rate and supplied power are provided in Table 6.2.

Table 6.1: Solution Parameters

Parameter	Value
k	20
R	6,356,766.0 m
g	9.82 m/s/s
V_c	395.0425 m/s
d_c	15,891.915 m
t_c	40.228 s

Table 6.2: Problem Bounds

Min	Variable	Max	Units
0.1	V	30	m/s
-30	γ	30	deg
-10	$\dot{h}$	10	m/s
0	P	100	kW
0	T	10	kN
-10	α	10	deg
-90	μ	90	deg
-0.5	$\dot{\alpha}$	0.5	deg/s
-3.0	$\dot{\mu}$	3.0	deg/s
-1.0	$\dot{T}$	1.0	kN/s
-0.6	$\dot{\psi}$	0.6	deg/s

In solving the optimal control problems, we neglect the contribution from centripetal acceleration (those terms from Eqs. (3.37) through (3.39) with ω_E^2). This acceleration is constant in the ENU frame, with a magnitude of 0.029 m/s^2, and components only in the North/South and vertical directions. The upward vertical component is assumed to be a tiny part of the buoyancy that cancels with gravity. The component in the North/South direction acts in the lateral direction of the airship for East/West flights, with a magnitude of about 0.014 m/s/s. These are the only flights considered in this paper for minimum energy scenarios, where the Earth acceleration terms can be significant. We ignore this lateral component in the optimization because it is easily dominated by lateral forces and it cannot be exploited for East/West flights.

Below, we consider four different types of ascent scenarios, all with the same target location but with different initial conditions and different flight objectives.

5 Characteristics of Optimal Flights

We first consider ascent trajectories for two different launch sites, with Scenario 1 launching from 20 km east of the target, and Scenario 2 launching from 250 km west of the target. For each scenario, we consider both minimum-time and minimum-energy flights. Minimum-time ascent flights may be necessary for military missions, where the airship is at risk at low altitudes, or for any time-sensitive application where the payload must be delivered to operational altitude as soon as possible. Minimum-energy flights, on the other hand, would be important for situations when the airship has limited power production capability, such as night launches.

Scenarios 1 and 2 are illustrated in Figure 6.1, where the vertical axis is shown with a larger scale for clarity. Recall that the wind pattern is directed east across all altitudes, with a maximum velocity occurring at around 14 km, as shown in Figure 3.5. In scenario 1, the airship must fly against the wind in order to reach the target. The minimum time solution takes 1 hour and 10 minutes, with the airship flying at the maximum flight path angle of 30 deg and using maximum power for the duration of the flight. Although

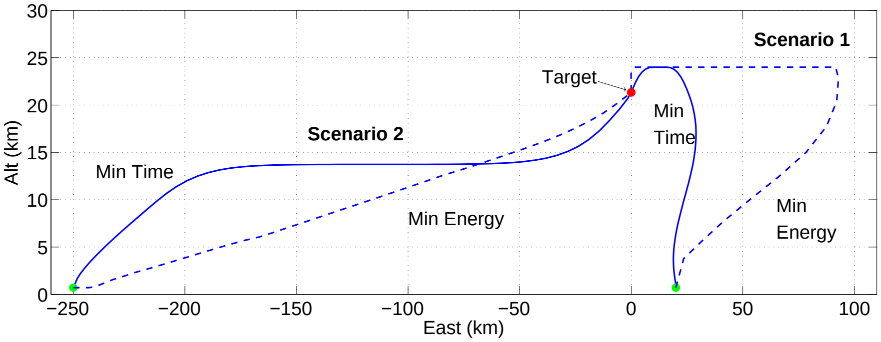

Figure 6.1: Scenarios 1 & 2, Minimum Time and Fixed-Time / Minimum Energy Trajectories

the wind blows the airship further east of its launch point, the airship wind-relative heading is aligned west at all times. This can be seen in the ascent path of the Scenario 1 minimum-time solution in Figure 6.2, which shows the orientation of the airship at points along the trajectory.

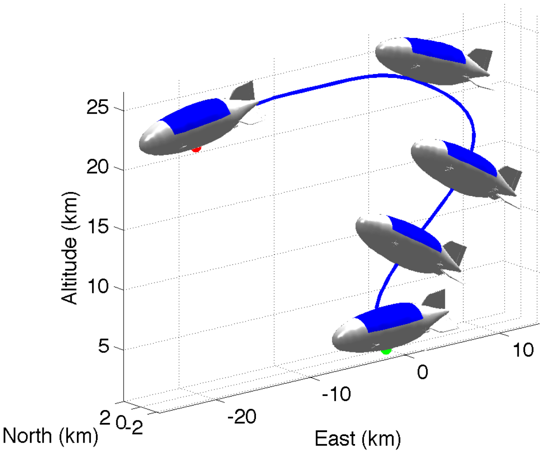

Figure 6.2: Scenario 1 Minimum-Time Ascent Path

In scenario 2, the airship launches much further away at 250 km, but is able to fly with the wind for the entire flight. The minimum time trajectory takes 2 hours. The airship first saturates thrust at 10 kN, then immediately reaches the maximum flight path angle of 30 deg. It continues to accelerate and reaches the power limit of

100 kW after 12 minutes. It then cruises at the jet stream altitude of 14 km for about 45 minutes, covering a range of 120 km, and finally climbs to the target station. The control history for this minimum time case of Scenario 2 is shown in Figure 6.3, and time histories for velocity, flight path angle, climb rate and power are shown in Figure 6.4. The Earth-relative heading, flight path angle and velocity are shown as dashed lines.

It is interesting to observe the use of angle of attack as a control. In this and in all other simulations, the angle of attack is set to -0.78 deg for almost the entire trajectory, which is the minimum drag angle for the polynomial approximation of drag coefficient used from [2]. Longitudinal control is achieved primarily by throttling thrust and rotating the thrust vector through μ. Aerodynamic lift and drag are used sparingly. In this case, angle of attack control is used only at the end of the trajectory to reduce speed, so that the final Earth-relative velocity constraint of < 10 m/s can be met.

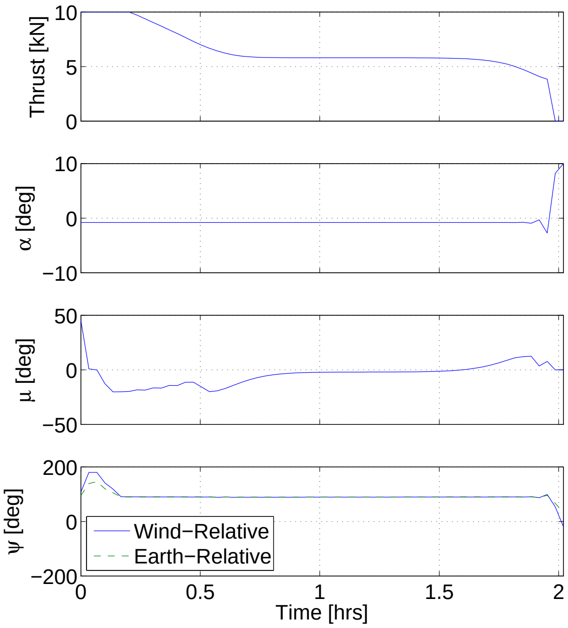

Figure 6.3: Scenario 2, Control History for Minimum Time Solution

For the minimum energy flight of scenario 2, the control histories are plotted in Figure 6.5 and additional time histories are given in Figure 6.6. The trajectory begins

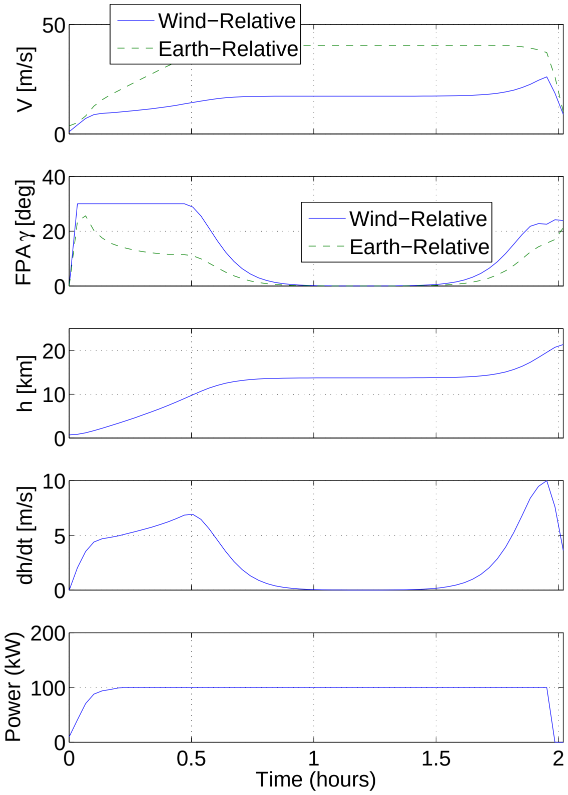

Figure 6.4: Scenario 2, Selected Time Histories for Minimum Time Solution

with the airship flying 1 m/s to the east. While the airspeed stays below 5 m/s during the flight, the Earth-relative velocity increases to nearly 30 m/s, before decreasing to the maximum terminal constraint of 10 m/s. A sequence of small thrusts is applied in the first half hour to initiate the climb. The airship continues to climb at the maximum flight path angle for the duration of the flight. A small amount of downward thrust is applied again between 3 and 4 hours in order to prevent the flight path angle from increasing above its limit. The airspeed velocity is seen to increase steadily throughout the flight, even when no thrust is applied. This is possible because the minimum energy solution intentionally avoids the use of thrust and instead exploits the accelerations due to mass flow rate, Coriolis effects, and wind rates. The Earth-relative heading stays near 90 degrees for the entire flight, as the airship always travels east with the wind, although the wind-relative heading changes several times. When the airship flies north or south, the wind rate terms vanish because the wind model used here is only directed to the east. In addition, the heading angle has a direct impact on the magnitude of Coriolis acceleration in the x direction. In this way, the heading angle provides a small amount of longitudinal control. A perspective view of the ascent trajectory for this scenario is shown in Figure 6.7. It illustrates the changing wind-relative heading of the airship during its ascent.

For scenario 1, where the launch location is 20 km downwind, the airship is carried past the target by the wind. It therefore must expend a certain amount of energy to return to the target, regardless of the time of flight. The control history for the minimum energy solution of scenario 1 is given in Figure 6.8, and additional time histories are provided in Figure 6.9. The first two hours are spent climbing to the pressure altitude of 24 km. The Earth-relative heading angle during this time is at 90 deg, meaning the airship flies east with the wind as it climbs. Once it reaches the maximum altitude, just before 2 hours, it turns west and flies at about 7 m/s for the next 10 hours, covering a distance of over 90 km, until it finally descends to the target station. A perspective view of the ascent trajectory is shown in Figure 6.10, which shows the changing wind-relative

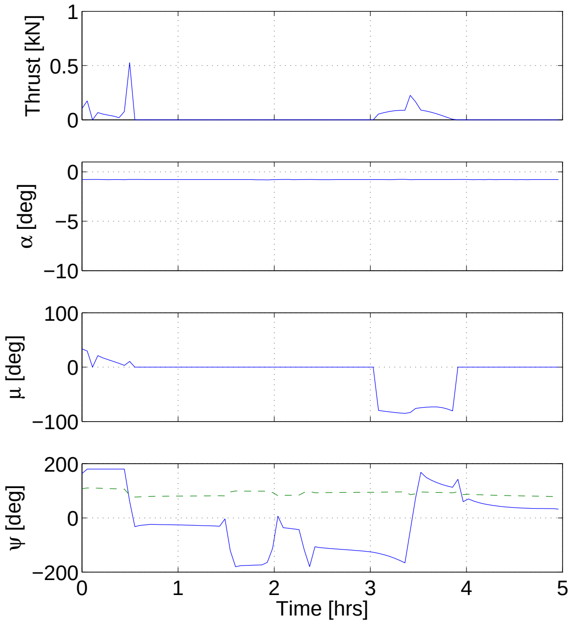

Figure 6.5: Scenario 2, Control History for Minimum Energy Solution

heading of the airship as it climbs and turns.

It is interesting to compare the relative magnitude of the various components of acceleration that the airship experiences. Consider the acceleration in the x direction of the wind-frame for the minimum time and minimum energy (5 hours) solutions of scenario 2, as shown in Figure 6.11. The effects due to mass flow rate and wind rates are clearly comparable to the net effect of thrust and drag. For the minimum time solution, the maximum acceleration due to Earth's rotation is about one order of magnitude smaller than the other components, at 1E-03. For the minimum energy solution, however, its magnitude is comparable to the other components. While the effects of Earth rotation and mass flow rate do not provide a dominating influence, these relative magnitudes suggest that they ought to be incorporated into the trajectory planning process along with the wind rates.

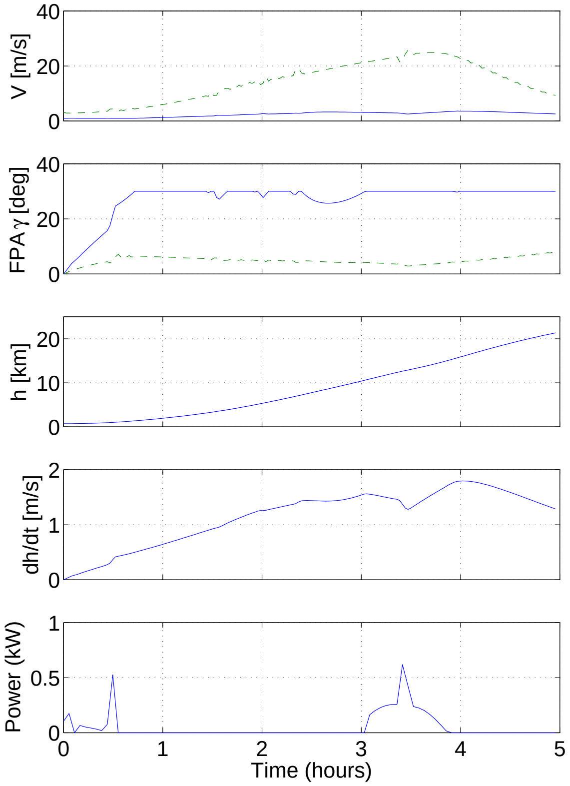

Figure 6.6: Scenario 2, Selected Time Histories for Minimum Energy Solution

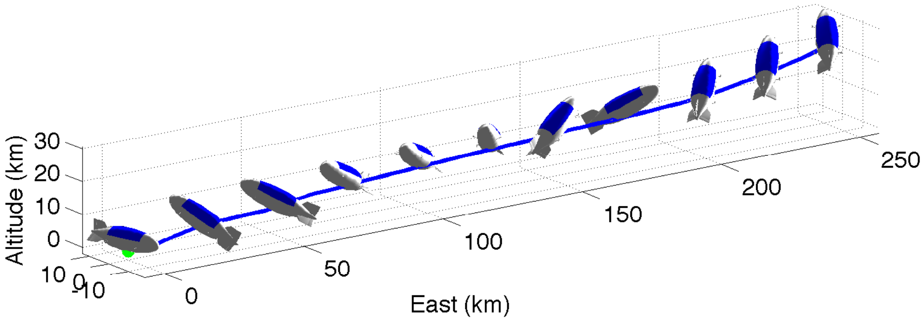

Figure 6.7: Scenario 2, Minimum Energy 3D Ascent Trajectory

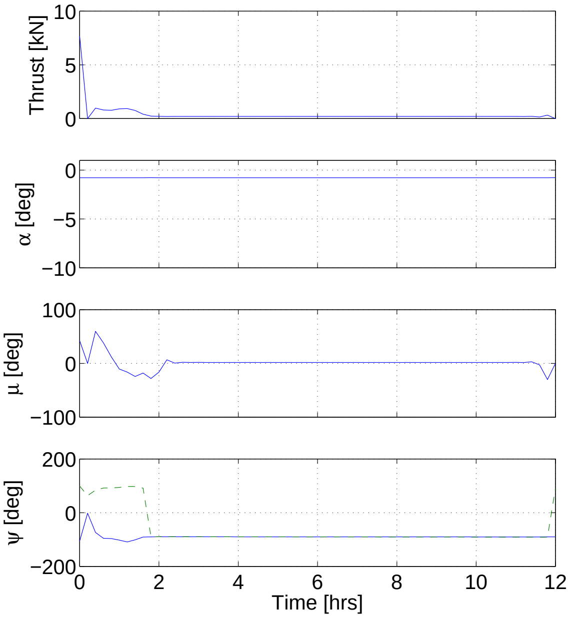

Figure 6.8: Scenario 1, Control History for Minimum Energy Solution

6 Time and Energy Tradeoff

For scenarios 1 and 2, we now consider minimum energy trajectories at a series of specified flight times, extending to a maximum flight time of 12 hours. Figure 6.12 shows the initially steep and then gradual energy reduction with increasing flight time for both scenarios. For scenario 1, the energy continues to decrease with increasing the flight time, but extending the flight to 16 hours provides only a 2.5% further decrease in energy. The minimum energy solutions of scenario 1 follow a similar path to that of the minimum time case, but climb at slower airspeeds to reduce drag, which results in the jet stream winds carrying the airship further east. In all cases, the optimal trajectory involves a direct climb to the maximum operational altitude of 24 km, followed by a cruise and descent to the target station.

For the minimum energy trajectories of scenario 2, there is a steep decline in the energy requirement from 2 to 4 hours. The energy reaches a minimum between 5 and 6 hours, and then gradually increases with larger flight time. The zoomed-in view of

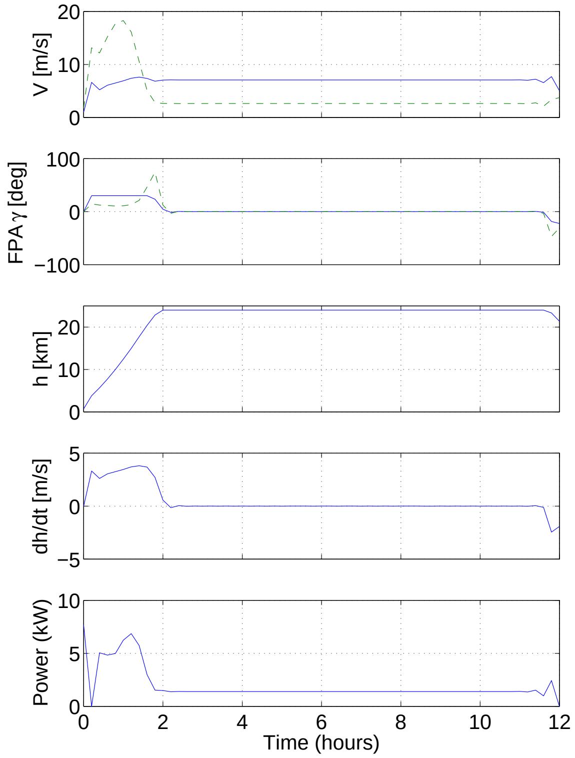

Figure 6.9: Scenario 1, Selected Time Histories for Minimum Energy Solution

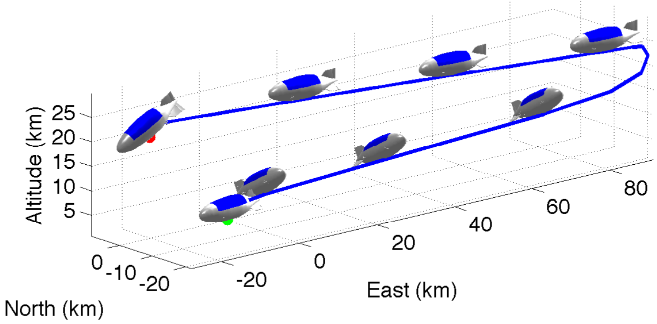

Figure 6.10: Scenario 1, Minimum Energy 3D Ascent Trajectory

Figure 6.11: Scenario 2, Acceleration Components for Minimum Time and Minimum Energy Solutions

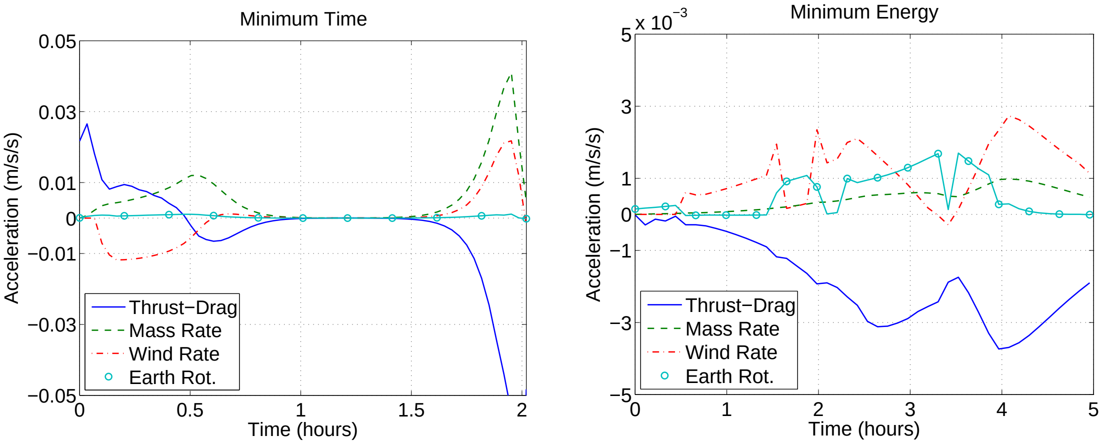

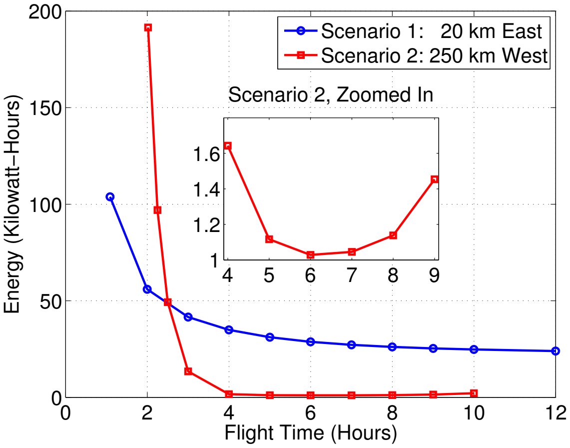

Figure 6.12: Scenarios 1 & 2, Energy vs. Time

the energy curve for Scenario 2 clearly shows the energy increasing after 6 hours. The minimum energy solution requires just 0.5% of the energy required for the minimum time case. For this solution, the vehicle climbs slowly at low airspeeds, eventually entering the jet stream and allowing the wind to carry it to the target. For flight times less than 5-6 hours, additional energy must be expended to increase the eastward velocity. For longer flight times, additional energy is required to decrease the eastward velocity. In general, the airspeeds stay very low, between 1-4 m/s, so that there is very little drag (100-350 N). The small deceleration due to this drag is comparable to the accelerations associated with wind rate, Coriolis effect, and mass flow rate. Thus, thrust is used sparingly in order to maintain a small, positive rate of climb as it coasts to the target.

These results indicate that, unless seriously pressed for time, optimal airship ascent operations should be designed at the minimum energy points, with a maximum flight time constraint applied if necessary. At these conditions, the energy consumption is greatly reduced for a reasonable time penalty.

7 Effects of Varying Initial Positions

The previous sections focus on scenarios that primarily involve east/west motion with an eastward wind. We now consider the effect of changing the initial heading of the launch location. In Scenario 3, trajectories are planned for launch sites distributed along a circular region with the radius of 10 km from the target, and in Scenario 4 the radius is increased to 100 km.

A set of 12 different trajectories are shown in Figure 6.14 for the 10 km range case. The shaded bar on the side of the figure is provided to illustrate the flight time of each trajectory. The left hand plot shows the horizontal projection of each path, while the right hand plot provides a perspective view. As we would expect, initial positions to the west of the target location result in shorter flight times, as they enable airships to fly with the wind during most of the flight. The trajectory launched from the due west location winds back and forth during its ascent. This is necessary in order to achieve the maximum climb rate while preventing the airship from flying too far east, much like winding up or down a mountain with a fixed slope.

Similar results are observed for the 100 km range case, scenario 4. A set of 24 trajectories are shown in Figure 6.13, with the flight time ranging from about 1 to 2 hours. Here, we also observe a transition between two types of trajectories. For the launch sites located furthest to the west, the minimum time ascent involves a consistent climb to the target altitude, with a greater distance covered in the jet stream altitudes. However, as the launch point moves east, the nature of the optimal solution changes. As the launch position moves around the circle towards the east, we reach a condition where the fastest path involves first climbing above the target altitude to the altitude ceiling, then descending to the station. Note that this is the type of altitude profile observed for all cases of scenario 1. The reason for this behavior is due to the fact that the maximum power constraint for the minimum time solution is active for nearly the entire flight (see Figure 6.3). With the power constraint reached, the only way to increase the velocity is to reduce the thrust. This is only possible by elevating to lower density air where the drag for a given velocity is lower.

Figure 6.13: Scenario 4, Minimum Time Ascent Trajectories from 100 km Radius

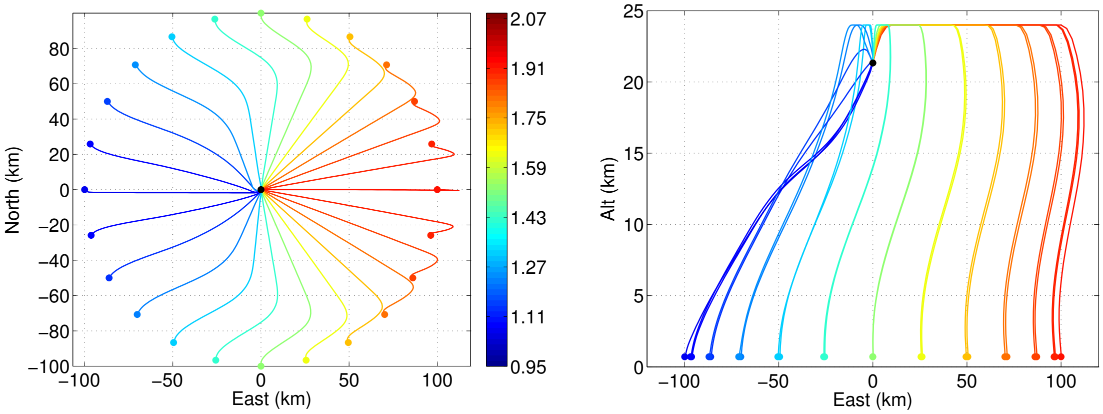

In Figure 6.15, we see that the flight time and total energy follow the same trend with launch location. This is to be expected, because in all cases the objective is to minimize

Figure 6.14: Scenario 3, Minimum Time Ascent Trajectories from 10 km Radius

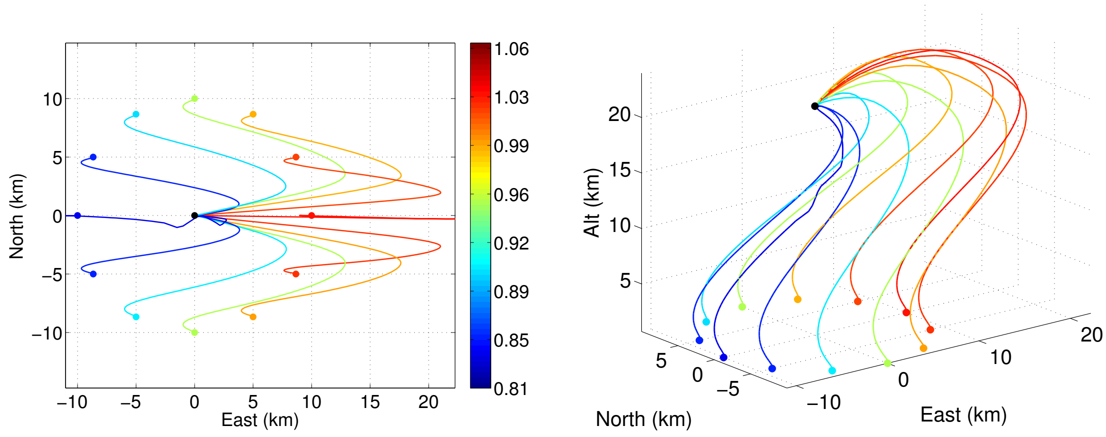

flight time. The associated structure of the control is also the same in all cases, with the power constraint active for nearly the entire flight. Thus, the total energy (the integral of the power) is expected to depend linearly on the flight time.

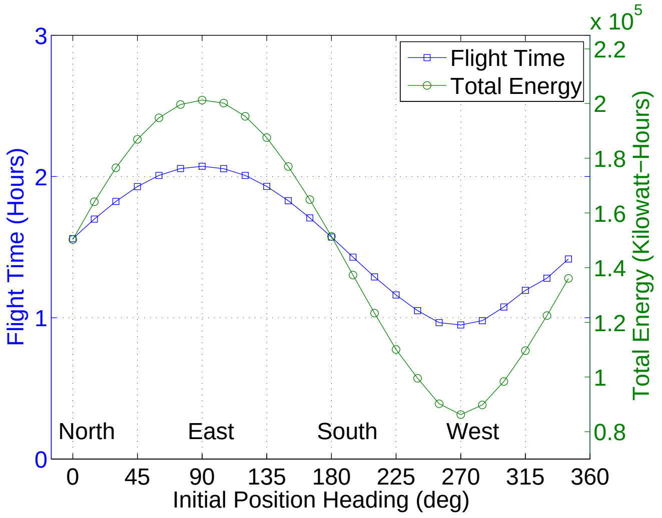

Figure 6.15: Scenarios 4, Energy & Time vs. Launch Location

Clearly, the jet stream provides a speed advantage only if the final altitude could be reached before the final longitude is reached. In these cases, the airship can reduce the rate of climb while in the jet stream altitudes to utilize the wind. This is seen in the far west launch locations of scenario 4, and in the minimum time solution of scenario 2. Here, the launch location is far enough away that, with the fastest possible climb, the final altitude would be reached before the final longitude is reached. Otherwise, there is no advantage to staying in the jet stream, and the optimal solution is simply to climb as fast as possible. Since the jet stream winds carry the airship further east of the target station in these cases, the final phase of the flight involves flying into the wind at maximum power, and sometimes at maximum airspeed. This final return phase involves a cruise at the maximum altitude where the resisting wind and density is smallest.

8 Discussions

Results obtained in this paper are specific to the wind model and airship configuration that was used. However, the wind model is representative of the class of wind profiles that are seen throughout many parts of the globe, and the airship design is based upon published data from prototype vehicles as well as accumulated engineering experience from prior work in airship research. Therefore, examination of these optimization results enables us to develop some general strategies for planning optimal ascent trajectories subject to similar wind profiles and similar vehicle designs.

There are also some important limitations to the scope of this analysis. First, neutral buoyancy has been assumed at all flight conditions, which requires the pressure regulation system to achieve high mass flow rates during high rates of climb, or more precisely whenever the rate of change in the ambient air density is high. A more accurate model would include air flow constraints, so that buoyancy and weight are modeled separately. In such a model, neutral buoyancy conditions would only be achieved when the required mass flow rate is under the prescribed limit. Also, as previously mentioned, our model for the required power for flight does not include the operation of fans for pressure regulation. Including this power requirement in the performance objective would lead to more accurate predictions of energy consumption, and may influence the optimal trajectories. Finally, the power generation during the flight of a stratospheric airship depends upon its orientation, which governs the incidence angles of the photovoltaic solar cells. Introducing a model for the generated power and including appropriate energy balance constraints may lead to a different class of optimal trajectories that exploit the combination of the wind-relative and inertial orientations as the sun moves through the sky. Each of these areas are topics worthy of future research.

Chapter 7

Performance Evaluation of Optimal Solutions

7.1 Introduction

In this chapter, we seek to analyze some performance aspects of the optimal ascent trajectories developed earlier. Two different types of analyses are conducted. First, we develop a model to compute the solar flux available to the airship, and use this model to approximate the solar power and cumulative energy that the airship can generate during an ascent trajectory. This analysis is performed for a variety of ascent trajectories in order to identify how the vehicle orientation and flight profile can impact its power production, and to determine whether batteries are needed for ascent. Solar power modeling for airships has been presented before [3, 4, 5, 29], but the analysis here provides a more general model that includes seasonal and diurnal effects, hull geometry effects, atmospheric losses, and the attitude of the vehicle.

In the second analysis, we consider changes to the drag coefficient and the wind model, and attempt to quantify how these changes impact the performance of the optimal trajectories. To do this we conduct a new series of trajectory optimizations, each with respect to a different model perturbation. This exercise allows us to determine the sensitivity of the optimal solutions to changes in uncertain parameters.

7.2 Energy Production Analysis

Optimal ascent trajectories have been developed for a variety of different scenarios. Minimum time and minimum energy flights were planned from launch sites located downwind and upwind of the target station, and minimum time flights were found for an array of launch sites that surrounded the target station. It was found that minimum-time flights spend much of their time operating at the maximum power constraint, which was set at 100 kW to match the conceptual design in Ref. [2]. Given the large amount of energy required for these flights, it is important to understand how much energy can be supplied from solar power. If the solar energy production is insufficient for daytime ascents, batteries will be required.

In this section, we use the solar flux model developed in Section 3.5 to analyze the energy production capability associated with a set of optimal trajectories from Ref. [17]. A plot of the minimum time trajectories for 24 launch sites at a 100 km radius from the target station is shown in Figure 6.13. The flight paths are shaded according to the flight times, shown in hours in the shaded legend bar.

The propulsion energy required for each trajectory is

$$E_{\text{Req}} = \int_{t_0}^{t_F} \frac{TV}{\eta_P} dt$$

where η_P is the combined efficiency of the electric motor and propellers. For this analysis we let $\eta_P = 0.65$.

The solar energy that may be generated for each trajectory is

$$E_{\text{Gen}} = \eta_S \int_{t_0}^{t_F} F dt$$

where F is the total solar flux from Eq. (3.64), and η_S is the efficiency of the solar cells. In truth, the efficiency of all cells cannot be accurately modeled as a single parameter.

The efficiency for each cell across the hull will be different, as it will fluctuate with temperature, the solar intensity it feels, and even the speed of the local airflow. However, for the sake of analysis we apply an average value $\eta_S = 0.075$ to all solar cells. This corresponds to thin film solar cells, which can reliably achieve efficiencies as high as 10%.

Using the above formulas, the total energy required for each trajectory is plotted in Figure 7.1 along with the total energy generated, for both summer and winter conditions. We assume the trajectories begin at 11 a.m. There are three important observations we can make. First, both the required and generated energy curves follow the same trend with initial position, achieving maxima at the east launch site and minima at the west launch site. This is primarily due to the fact that the wind is directed eastward over all altitudes, so that launches from the west enable the airship to fly with the wind throughout the entire flight, reducing the flight time. The reduced flight time means that both required power and generated power are integrated over shorter times, so both energies are reduced.

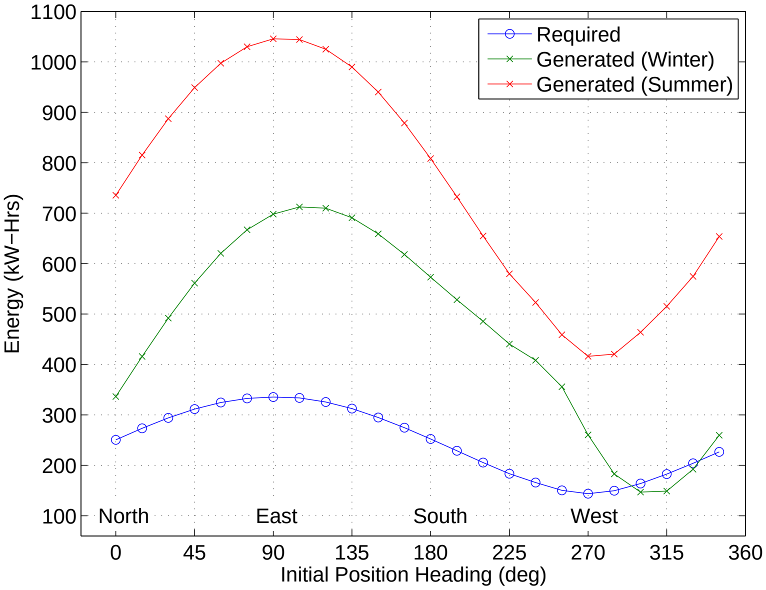

Figure 7.1: Required and Available Energy for Minimum Time Flights

The second observation we can make is that for the winter case, the generated power drops sharply for launch sites between 270 deg and 360 deg. This is because the airship is climbing at a pitch angle of 30-40 degrees during ascent, and for these launch sites, the vehicle is facing a southern direction. Thus, at this northern latitude in the winter, the inclined pitch angle with a south heading blocks much of the top-mounted solar cells from the sun.

Finally, we see that the energy generated for nearly all flights considered surpasses the energy requirement. This provides confirmation that the baseline design configuration should adequately meet the energy demands of minimum-time ascent trajectories. However, these results are based upon an assumption of constant efficiency for the motors, propellers, solar cells. If the true efficiencies are significantly below the assumed values, then solar energy production may prove insufficient for these minimum-time flights.

1 Energy Requirement for Ballast Control

The energy requirement considered thus far is limited to that required for propulsion. It is instructive to also consider the energy required to move air in and out of the ballonets. To do so, we develop a simple model which provides a reasonable approximation. If the mass flow rate is directed vertically down, then the force associated with the air flow is $|\dot{m}\dot{h}|$. This force must act over each incremental change in altitude. The total energy required for ballast control, therefore, is the work done by this force over altitude. Letting $dh = \dot{h}dt$, the expression becomes:

$$E_{\mathrm{BC}} = \int_{t_0}^{t_F} |\dot{m}|\dot{h}^2 dt$$

For neutral buoyancy, the mass of the enclosed airship (including ballast air in the ballonets) must equal the mass of displaced air. The mass flow rate of the airship is therefore equivalent to the mass rate of change of the displaced air:

$$\begin{aligned} \dot{m} &= U_H \dot{\rho} \\ &= U_H \frac{\partial \rho}{\partial h} \dot{h} \end{aligned} \tag{7.1}$$

The ballast control energy can now be written as:

$$E_{\mathrm{BC}} = U_H \int_{t_0}^{t_F} |\frac{\partial \rho}{\partial h} \dot{h}^3| dt$$

Consider the launch site located 100 km due east of the station. The total energy required for this flight is just over 200 kW-Hrs, neglecting efficiency losses. The mass flow rate and associated energy required for ballast control during this flight is shown in Figure 7.2. The total energy reaches just 4 kW-Hrs, only 2% of the total propulsive energy requirement. This indicates that ballast control energy can safely be neglected when estimating the energy for minimum time flights. For minimum energy flights, it can become somewhat more significant. In the cases analyzed thus far it reaches up to 10% of the total propulsive energy.

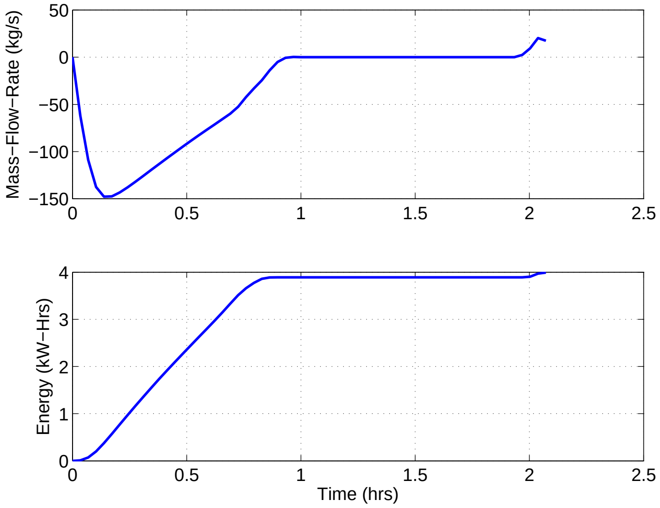

Figure 7.2: Energy Required for Ballast Control

7.3 Sensitivity Analysis

The optimal solutions found in Ref. [17] are based upon deterministic models of the environment. Although the models used for lift and drag, atmospheric density, and wind velocity are reasonable approximations, the true values experienced during flight will differ from these simplistic models. This is especially true for the wind model, as the actual wind profile for a given day may be quite different from the representative model selected for planning.

It is therefore important to examine the sensitivity of the optimal solutions to changes in model parameters. In this section we present the results from a sensitivity analysis conducted with respect to independent changes in the drag coefficient and the wind profile. Two different optimal flight plans are considered:

1. Minimum-time flight from a launch site 250 km west of the station
2. Minimum-time flight from a launch site 20 km east of the station

The characteristics of the optimal solutions for these two scenarios are discussed extensively in Ref. [17]. In this sensitivity analysis, we introduce small changes to the drag coefficient and wind profile, and then recompute the minimum-time solutions with respect to the changed models. The sensitivity of flight time and total energy consumption for each new trajectory is then illustrated by plotting their changing values against the varying model parameters.

1 Variation in Drag Coefficient

The nominal drag coefficient at zero incidence is 0.04, based upon the aerodynamic model presented in Ref. [2]. We consider a ±50% change in the drag coefficient, so that it can range between 0.02 and 0.06. The sensitivity of flight time and total energy consumption is shown in Figure 7.3.

The results show a relatively small sensitivity to the drag coefficient. For a ±10% change in drag coefficient around 0.04, the optimal flight time for the east launch site changes by about 3.3 minutes, compared with about 1.9 minutes for the west launch site. This is a 5% change for the east site, and only a 1.5% change for the west site. The energy sensitivity follows a similar trend. This is expected as the total energy is roughly proportional to flight time.

Figure 7.3: Sensitivity of Flight Time and Energy to Drag Coefficient

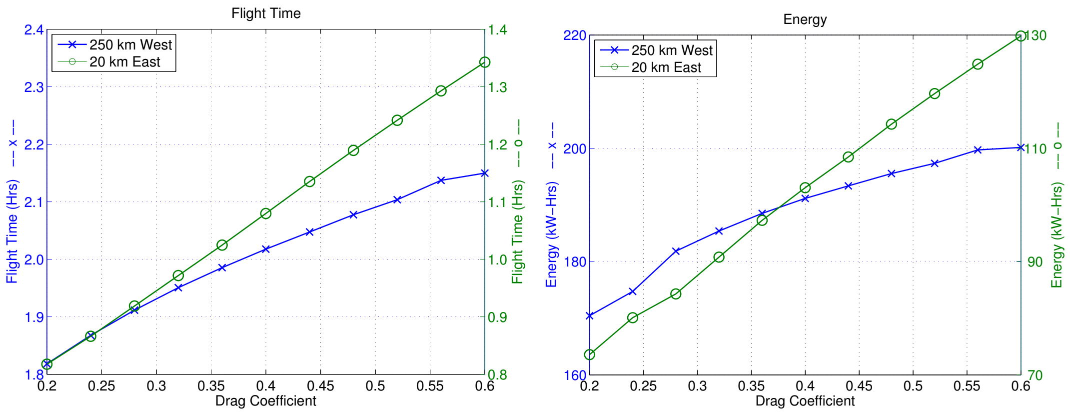

The east launch site trajectories are more sensitive to drag coefficient because they fly at a higher average airspeed velocity. This can be explained by examining the 2D optimal flight paths, shown in Figure 7.4. The trajectories for both cases follow a consistent structure. For the west launch site, the optimal solution is to climb at max power and at max flight path angle until the jet stream altitude is reached, at which point the airship cruises at max power until finally climbing to the station. Because it is already at the maximum power constraint, it cannot increase velocity or thrust, and it cruises at an airspeed of about 17.2 m/s. For the east launch site case, it climbs at the max rate of climb all the way to the target station, increasing airspeed as it goes. It therefore has a higher average airspeed. As drag is proportional to the square of the airspeed, these trajectories are more strongly influenced by changes in the drag coefficient.

2 Variation in Peak Wind Magnitude

The nominal wind profile is based on the HWM93 model for the winter season above Edwards AFB in California, as shown in Figure 3.5. Let us denote this curve as $\bar{W}_E(h)$. We consider incremental changes to this nominal profile by introducing a wind variation

Figure 7.4: Variation of Optimal Flight Paths with Drag Coefficient

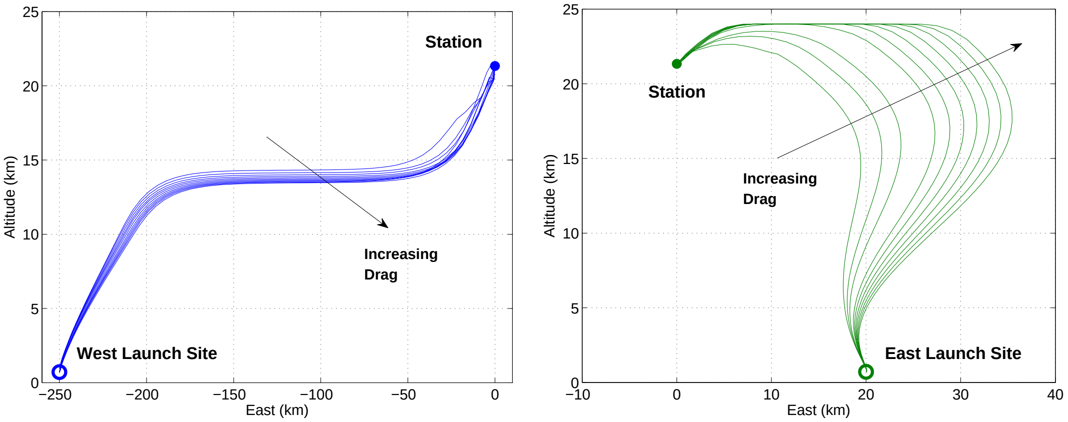

δW_E, so that

$$W_E(h) = \bar{W}_E(h) + \delta W_E(h)$$

The variation is defined as: which is a Gaussian distribution centered at h_{max} with height ΔW_p, and spread across an altitude range of Δh. This enables us to add a smooth variation to the original wind profile, with a desired magnitude change located at a particular altitude. We choose to add the magnitude change at $h_{\text{max}} = 12$ km, which is the altitude of peak wind speed, and we consider 8 different magnitude variations ranging from $\Delta W_p = -5$ to $+5$ m/s. The resulting curve is then fit with a new 7^{th} order polynomial . The curves for all polynomial fits are shown in Figure 7.5.

The sensitivities are shown in Figure 7.6. For the west launch site, increases in the eastward wind reduce the flight time and energy, while they are increased for the east launch site. Again, the sensitivities are relatively small. The flight time and energy for the west site drop by about 1.7% for each 1 m/s increase in the peak wind magnitude. This compares to about 1.0% increase in flight time and energy for the east site.

The 2D optimal flight paths are shown in Figure 7.7. Again, the trajectories follow a consistent structure. For the east launch site, the optimal solution in every case is to climb to the pressure altitude, fly back towards the station, then descend to the target altitude. With the max power constraint reached, the only way to increase the velocity

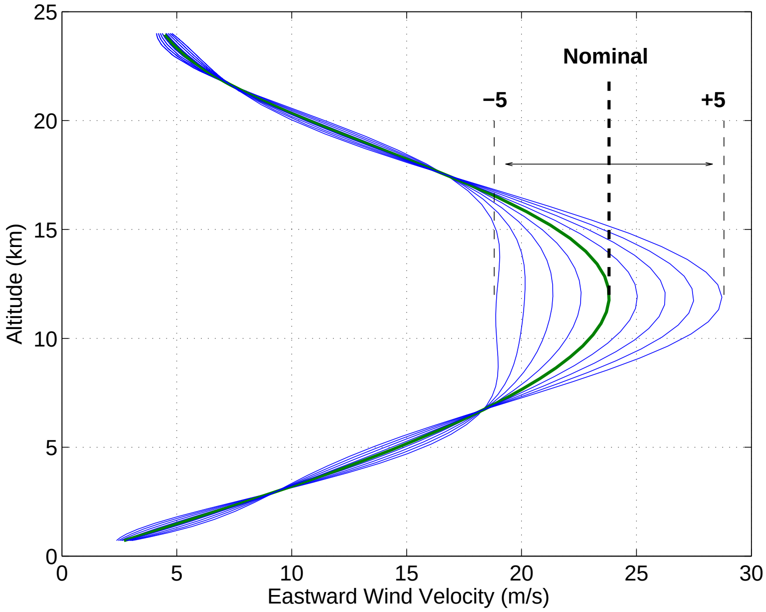

Figure 7.5: Model of Varying Peak Magnitude of the Eastern Wind Velocity

Figure 7.6: Sensitivity of Flight Time and Energy to Changing Winds

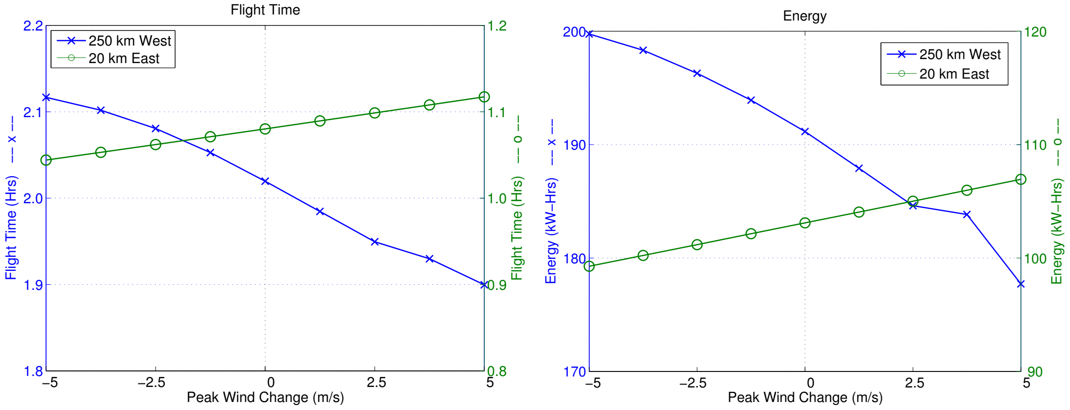

is to reduce the thrust. This is only possible by elevating to lower density air where the drag for a given velocity is lower.

The same principle applies for the west launch site trajectories. The maximum wind speed is always located at about 12 km altitude. It would seem that this would be the ideal altitude for the airship to cruise at until it comes close to the station. However, it can reach a higher airspeed velocity at higher altitudes with lower density, and so it climbs above 12 km. It cannot climb to far, though, as the contribution from the wind speed begins to drop. The cruise altitude in each scenario is therefore the location of the maximum possible total velocity. The airship climbs higher for wind profiles with smaller peaks because the increase in airspeed remains larger than the decrease in wind speed over a larger altitude range.

Figure 7.7: Variation of Optimal Flight Paths with Changing Winds

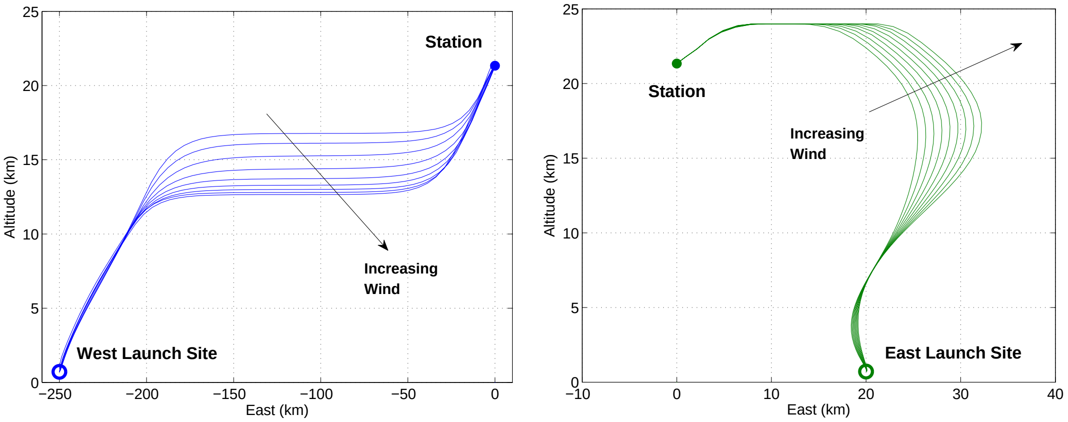

7.4 Concluding Remarks

A model for the solar flux of an ellipsoidal airship hull has been developed, which includes the effects due to geographic latitude, seasonal and diurnal effects that govern the sun motion, the curvature loss for an ellipsoidal hull, and the time-varying orientation of the airship. This model was used to analyze the energy production associated with several minimum-time ascent trajectories. We find that the energy production capability is sufficiently high to meet the energy demands for these trajectories, assuming a mid-day launch time. However, it is also discovered that the steep pitch angle during ascent can result in significant energy loss for certain orientations, particularly south-flying ascents from the northern hemisphere, and vice versa. The sensitivity of the optimal solutions is also examined with respect to changes in drag coefficient and peak wind magnitude. The flight time and total energy of the flights are found to change by only a few percent, and the optimal trajectories retain a consistent structure over all parameter values.

Chapter 8

Onboard Guidance Methods

8.1 Introduction

Optimal ascent trajectories have been presented here and in previous works [2, 17]. The optimal ascent trajectories in Chapter 6 have been found through the numerical solution of optimal control problems. Solutions were obtained by first using collocation to discretize the optimal control problem over a finite number of time intervals, producing a nonlinear parameter optimization problem where nonlinear equality constraints are used to capture the dynamic equations. Each discrete formulation consists of hundreds to thousands of variables and nonlinear constraint equations, requiring a substantial computational effort to reach a solution. In addition, as is often the case in high-dimension nonlinear optimization, reliable convergence requires a good initial guess, which is not trivial to construct. Considering the computational demands and the risk of not obtaining feasible solutions in time to use them, this approach is not well-suited for onboard implementation. One way to implement a form of optimal guidance onboard without this prohibitively high computational burden is by first generating optimal solutions offline. However, in this case each optimal solution would be valid only for a single wind model. Because the wind profile across altitude is uncertain, it would be necessary to pre-compute optimal trajectories for a large number of possible wind profiles.

In this section, an alternative guidance method is presented in which *approximate* optimal trajectories are solved. By characterizing the structure of the original optimal solutions, minimum-time and minimum-energy ascent flights are approximated by piecing together different parameterized flight segments. This greatly simplifies the optimization, leaving only a small number of variables to be decided.

The guidance and control system structure is shown in Figure 8.1. Wind measurements are used to update the onboard wind model, which fits a combination of recorded winds at lower altitudes and the current wind predictions at higher altitudes into a polynomial function. The predicted wind profile and current states are used in an outer loop guidance strategy to determine the desired airspeed, flight path, heading, and altitude. Nonlinear dynamic inversion is then used to command the thrust, thrust pitch angle, and angle of attack in order to track the desired trajectory.

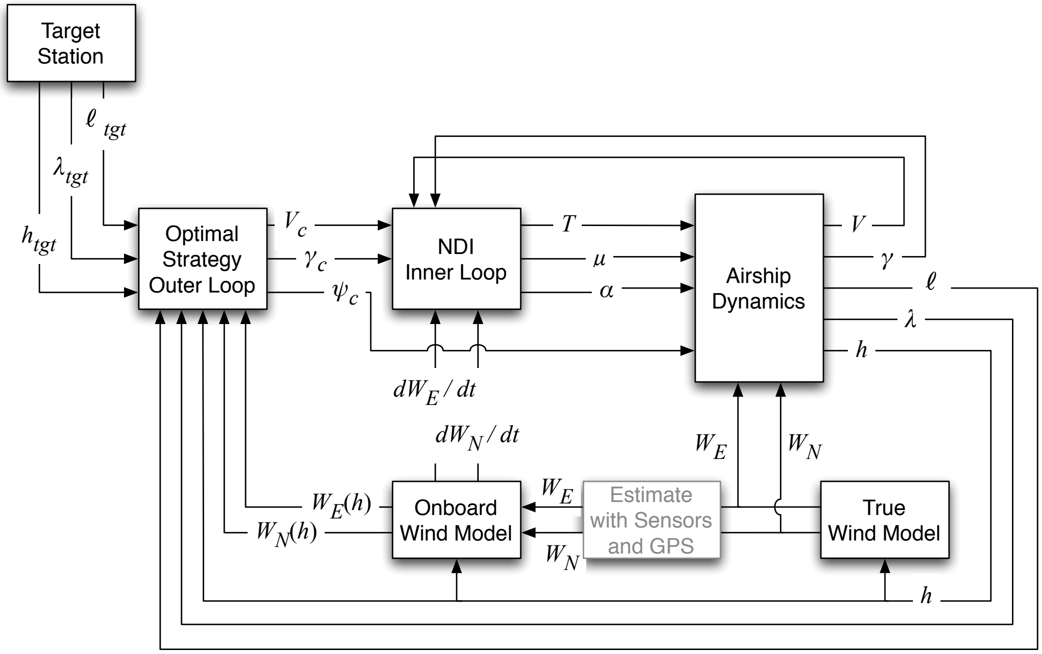

Figure 8.1: Control System Architecture

The onboard guidance strategy integrates an onboard wind model across a candidate altitude profile to predict a wind-relative location for the target station. This *virtual target* station moves gradually as the wind model is updated.

The next section discusses nonlinear dynamic inversion as a guidance method, and how it is applied to our airship dynamic model. The section that follows describes the concept of the virtual target and how it is used in planning optimal ascents.

8.2 Dynamic Inversion

This section describes the use of non-linear dynamic inversion as a feedback control method for autonomous guidance. The goal is to develop a suitable framework for evaluating the performance of the optimal trajectory solutions in closed-loop simulations. As such, the scope is limited to controlling the point mass model of the airship so that it tracks the optimal trajectory. It should be pointed out that the full design of an autonomous guidance system for stratospheric airships would include also GPS navigation, local state estimation, wind estimation, and the use of actuators to control the airship state. However, for the present analysis it is assumed that each of these components may be designed to function sufficiently. The research is instead focused on measuring how deviations from the predicted wind profile will impact the ability of the airship to follow the optimal trajectory, and in general how it will impact certain measures of performance in the closed-loop trajectory.

The concept of *dynamic inversion* is to define the control signal input so that it produces desired dynamics. If the desired dynamics are linear, then the approach may also be referred to as *feedback linearization.* Consider a general dynamic system with state x, output y and input u. We first consider a linear system:

$$\dot{x} = Ax + Bu \tag{8.1}$$

$$y = Cx \tag{8.2}$$

Next, the control signal may be expressed in terms of the output dynamics and the state:

$$\begin{aligned} u &= (CB)^{-1}\left(C\dot{x} - CAx\right) && (8.3) \\ &= (CB)^{-1}\left(\dot{y} - CAx\right) && (8.4) \end{aligned}$$

Let $\dot{y}_{des}$ be the desired time derivative of the output y. Dynamic inversion involves solving for the control signal that achieves the desired output dynamics. The solution is found simply by substituting the desired signal $\dot{y}_{des}$ for the $\dot{y}$ term in Eq. 8.4.

$$u_c = (CB)^{-1}\left(\dot{y}_{des} - CAx\right)$$

Note that the above equation requires matrix CB to be nonsingular. If it is singular, then one may instead attempt to track the second derivative, $\ddot{y}$, which requires the inverse of matrix CAB.

If the system is nonlinear, it may be expressed as follows:

$$\begin{aligned} \dot{x} &= f(x, u) && (8.5) \\ y &= h(x) && (8.6) \end{aligned}$$

The output dynamics are found through the chain rule:

$$\begin{aligned} \dot{y} &= \frac{\partial h}{\partial x}\dot{x} && (8.7) \\ &= \frac{\partial h}{\partial x} f(x, u) && (8.8) \end{aligned}$$

As before, we now use this equation to solve for u in terms of x and $\dot{y}$. Let this solution be expressed in general form as $u = g(x, \dot{y})$. The control signal solution for nonlinear dynamic inversion is then:

$$u_c = g(x, \dot{y}_{des})$$

Whether the dynamic system to be controlled is linear or non-linear, the dynamic inversion method requires the desired signal $\dot{y}_{des}$ to be defined.

1 Airship Dynamic Model

The nonlinear dynamic equations for the airship point mass vehicle are given below:

$$\dot{h} = V\sin\gamma \tag{8.9}$$

$$\dot{\lambda} = \frac{V\cos\gamma\cos\psi + W_N}{R+h} \tag{8.10}$$

$$\dot{\ell} = \frac{V\cos\gamma\sin\psi + W_E}{(R+h)\cos\lambda} \tag{8.11}$$

$$\dot{V} = \frac{T\cos\mu - \frac{1}{2}\rho(h)U_H^{2/3}C_D(\alpha)V^2 - U_H\left(\frac{\delta\rho}{\delta h}\right)\dot{h}V}{m+m_{ax}} - \dot{W}_x \tag{8.12}$$

$$\dot{\gamma} = \frac{T\sin\mu + \frac{1}{2}\rho(h)U_H^{2/3}C_L(\alpha)V^2}{(m+m_{az})V} - \frac{\dot{W}_z}{V} \tag{8.13}$$

Note that in Eq. (8.12), the mass flow rate is expressed as:

$$\begin{aligned} \dot{m} &= \frac{d}{dt}(U_H\rho(h)) \\ &= U_H\dot{\rho}(h) \\ &= U_H\left(\frac{\partial\rho}{\partial h}\right)\dot{h} \end{aligned} \tag{8.14}$$

The wind rate terms in the wind frame are:

$$\dot{W}_x = \dot{W}_E\cos\gamma\sin\psi + \dot{W}_N\cos\gamma\cos\psi \tag{8.15}$$

$$\dot{W}_z = \dot{W}_E\sin\gamma\sin\psi + \dot{W}_N\sin\gamma\cos\psi \tag{8.16}$$

2 Nonlinear Dynamic Inversion for Airship Guidance

The Nonlinear Dynamic Inversion (NDI) approach used for airship guidance was shown in Figure 8.1. The objective of this design is to track the optimal position trajectory that is computed offline by the trajectory optimization program. The commanded 3-dimensional inertial position consists of the altitude h_c, latitude λ_c and longitude ℓ_c. These reference signals are sent to the NDI outer loop control law, which commands the wind-relative velocity vector necessary to track the reference inertial position. The airspeed velocity V_c and flight path angle γ_c outputs from the NDI outer loop controller are then sent to the NDI inner loop controller. In the inner loop control law, the thrust magnitude T_c, thrust pitch angle μ_c and angle of attack α_c are used to track V_c and γ_c.

3 Outer Loop NDI Control

The outer loop NDI control law commands the wind-relative velocity vector that is necessary to achieve the desired rates of the inertial position vector, which includes the $\dot{h}_{des}$, $\dot{\lambda}_{des}$, and $\dot{\ell}_{des}$ signals. Decoupled first order systems are used to define the desired dynamics for tracking each signal.

$$\begin{aligned} \dot{h}_{des} &= K_h\,(h_c - h) && (8.17)\\ \dot{\lambda}_{des} &= K_\lambda\,(\lambda_c - \lambda) && (8.18)\\ \dot{\ell}_{des} &= K_\ell\,(\ell_c - \ell) && (8.19)\\ & && (8.20) \end{aligned}$$

Eq. (8.10) and Eq. (8.11) are rearranged to solve for $\cos\psi$ and $\sin\psi$, respectively.

$$\begin{aligned} \sin\psi &= \frac{(R+h)\cos\lambda\dot{\ell} - W_E}{V\cos\gamma} && (8.21)\\ \cos\psi &= \frac{(R+h)\dot{\lambda} - W_N}{V\cos\gamma} && (8.22) \end{aligned}$$

Replacing the state derivatives with the desired rates and dividing Eq. (8.21) by Eq. (8.22) yields the following solution for the heading command ψ_c.

$$\psi_c = \tan^{-1}\left(\frac{(R+h)\cos\lambda\dot{\ell}_{des} - W_E}{(R+h)\dot{\lambda}_{des} - W_N}\right) \tag{8.23}$$

To solve for V_c and γ_c, the wind-relative velocity vector is first divided into horizontal and vertical components, as follows:

$$\begin{aligned} V_{Horiz} &= V_c\cos\gamma_c = \sqrt{\left[(R+h)\cos\lambda\dot{\ell}_{des} - W_E\right]^2 + \left[(R+h)\dot{\lambda}_{des} - W_N\right]^2} && (8.24)\\ V_{Vert} &= V_c\sin\gamma_c = \dot{h}_{des} && (8.25) \end{aligned}$$

Dividing Eq. (8.25) by Eq. (8.24) yields a solution for the commanded flight path angle:

$$\gamma_c = \tan^{-1}\left(\frac{\dot{h}_{des}}{\sqrt{\left[(R+h)\cos\lambda\dot{\ell}_{des} - W_E\right]^2 + \left[(R+h)\dot{\lambda}_{des} - W_N\right]^2}}\right) \tag{8.26}$$

Finally, computing the magnitude of the horizontal and vertical components yields an expression for the airspeed command.

$$V_c = \sqrt{\left[(R+h)\cos\lambda\dot{\ell}_{des} - W_E\right]^2 + \left[(R+h)\dot{\lambda}_{des} - W_N\right]^2 + \dot{h}_{des}^2} \tag{8.27}$$

Equations (8.23,8.26,8.27) define the wind-relative velocity vector command that is output from the outer loop NDI control law.

4 Inner Loop NDI Control

The inner loop NDI control law commands the thrust magnitude T_c, thrust pitch angle μ_c and angle of attack α_c in order to track the commanded wind-relative velocity components: V_c, γ_c. A diagram of the inner loop NDI control law is shown in Figure 8.2.

The first-order desired dynamics for the inner-loop are:

$$\dot{V}_{des} = K_V\left(V_c - V\right) \tag{8.28}$$

$$\dot{\gamma}_{des} = K_\gamma\left(\gamma_c - \gamma\right) \tag{8.29}$$

$$\dot{\psi}_{des} = K_\psi\left(\psi_c - \psi\right) \tag{8.30}$$

Let the body frame x and z components of the thrust command be $T_x = T_c\cos\mu_c$ and $T_z = T_c\sin\mu_c$. We solve for these quantities directly by using the desired signals $\dot{V}_{des}$ and $\dot{\gamma}_{des}$ in Eq. (8.12) and Eq. (8.13), respectively.

$$T_x = (m+m_{ax})\left(\dot{V}_{des} + \dot{W}_x + a_{Ex}\right) + \frac{1}{2}\rho(h)U_H^{2/3}C_D(\alpha_c)V^2 + U_H(\frac{\partial\rho}{\partial h})\dot{h}V \tag{8.31}$$

$$T_z = (m+m_{az})\left(V\dot{\gamma}_{des} - \dot{W}_z - a_{Ez}\right) - \frac{1}{2}\rho(h)U_H^{2/3}C_L(\alpha_c)V^2 \tag{8.32}$$

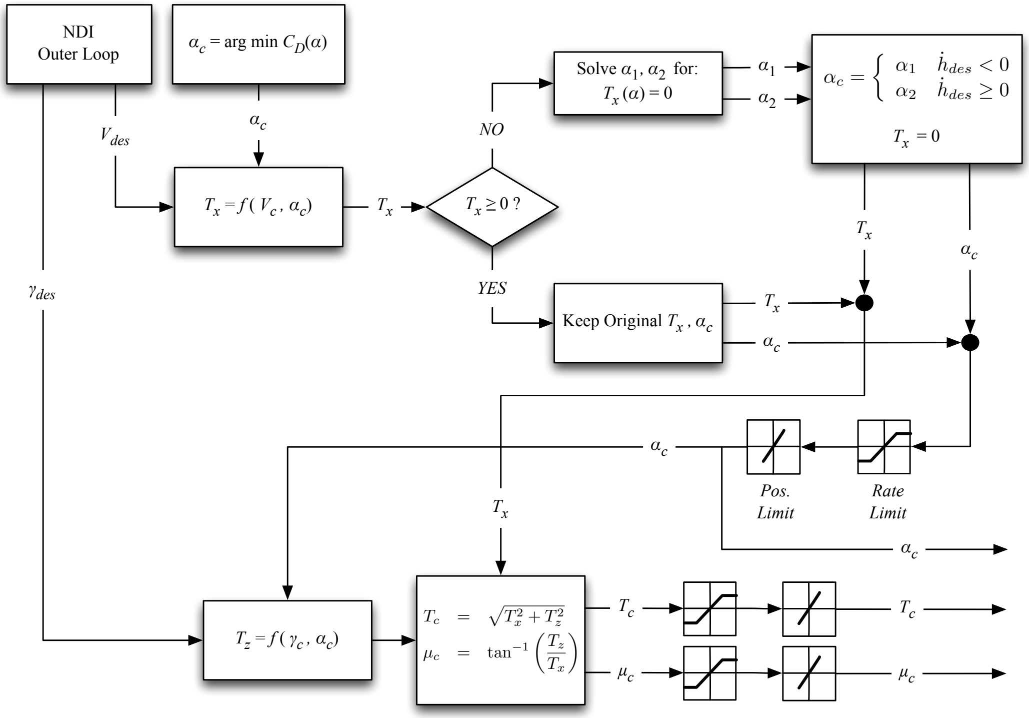

Figure 8.2: NDI Inner Loop Control Law for Minimum-Time

While T_z is unrestricted in sign, we constrain the forward thrust so that $T_x \geq 0$. This ensures that thrust is only used for forward acceleration or for changing the climb rate. Angle of attack control is used to achieve commanded deceleration.

The control allocation procedure is summarized as follows. First, the minimum-drag angle of attack is chosen. This angle is defined as:

$$\begin{aligned} \alpha_{c0} &= \arg\min\left(C_D(\alpha_c)\right) && (8.33) \\ &= \arg\min\left(q_{CD1}\alpha_{c0}^4 + q_{CD2}\alpha_{c0}^3 + q_{CD3}\alpha_{c0}^2 + q_{CD4}\alpha_{c0} + q_{CD5}\right) && (8.34) \end{aligned}$$

Setting the partial derivative with respect to α_{c0} to zero provides the solution.

$$4q_{CD1}\alpha_{c0}^3 + 3q_{CD2}\alpha_{c0}^2 + q_{CD3}\alpha_{c0} + q_{CD4} = 0$$

For the given set of coefficients used in this model, the solution is: $\alpha_{c0} = -0.0136$ radians.

Next, the forward thrust is found by solving Eq. (8.31) with α_{c0}. If this gives $T_x \geq 0$, then the angle of attack command is $\alpha_c = \alpha_{c0}$. If instead this gives $T_x < 0$, the desired $\dot{V}_{des}$ cannot be achieved with forward thrust, and so a larger angle of attack must be used to provide reverse acceleration. The required angle of attack is found by setting $T_x = 0$ in Eq. (8.31) and solving for the two real roots, $\{\alpha_1, \alpha_2\}$, where $\alpha_1 \leq \alpha_{c0}$ and $\alpha_2 \geq \alpha_{c0}$.

$$\alpha_c = \begin{cases} \alpha_1 & \dot{h}_{des} < 0 \\ \alpha_2 & \dot{h}_{des} \geq 0 \end{cases} \quad (8.35)$$

The angle of attack command is then constrained with the proper rate limit and position limit. Next, the required z thrust is computed from Eq. (8.32) in order to achieve $\dot{\gamma}_{des}$ with the known angle of attack command, α_c. The final thrust magnitude and angle commands are computed as:

$$\begin{aligned} T_c &= \sqrt{T_x^2 + T_z^2} && (8.36) \\ \mu_c &= \tan^{-1}\left(\frac{T_z}{T_x}\right) && (8.37) \end{aligned}$$

As with the angle of attack, each of these commands is constrained by its rate and position limit.

Minimizing Thrust Magnitude

The angle of attack command provides an additional degree of freedom. This enables the thrust magnitude to be minimized subject to the above equations, leading to the following convex, constrained minimization:

$$\begin{aligned} \min_{\alpha_c} \quad & T_x(\alpha_c)^2 + T_z(\alpha_c)^2 \\ \text{subject to} \quad & T_x(\alpha_c) \geq 0 \\ & \alpha_{\min} \leq \alpha_c \leq \alpha_{\max} \end{aligned} \tag{8.38}$$

where $T_x(\alpha_C)$ and $T_z(\alpha_C)$ are given by Eq. (8.31) and Eq. (8.32), respectively.

The solution to the unconstrained problem is found by setting the gradient of the cost function to zero. This reduces to:

$$\frac{d}{d\alpha_c}\left(T_x(\alpha_c)^2 + T_z(\alpha_c)^2\right) = 0 \tag{8.39}$$

$$T_x T_x' + T_z T_z' = 0 \tag{8.40}$$

where T_x' and T_z' are the partial derivatives with respect to α_c of T_x and T_z, respectively. The only dependence on α_c appears in the lift and drag coefficients. Therefore these derivatives are:

$$T_x' = \frac{1}{2}\rho(h)U_H^{2/3}V^2\frac{d}{d\alpha_c}\left(C_D(\alpha_c)\right) \tag{8.41}$$

$$T_z' = -\frac{1}{2}\rho(h)U_H^{2/3}V^2\frac{d}{d\alpha_c}\left(C_L(\alpha_c)\right) \tag{8.42}$$

Both the lift and drag coefficients are approximated as 4^{th} order polynomials in α, and so their derivatives with respect to α are 3^{rd} order polynomials. Therefore, Eq. (8.40) is a 7^{th} order polynomial whose roots contain the optimal unconstrained solution. Alternatively, the solution could be obtained through the use of a gradient search method.

If the solution to the unconstrained problem satisfies $T_x \geq 0$ and the angle of attack bounds, then the constrained problem is also solved. If the angle of attack constraint is violated, then α_c is restricted to the nearest bound and both T_x and T_z are computed for this extreme α_c value. If instead the solution has $T_x < 0$, then we apply the constraint $T_x = 0$ and proceed to solve for T_z, α_c. In such a case, the airship requires a reverse acceleration. The strategy in this case is to use drag to achieve as much of the reverse acceleration as possible, which is done by commanding the appropriate angle of attack. Thus, we first solve for α_c that gives the desired $\dot{V}_{des}$ with $T_x = 0$, and limit it to lie within the $[\alpha_{\min}, \alpha_{\max}]$ range. Finally, we solve for T_z given this α_c value. The process is described in Figure 8.3.

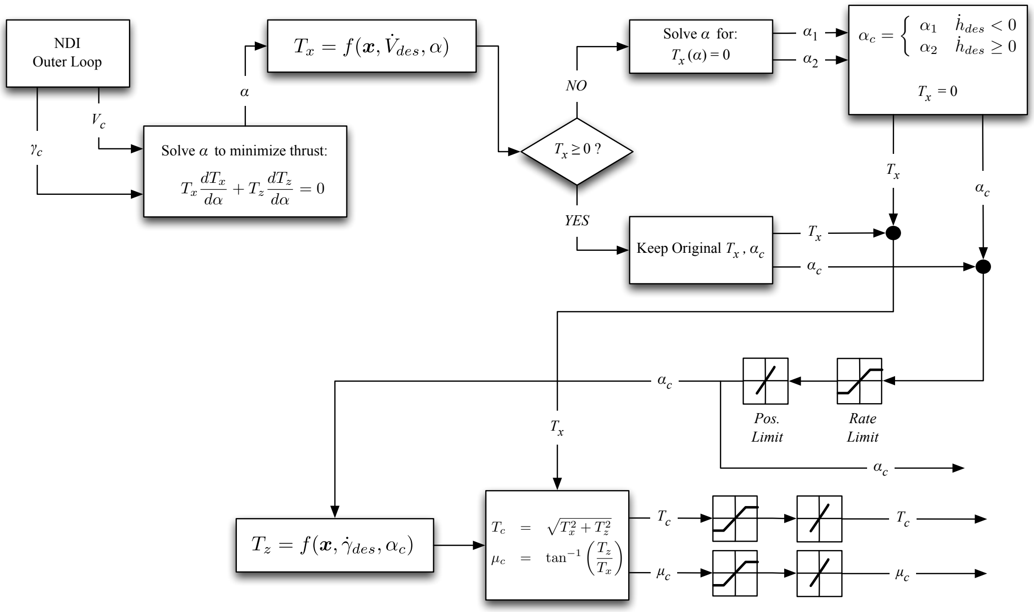

Figure 8.3: NDI Inner Loop Control Law for Minimum-Energy

8.3 Virtual Target and Ascent Cone

The horizontal motion of the airship is influenced both by its wind-relative velocity and the horizontal velocity of the wind. The horizontal distance it flies is the integral over time of the sum of these two velocity components:

$$\begin{aligned}\Delta e &= \int (V\cos\gamma\sin\psi + W_E(h(t)))\,dt \qquad (8.43)\\ &= \Delta e_A + \Delta e_w\\ \Delta n &= \int (V\cos\gamma\cos\psi + W_N(h(t)))\,dt \qquad (8.44)\\ &= \Delta n_A + \Delta n_w\end{aligned}$$

where Δe_A is the eastward distance due to the airship's motion in the wind-relative frame, and Δe_w is the additional eastward distance contributed by the wind. As before, the wind model is assumed to be a function of altitude only. Thus, for a given altitude profile, the wind component of each integrand is determined explicitly as:

$$\Delta e_w = \int W_E(h(t))dt \qquad \Delta n_w = \int W_N(h(t))dt \qquad (8.45)$$

The position of the target station for the ascent trajectory is initially defined in an Earth-fixed (inertial) frame, (e_T, n_T). As the airship ascends over an altitude profile of $h(t)$, it moves horizontally with the wind through Δe_w and Δn_w in the east and north directions, respectively. To reach the horizontal components of the target, we have the constraints:

$$\begin{aligned}\Delta e_A + \Delta e_w &= e_T \qquad (8.46)\\ \Delta n_A + \Delta n_w &= n_T\end{aligned}$$

Now, subtract the wind component from both sides to isolate the wind-relative components of the airship motion:

$$\begin{aligned}\Delta e_A &= \int V\cos\gamma\sin\psi = e_T - \Delta e_w \qquad (8.47)\\ \Delta n_A &= \int V\cos\gamma\cos\psi = n_T - \Delta n_w\end{aligned}$$

This defines a new target, $(e_T - \Delta e_w, n_T - \Delta n_w)$ to be reached in the wind-relative frame. This is hereafter referred to as the *virtual target*.

The diagram shown in Figure 8.4 illustrates the idea of the virtual target with a pure eastward wind profile. The inertial target is far to the east. As the airship ascends, the wind will carry it to the east by $\Delta e_w > 0$, towards the target. Therefore, the actual distance that the airship must fly in the wind-relative frame is shortened.

Figure 8.4: Inertial Target and Virtual Target with East Wind

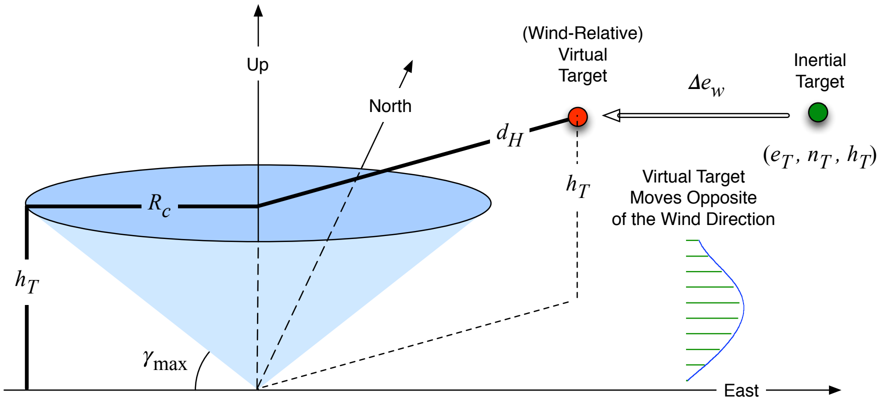

The total horizontal distance flown in the wind-relative frame is:

$$d_H = \sqrt{(e_T - \Delta e_W)^2 + (n_T - \Delta n_W)^2} \tag{8.48}$$

Note that if d_H is very small, the airship would have to ascend nearly vertically in the wind-relative frame. However, recall that we impose a maximum flight path angle, $\gamma_{\max}$. Therefore, the minimum horizontal distance that could be flown over a straight ascent is:

$$R_c = h_T / \tan \gamma_{\max} \tag{8.49}$$

The blue area shown in Figure 8.4 is referred to as the *ascent cone*. It has radius R_c at altitude h_T, according to Eq. (8.49). The virtual target is inside the ascent cone if the wind-relative horizontal distance d_H is less than R_c. When this condition occurs, the airship must fly a curved path in the wind-relative frame. It could not fly a straight path to the virtual target, as this would require the flight path angle to exceed $\gamma_{\max}$. This is equivalent to the need for roads to wind up a mountain in order to keep the grade sufficiently low.

The location of the virtual target with respect to the ascent cone is a distinguishing feature of the optimal ascent trajectories. In the subsections that follow, strategies for both minimum-time and minimum-energy ascent plans are developed. In both cases, the virtual target location is used to determine the appropriate structure of the optimal solution.

8.4 Minimum-Time Ascent

Analysis of optimal solutions indicates a common structure for the minimum time ascent trajectory. The airship always ascends at its maximum rate of climb, subject to constraints on flight path angle, thrust and power. While all minimum-time flights share this trait, they also exhibit some distinguishing characteristics. In general, two different structures of minimum-time ascent paths are observed. In some cases, there is a maximum velocity cruise phase at a certain altitude. This includes both situations where the airship flies with and against the wind. In other cases, the airship consistently climbs at the maximum flight path angle, but winds horizontally in order to intercept the target.

As alluded to previously, the difference between these two structures can be explained by the location of the virtual target with respect to the ascent cone. If the virtual target is inside the ascent cone, the optimal solution is simply to fly at the maximum climb rate, but a turn must be executed in order to intercept the target. Otherwise, if it is outside of the ascent cone, then the optimal structure of the ascent is to climb, cruise at some altitude, and then ascend (or descend) to the station. Each of these two cases is discussed in detail in the sections that follow. First, the ascent profile for maximum rate of climb is presented.

1 Maximum Climb-Rate Ascent

The ideal altitude profile during minimum time ascent can be computed by integrating $\dot{h} = V \sin\gamma$ at maximum thrust and power, and at constant flight path angle, $\gamma_{\max}$. This gives the maximum possible climb rate. Refer to Eq. (8.12) and Eq. (8.13) for $\dot{V}$ and $\dot{\gamma}$ expressions. Setting $\mu = \alpha = 0$, and neglecting the small wind rate term, it can be seen that $\dot{\gamma} = 0$. It is therefore safe to approximate a constant flight path angle of $\gamma_{\max}$ during the ascent. This leaves the altitude profile dependent on the airspeed velocity alone. When integrating $\dot{V}$ we must first note that the thrust is bounded by two constraints:

$$\begin{aligned} T &\leq T_{\max} \\ T &\leq \frac{P_{\max}}{V} \end{aligned}$$

This is due to the fact that the power is bounded by $TV = P \leq P_{\max}$.

By setting $\dot{V} =$ and ignoring the wind rate term, we can approximate the maximum velocity as a function of altitude. By setting Eq. (8.12) to 0 and using $\mu = \alpha = \dot{W}_x = 0$, and $\dot{h} = V \sin\gamma_{\max}$, we obtain the expression:

$$T = \frac{1}{2}\rho(h)U_H^{2/3}C_{D0}V(h)^2 + U_H\frac{\partial\rho(h)}{\partial h}V(h)^2\sin\gamma_{\max} \tag{8.50}$$

Considering the two bounds on thrust, this leads to two possible solutions for $V(h)$. The first solution is applicable when thrust is saturated at $T = T_{\max}$:

$$V_{\max,1}(h) = \left(\frac{2T_{\max}}{\rho(h)U_H^{2/3}C_{D0} + 2U_H\partial\rho(h)\partial h\sin\gamma_{\max}}\right)^{1/2} \tag{8.51}$$

The second is applicable when power is saturated. In this case, the thrust must be lowered so that $T = P_{\max}/V \leq T_{\max}$.

$$V_{\max,2}(h) = \left(\frac{2P_{\max}}{\rho(h)U_H^{2/3}C_{D0} + 2U_H\partial\rho(h)\partial h\sin\gamma_{\max}}\right)^{1/3} \tag{8.52}$$

The analytic solution compares well with the numerical integration. The plot in Figure 8.5 shows a comparison. For the numerical integration, the initial velocity and altitude are set to zero, and the flight path angle is set to $\gamma_{\max} = 30$ deg. The numerical integration reaches maximum velocity at about 2.5 km. After this point, the largest percent error is 3.5%.

Figure 8.5: Comparison of Analytic Expression of Maximum Velocity to Numerical Integration

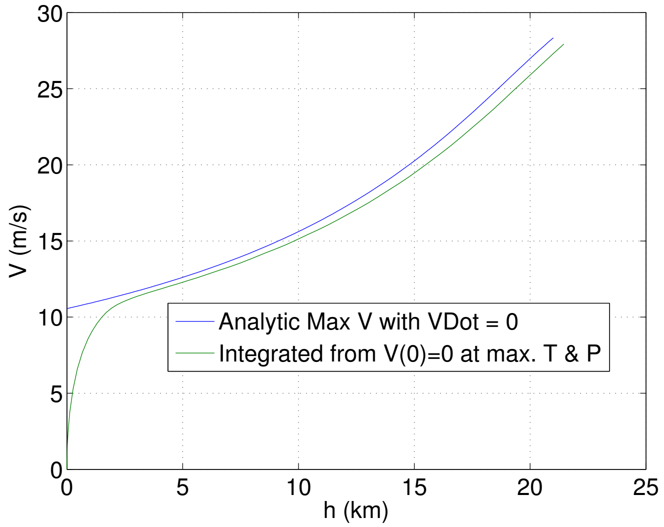

2 Determining the Virtual Target Location

The virtual target location is found by subtracting the cumulative wind drift components from the inertial target. Refer back to Figure 8.4 for an illustration of the inertial and virtual targets.

$$e_{VT} = e_T - \Delta e_W \tag{8.53}$$

$$n_{VT} = n_T - \Delta n_W \tag{8.54}$$

The method for computing the east and north drift components is the same. Therefore we just use the east component as the example in the following equations.

As the airship ascends in the wind-relative frame, the Eastward and Northward wind speeds change. The integration of the wind in each direction over time determines the total amount of drift due to the wind.

$$\Delta e_W = \int_{t_0}^{t_F} W_E(t)dt \tag{8.55}$$

Our model for the wind is a function of altitude, however, and so we must introduce a change of variable. The general formula for integration with a substitution of variable from t to x is:

$$\int_{g(a)}^{g(b)} f(t)dt = \int_a^b f(g(x))g'(x)dx \tag{8.56}$$

where $t = g(x)$. In our problem, we wish to change the integration variable from time t to altitude h. The original function to integrate is $f(t) = W_E(t)$ and the time is expressed as a function of altitude, $t = g(h)$. Therefore, we have:

$$\int_{t_0}^{t_F} W_E(t)dt = \int_{h_0}^{h_F} W_E(g(h))g'(h)dh \tag{8.57}$$

In order to find the functional form for $t = g(h)$, we begin with the equation for the altitude rate:

$$\frac{dh}{d\tau} = V(h)\sin\gamma \tag{8.58}$$

In this derivation we assume that γ is constant, which is true for each segment of the assumed optimal solution structure used in planning minimum-time flights. Rearranging Eq. 8.58 to isolate dh and $d\tau$ on each side, we have:

$$\left(\frac{1}{\sin\gamma}\right)\frac{dh}{V(h)} = d\tau \tag{8.59}$$

Integrating from t_0 to time t, we have:

$$t - t_0 = \int_{t_0}^{t} d\tau = \frac{1}{\sin\gamma}\int_{h_0}^{h_F}\frac{dh}{V(h)} \tag{8.60}$$

For a fixed γ and a known velocity profile, this gives the expected time to climb.

The resulting expression for the cumulative wind drift is:

$$\Delta e_W = \int_{t_0}^{t_F} W_E(t)dt = \frac{1}{\sin\gamma}\int_{h_0}^{h_F}\frac{W_E(h)}{V(h)}dh \tag{8.61}$$

For the minimum-time profile, we use $\gamma = \gamma_{\max}$ and a maximum velocity profile. The maximum velocity formula of Eqs. 8.51 and 8.52 can be used to give a purely analytic expression that can be integrated to give a closed-form solution. A further simplifying step would be to compute a polynomial fit in h for $1/V_{\max}(h)$. Multiplied with the polynomial of $W_E(h)$, this would simply give a higher order polynomial whose integral can be found easily. Implementing this latter approach enables the cumulative wind drift to be evaluated with minimal computational effort. This is particularly important if the evaluation must be done repeatedly in an optimization.

With Δe_W and Δn_W computed, the horizontal distance to the virtual target d_H can be computed with Eq. (8.48), and the ascent cone radius R_T is found from Eq. (8.48). If $d_H \leq R_c$, this then the virtual target is inside the ascent cone; otherwise it lies outside. The optimal solution for each case is described in the sections below.

3 Virtual Target Inside the Ascent Cone, $d_H \leq R_c$

We first consider the case where the virtual target is inside the ascent cone. An example illustration is provided in Figure 8.6. The desired longitudinal motion to fly at maximum flight path angle, and at maximum thrust and power, until the target altitude is reached. Using this altitude profile, the integral effect of the wind can be computed to determine the virtual target location. The airship must then vary the heading such that it intercepts the virtual target at the end of the ascent.

There are in fact an infinite number of ways to vary the heading. As the objective here is to minimize time of flight, the most direct approach is appropriate. One simple and direct method is to fly at a constant turn rate along a circular arc, as projected in the horizontal plane. Since the airship flies at maximum flight path angle, the horizontal distance flown is equal to the ascent cone radius, R_c. Therefore, the virtual target is intercepted if the arc length s (along the circle to the virtual target) is equal to the ascent cone radius R_c.

An illustration of the turning radius geometry is shown in Figure 8.7. The direction

Figure 8.6: Minimum-Time Path for Virtual Target Inside the Ascent Cone

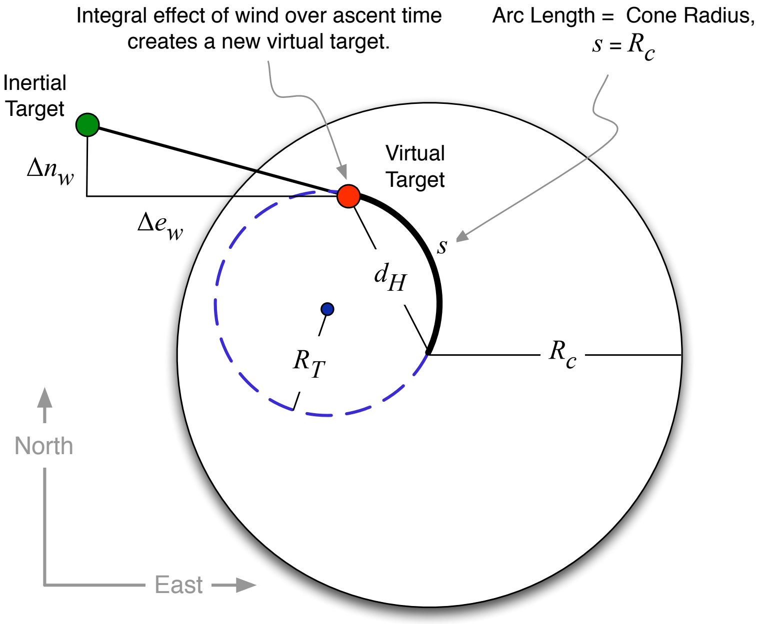

of motion at the starting point and end point (virtual target) is shown with arrows. The vehicle has an initial heading of ψ_0 and turns at a constant $\mathrm{d}\psi/ds$ rate along the circular arc, ending at heading ψ_F.

The angular length of the arc flown is:

$$\phi_T = \frac{s}{R_T} \tag{8.62}$$

Now consider the two symmetric triangles formed inside the circle. The sine of $\phi_T/2$ is equal to the ratio of the opposite side ($d_H/2$) to the hypotenuse (R_T). Using this with Eq. (8.62) leads to the equation:

$$\sin\left(\frac{s}{2R_T}\right) - \frac{d_H}{2R_T} = 0 \tag{8.63}$$

The turning radius is found by solving the above equation for R_T, with s and d_H given. There is no analytic solution but it can be easily solved numerically. For example, using the Newton-Rhapson method with s as the initial guess typically converges in 5 or fewer iterations.

Figure 8.7: Constant Turning Radius for Virtual Target Inside the Ascent Cone

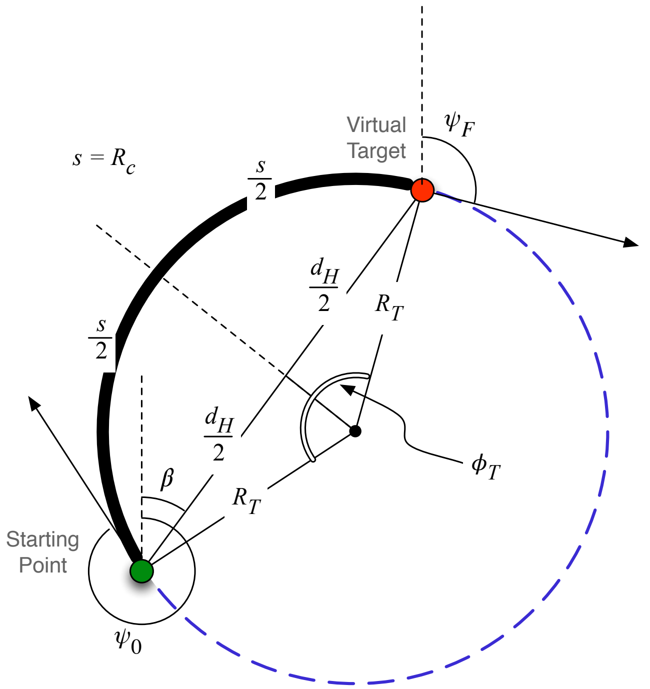

Also, note that for the limiting case of $d_H = s$, the solution is $R_T = \infty$, which corresponds to a straight line. This is consistent with the definition of the ascent cone.

The heading rate is derived by first applying the chain rule to get:

$$\frac{d\psi}{ds} = \frac{d\psi}{ds}\frac{ds}{dt} \tag{8.64}$$

The first term $d\psi/ds$ is the rate of change of heading with respect to the arc length. Because a circular arc is flown, this is a constant equal to the inverse of the turning radius, $1/R_T$. The second term ds/dt is the horizontal velocity, which is $V \cos\gamma$. Therefore, the heading angle history can be expressed as:

$$\psi(t) = \psi_0 + \frac{1}{R_T}\int_0^t V(\tau)\cos\gamma_{\max} d\tau \tag{8.65}$$

where the initial heading is determined from the geometry to be:

$$\psi_0 = \begin{cases} \beta \pm \phi/2 & s \leq \pi R_T \\ \beta \pm \phi/2 + \pi & s > \pi R_T \end{cases} \tag{8.66}$$

and β is the angle from the starting point to the target, measured from north.

$$\tan\beta = \frac{\Delta e}{\Delta n} \tag{8.67}$$

The sign on the $(\phi/2)$ term in each case is arbitrary. This is due to the fact that the diagram could have been drawn differently, reversing it about the d_H line (from starting point to virtual target). In that case the arc length would have been the same but the initial heading would be towards the east rather than the northwest.

Two examples of the turn radius calculation are shown below. In both cases, the ascent cone radius is $R_c = 10$ km. In the plot on the left, the virtual target is at coordinates $(1, 2)$ km in the East-North plane. The solution to Eq. (8.63) yields $R_T = 1.97$ km. Computing the turn angle with Eq. (8.62) gives $\phi = 5.07$ rad. In the right-hand side plot, the virtual target is moved to coordinates $(5, 6)$ km, and the turn radius is $R_T = 4.2$ km with a turn angle of $\phi = 2.37$ rad.

Figure 8.8: Constant Turn Radius Examples

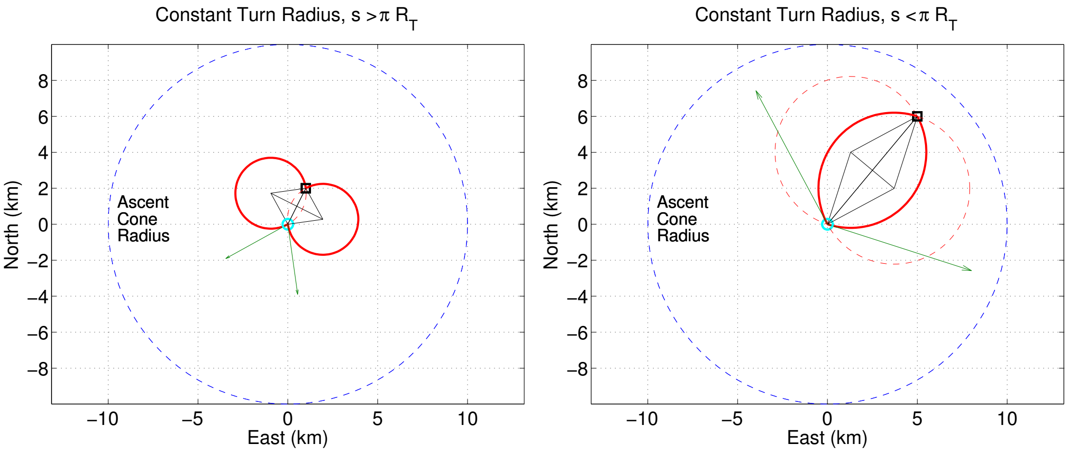

Example of Minimum-Time Plan with Virtual Target Inside the Ascent Cone

Here, an example of a minimum-time ascent plan is presented where the virtual target is inside the ascent cone. We use one of the cases from Scenario 4, where the target station is 10 km east of the launch site, and the target altitude is again 21 km. The optimal solution for this scenario showed to exhibit a winding path during the ascent, indicating that the virtual target is inside the ascent cone.

First, the longitudinal motion is predicted by integrating the airship equations of motion at maximum thrust and power constraints. The flight path angle is controlled at $\gamma_{\max}$ by adjusting the thrust angle using NDI control. The angle of attack is held constant to minimize drag, and thrust is set to the smaller of $T_{\max}$ or $P_{\max}/V$. The resulting time histories are shown in Figure 8.9. The ascent time is 48 minutes.

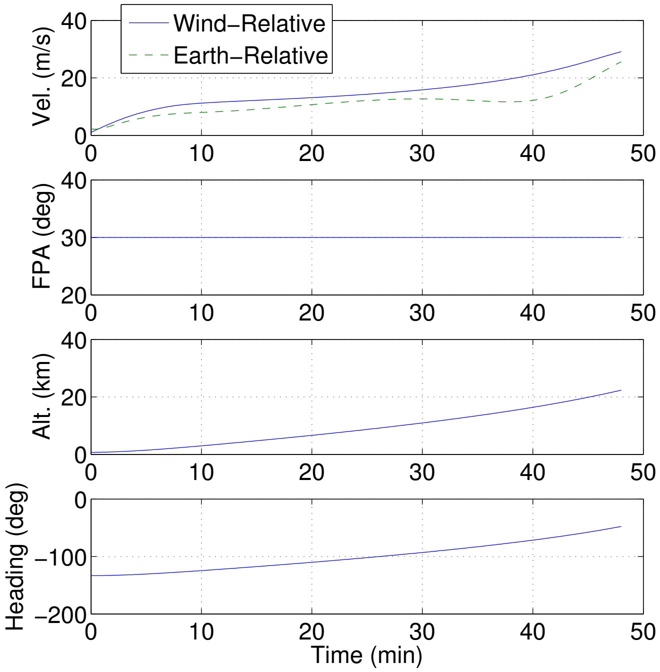

Figure 8.9: Longitudinal Time Histories of Minimum-Time Ascent

Note that the airspeed velocity exceeds the initial velocity for the entire flight. This is because the airship must fly into the wind as it ascends, reducing the inertial velocity in the horizontal plane so that it does not drift past the target. The heading changes gradually over the flight from -133 deg to -47 deg. It therefore begins by flying southwest, slowly turns north, and ends the flight with a northwest heading. This can be seen in Figure 8.10, which shows the wind-relative path of the airship in the east-north plane.

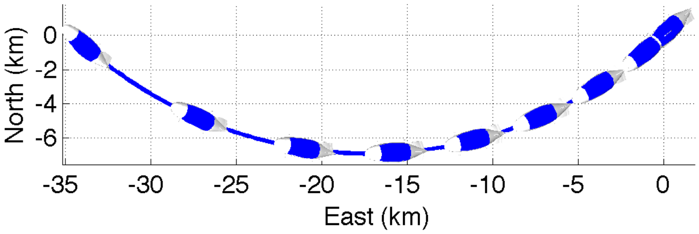

Figure 8.10: Wind-Relative Ascent Path

The inertial, or Earth-relative, path of the airship is plotted in Figure 8.11. The winding nature of the ascent is evident in the 3D plot on the left. This also illustrates that the inertial path successfully reaches the target station. The plot on the right shows the inertial path in the horizontal plane. Although it flies towards the west for the duration of the flight, it is carried east by the wind.

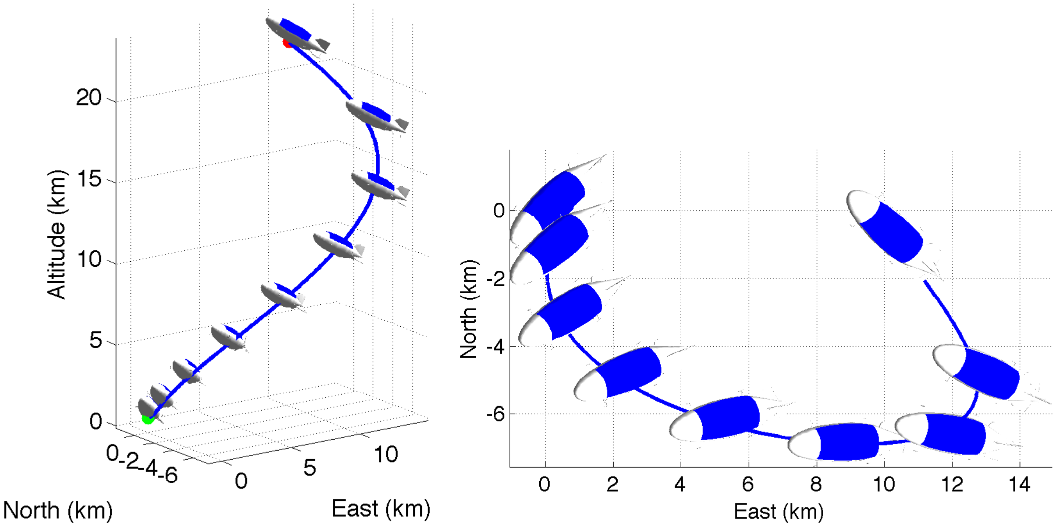

Figure 8.11: Earth-Relative Ascent Path

4 Virtual Target Outside the Ascent Cone, $d_H > R_c$

In this case, if the airship were to fly at the maximum flight path angle, it would reach the target altitude before it reaches the horizontal target (east,north) coordinates.

Therefore, it must fly for some portion of the trajectory at a lower flight path angle. This is evidenced in the optimal trajectories presented in Chapter 6. For example, Figure 6.1 shows the minimum-time ascent from 250 km downrange flying for a significant portion at 14 km, to make use of the peak east winds at that altitude.

The general structure of optimal solution for this case is as follows:

1. Ascend at the maximum climb-rate to cruise altitude h_C
    - Heading: ψ_A
    - Velocity: $V_{\max}(h)$
    - Flight path angle: $\gamma_{\max}$
2. Fly at cruise altitude h_C for time duration Δt_C
    - Heading: ψ_C
    - Velocity: $V_{\max}(h_C)$
    - Flight path angle: 0
3. Ascend (or descend) at the maximum climb-rate to target altitude h_T
    - Heading: ψ_A
    - Velocity: $V_{\max}(h)$
    - Flight path angle: $\pm\gamma_{\max}$

The approach taken here is to build a trajectory according to this structure in order to emulate the optimal minimum-time ascent solution. The set of parameters describing the trajectory include: ascent heading ψ_A, the cruise altitude h_C, cruise heading ψ_C and cruise time Δt_C. Thus, the size of the problem is reduced to just a few decision variables. The full problem formulation with objective function and constraints will be presented below.

First, the overall geometry is described in Figure 8.12. Here, the ascent heading has been intentionally drawn as $\psi_A = 0$ to simplify the diagram for visual clarity. As shown, the airship first ascends at the maximum flight path, with a fixed ascent heading. It then flies at a constant altitude at some other coast heading, and finally ascends to the target altitude at the ascent heading. All segments are flown at maximum airspeed, with thrust and/or power at their limit.

Figure 8.12: Minimum-Time Path for Virtual Target Inside the Ascent Cone

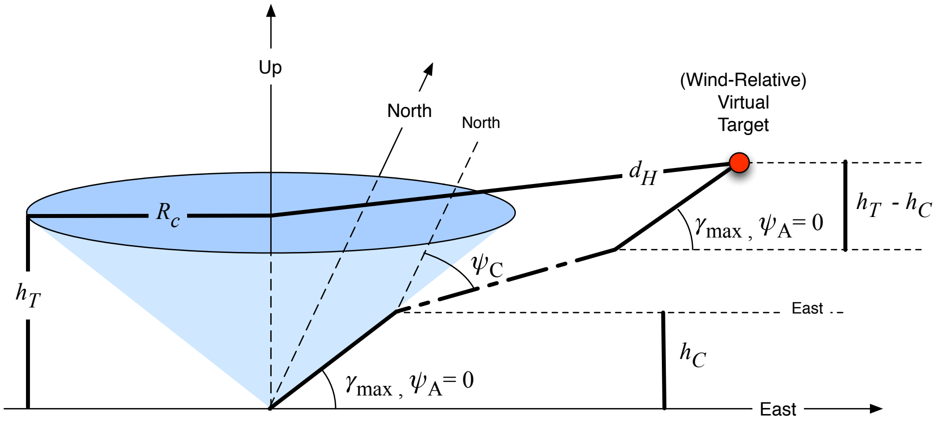

The total time to reach the station is approximated as the ascent time plus the horizontal cruise time:

$$t_F \approx \Delta t_A + \Delta t_C \tag{8.68}$$

The duration of the ascent phase is already minimized, as it is flown at the maximum rate of climb. Therefore, the task of minimizing the total ascent time for this trajectory reduces to a minimization of the cruise time.

To develop an expression for the cruise time, first consider the details of the ascent structure, as illustrated in Figure 8.13. The airship starts at the center of the ascent cone with radius R_c. It ascends at heading ψ_A to reach coordinates (e_{A0}, n_{A0}) at the end of the ascent phase. This position is marked with a bold blue circle on the ascent cone perimeter. During this time, the wind velocity produces a cumulative drift of Δe_w

and Δn_w in the east and north directions, respectively, moving the virtual target to (e_{VT0}, n_{VT0}).

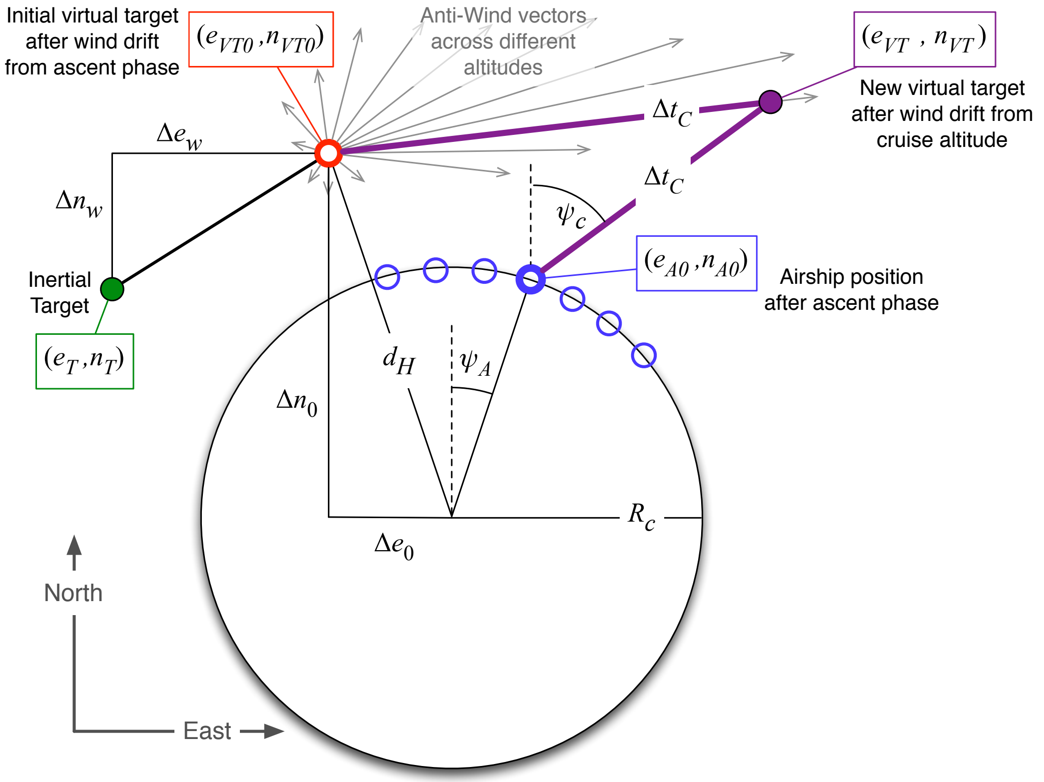

Figure 8.13: Minimum-Time Path for Virtual Target Outside the Ascent Cone

Several wind vectors are shown, representing the different magnitude and direction the of the wind across altitude. The virtual target is moved to its final location along the opposite direction of the wind vector at the selected cruise altitude. The virtual target location is defined as:

$$e_{VT} = e_T - \Delta e_w - W_E(h_C)\Delta t_C \tag{8.69}$$

$$n_{VT} = n_T - \Delta n_w - W_N(h_C)\Delta t_C \tag{8.70}$$

The position of the airship at the end of the ascent phase depends on the ascent cone radius, which is fixed for a given problem formulation, and the ascent heading, which may be varied. The coordinates are:

$$e_{A0} = R_c \sin\psi_A \tag{8.71}$$

$$n_{A0} = R_c \cos\psi_A \tag{8.72}$$

In order to reach the virtual target, the airship must fly at the required heading ψ_C. At the given cruise altitude, it has maximum velocity $V_{\max}(h_C)$. Therefore, the equation for the east position at the end of the cruise phase is:

$$e_{A0} + V_{\max}(h_C)\sin\psi_C \Delta t_C = e_T - \Delta e_w - W_E(h_C)\Delta t_C \tag{8.73}$$

Rearranging to solve for Δt_C gives:

$$\Delta t_C = \frac{e_T - \Delta e_w - R_c \sin\psi_A}{V_{\max}(h_C)\sin\psi_C + W_E(h_C)} \tag{8.74}$$

Using the north component produces a similar equation:

$$\Delta t_C = \frac{n_T - \Delta n_w - R_c \cos\psi_A}{V_{\max}(h_C)\cos\psi_C + W_N(h_C)} \tag{8.75}$$

Setting Eq. (8.74) and Eq. (8.75) equal enables ψ_C to be isolated in a function with the inertial target coordinates, the wind drift components, the wind velocities and maximum airspeed velocity at h_C, and the ascent heading ψ_A.

$$\begin{aligned}(V_{\max}(h_C)\cos\psi_C + W_N(h_C))\,(e_T - \Delta e_w - R_c \sin\psi_A) &= \\ (V_{\max}(h_C)\sin\psi_C + W_E(h_C))\,(n_T - \Delta n_w - R_c \cos\psi_A)\end{aligned} \tag{8.76}$$

This can be solved for $\sin\psi_C$ by isolating its cosine and sine terms, setting $\sin\psi_C = \pm\sqrt{1-\cos^2\psi_C}$, and squaring both sides of the equation. This leads to a quadratic expression in $\sin\psi_C$ which is readily solved.

Thus far, we have developed an equation for the cruise time Δt_C as a function of given parameters (e_{VT0}, R_c), and the variables ψ_A, h_C, and ψ_C. We have further found that ψ_C can be solved explicitly as a function of h_C, ψ_A. We are now in a position to minimize the cruise time over the variables h_C, ψ_A. First, however, we must consider the constraints on the inertial heading during the cruise phase.

One unique characteristic of airships that is not found in traditional aircraft is that they often fly at an airspeed that is slower than the ambient wind. As a simple example, consider an airship flying with a wind-relative speed of $V = 10$ m/s towards the west, but the wind is blowing east at $W_E = 25$ m/s. The inertial motion of the vehicle would of course be towards the east at $V_I = 15$ m/s. In this case, it would not be possible for the airship attain an inertial velocity towards the west, due to the overpowering influence of the wind. This potential limitation on inertial heading must be considered when selecting a cruse altitude.

When the cruise altitude is selected, it defines the wind magnitude $W = \sqrt{W_E^2(h_C) + W_N^2(h_C)}$ and direction $\psi_W = \tan^{-1}(W_E/W_N)$, as well as the airspeed velocity $V = V_{\max}(h_C)$. The diagram in Figure 8.14 illustrates the inertial heading constraints for the case when the wind magnitude is greater than the airspeed, $W > V$.

The inertial velocity is shown as the vector sum of the wind velocity and the airship's wind-relative velocity. A circle of radius V is drawn at the tip of the wind vector, indicating that the vehicle can fly in any wind-relative direction. However, since the wind velocity magnitude, which is not controllable, is greater than the ship's airspeed, this limits the achievable heading range for the inertial velocity. The attainable range of inertial velocity directions is marked with blue lines. As the geometry shows, the limits are:

$$\psi_{I,\min} = \psi_W - \Delta\theta \tag{8.77}$$

$$\psi_{I,\max} = \psi_W + \Delta\theta \tag{8.78}$$

where the angle $\Delta\theta$ is found to be

$$\Delta\theta = \sin^{-1}\left(\frac{V}{W}\right)$$

Consider again the geometry of the cruise phase in Figure 8.13. The east distance to the target is $e_{VT0} - e_{A0}$, and the north distance is $n_{VT0} - n_{A0}$. The inertial heading

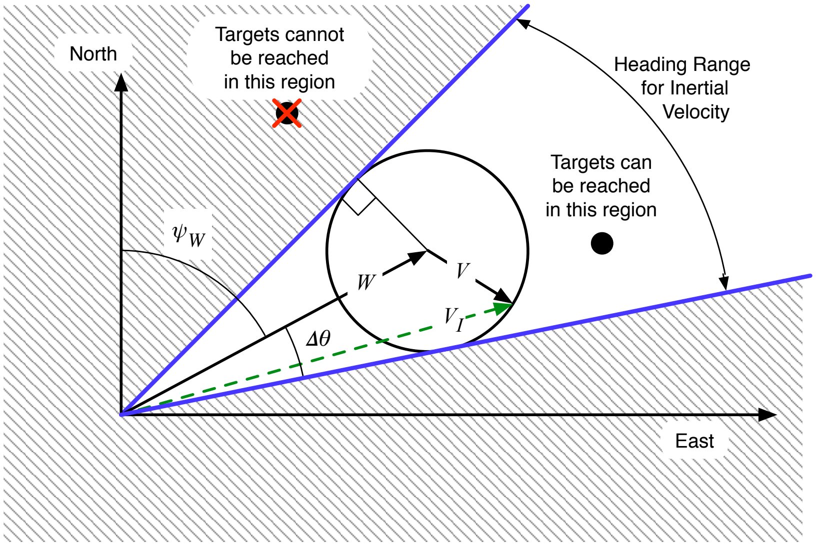

Figure 8.14: Heading Constraint for Minimum-Time Ascent

angle is therefore:

$$\psi_I = \tan^{-1}\left(\frac{e_{VT0} - e_{A0}}{n_{VT0} - n_{A0}}\right)$$

If it is the case that $W > V$, then in order for the airship to be capable of reaching the target, this heading angle must lie within the inertial heading limits described above: $\psi_{I,\min} \leq \psi_I \leq \psi_{I,\max}$. Expanding each term, the constraints are written as a function of the given parameters and variables h_C, ψ_A as follows:

$$\tan^{-1}\left(\frac{e_{VT0} - R_c \sin\psi_A}{n_{VT0} - n_{A0}}\right) \geq \tan^{-1}\left(\frac{W_E(h_C)}{W_N(h_C)}\right) - \sin^{-1}\left(\frac{V_{\max}(h_C)}{\sqrt{W_E^2(h_C) + W_N^2(h_C)}}\right) \tag{8.79}$$

$$\tan^{-1}\left(\frac{e_{VT0} - R_c \sin\psi_A}{n_{VT0} - n_{A0}}\right) \leq \tan^{-1}\left(\frac{W_E(h_C)}{W_N(h_C)}\right) + \sin^{-1}\left(\frac{V_{\max}(h_C)}{\sqrt{W_E^2(h_C) + W_N^2(h_C)}}\right) \tag{8.80}$$

With the cost function and the constraints now fully developed, we may write the complete problem formulation. The problem again is to minimize the cruise time through selection of the cruise altitude h_C and ascent heading ψ_A, subject to constraints on the inertial cruise heading. The minimum-time problem formulation is:

Minimum-Time Problem Formulation - Outside Ascent Cone, $d_H > R_c$

$$\begin{array}{ll} \min\limits_{h_C,\psi_A} & \Delta t_C = \dfrac{e_{VT0} - R_c \sin\psi_A}{V_{\max}(h_C)\sin\psi_C + W_E(h_C)} \\ \text{s.t.} & \tan^{-1}\left(\dfrac{e_{VT0} - R_c \sin\psi_A}{n_{VT0} - R_c\cos\psi_A}\right) - \tan^{-1}\left(\dfrac{W_E(h_C)}{W_N(h_C)}\right) - \sin^{-1}\left(\dfrac{V_{\max}(h_C)}{W(h_C)}\right) \leq 0 \\ & -\tan^{-1}\left(\dfrac{e_{VT0} - R_c \sin\psi_A}{n_{VT0} - R_c\cos\psi_A}\right) + \tan^{-1}\left(\dfrac{W_E(h_C)}{W_N(h_C)}\right) - \sin^{-1}\left(\dfrac{V_{\max}(h_C)}{W(h_C)}\right) \leq 0 \end{array} \tag{8.81}$$

where the cruise heading is solved explicitly according to the equation:

$$V_{\max}(h_C)\Delta e(\psi_A)\cos\psi_C - V_{\max}(h_C)\Delta n(\psi_A)\sin\psi_C + W_N(h_C)\Delta e(\psi_A) - W_E \Delta n(\psi_A) = 0$$

and the following abbreviations have been used:

$$\begin{aligned} W(h_C) &= \sqrt{W_E^2(h_C) + W_N^2(h_C)} \\ \Delta e(\psi_A) &= e_{VT0} - R_c \sin\psi_A \\ \Delta n(\psi_A) &= n_{VT0} - R_c \cos\psi_A \end{aligned}$$

The above problem formulation is a nonlinear program with two variables and two constraints. It is solved using Matlab's `fmincon` program with the sequential quadratic programming method (SQP). This approach computes a quasi-Newton approximation to the Hessian of the Lagrangian through evaluation of the cost and constraint functions.

Whereas the original minimum-time optimization included thousands of variables and constraints, taking tens to hundreds of seconds to reach a solution, this problem is routinely solved in less than 0.25 seconds. [1]

Example of Minimum-Time Plan with Virtual Target Outside the Ascent Cone

Consider the minimum-time ascent of Scenario 2 from Figure 6.1. The same conditions are repeated here and the solution is generated using the above alternative optimization method. In this case, the virtual target is outside the ascent cone, requiring a substantial cruise phase. A comparison of the original SNOPT solution and the new alternative method are shown in Figure 8.15. The two profiles agree closely, with both following a constant altitude cruise segment at about 14 km. The original SNOPT solution predicts a minimum time of 2 hours and 1 minute, compared with the new method's result of 2 hours and 5 minutes.

We now consider another example, where the target station is located 120 km east and 20 km south of the launch site. The same east wind profile is used, and a north wind profile is added that varies between -4 and +4 m/s. The total flight time is computed across a range of possible cruise altitudes and ascent headings, and the result is plotted with a color-map surface contour in Figure 8.16. The dark red region in the lower left corner is infeasible, as the combination of ascent heading and cruise altitude here would prevent the airship from overcoming the wind velocity. The color-map legend is shown in units of minutes. This shows that, even with a poor initial guess, the optimization method converges to the verified optimal solution.

---

[1] Mac PowerBook, Mac OS 10.7.5, 2 GHz Intel Core i7 processor, 4 GB RAM, Matlab R2013A

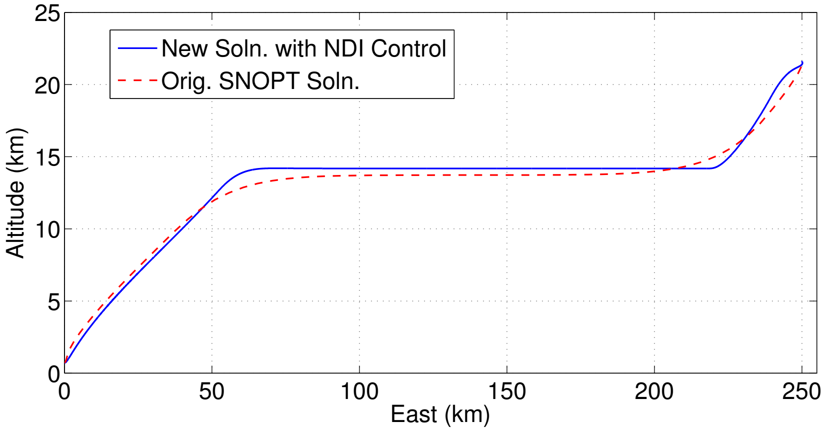

Figure 8.15: Scenario 2, Alternative Minimum-Time Ascent Solution Tracked with NDI Control, Comparison to Original SNOPT Solution

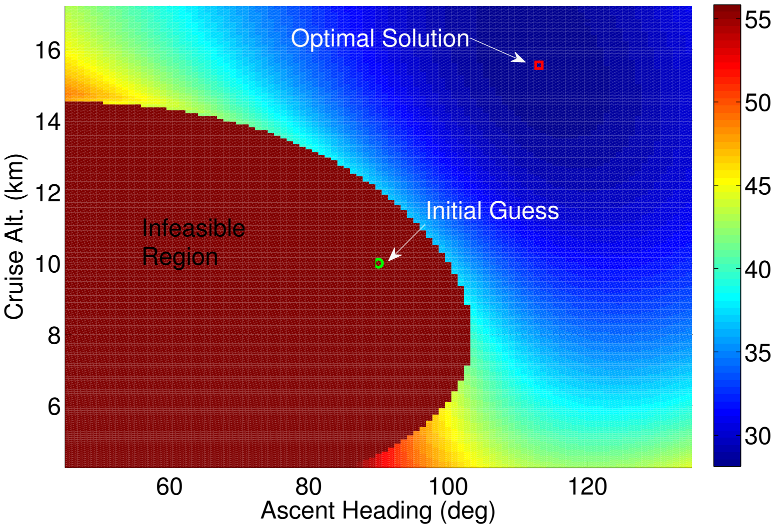

Figure 8.16: Evaluation of Flight Time Across Cruise Altitude and Ascent Heading

8.5 Minimum-Energy Ascent

In this section we develop new problem formulations involving trajectory models that emulate the structure of known minimum-energy solutions, with the immediate goal of reducing the computation time required to generate a solution. The ultimate objective is to apply this technique to rapidly develop near minimum-energy ascent plans for onboard implementation. A significant decrease in the planning computation time is achieved by greatly reducing the number of decision variables, and quickly generating an initial guess that is close to being feasible.

The minimum-energy solutions found from prior numerical optimization work indicate two different basic structures of the optimal solution. One type of solution involves a steady longitudinal ascent, at roughly constant airspeed and flight path angle, while the wind-relative heading varies. The second type of solution involves a steady wind-relative heading with three longitudinal segments: 1) a steepest ascent at roughly constant airspeed to the maximum operational altitude, 2) a constant velocity, level flight towards the station, and 3) a short descent to the station altitude.

The former structure, where the heading varies over time, is termed a *winding ascent*. The latter, where the heading is nearly constant, is termed a *direct ascent*. The remainder of this section discusses the modeling of these trajectory structures, and presents optimization methods to compute minimum energy trajectories that intercept the target station.

The procedure for computing the minimum-energy ascent plan is summarized in Figure 8.17. The first step is to identify which of the ascent types, *direct* or *winding*, should be used. To do this, we begin by computing a minimum energy solution for the simplest possible ascent, which is a straight line to the virtual target at constant velocity. If necessary, an additional cruise segment at constant altitude, constant velocity, may also be used. This initial trajectory structure is termed the *simple ascent*. If a horizontal cruise segment is used in the simple ascent, then we go on to compute a direct ascent plan. Otherwise, if no horizontal segment is used, we compute a winding ascent plan.

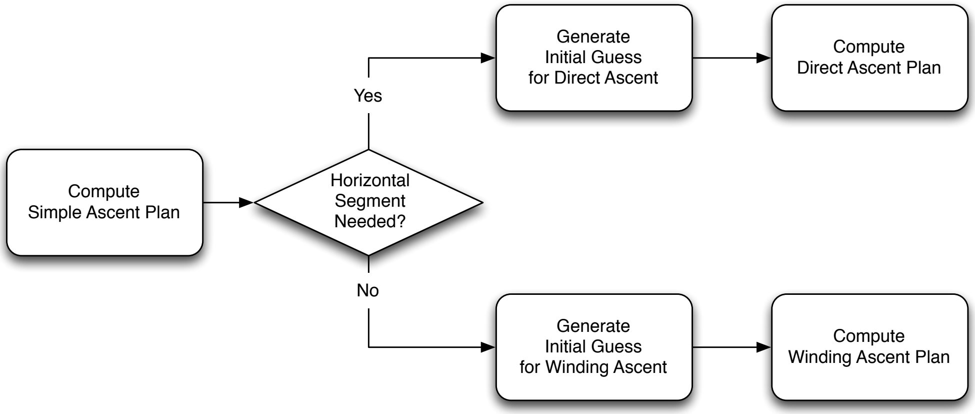

Figure 8.17: Procedure for Developing Minimum-Energy Ascent Plan

Each of the aforementioned methods is presented in the sections that follow. First, however, it is necessary to establish the fundamental components of the trajectory model that are used to develop each ascent profile.

Longitudinal Motion with Piecewise Linear Segments of V, γ

Let us now model the trajectory of the airship as a series of segments where its airspeed and flight path angle change linearly with time. Thus, over a time increment $0 \leq t \leq \Delta T_k$ from point k to $k+1$ in the segment, we have:

$$V(t) = V_k + at \tag{8.82}$$

$$\gamma(t) = \gamma_k + bt \tag{8.83}$$

where a and b give the constant rate of change in velocity and flight path angle, respectively, over the segment. These are defined as follows:

$$a = \left(V_{k+1} - V_k\right)/\Delta T_k \tag{8.84}$$

$$b = \left(\gamma_{k+1} - \gamma_k\right)/\Delta T_k \tag{8.85}$$

Using these expressions, we may integrate the altitude rate to find an analytic expression for the altitude over time.

$$\begin{aligned} h(t) &= \int_0^t V(\tau)\sin\gamma(\tau)d\tau && (8.86)\\ &= \int_0^t (V_k + a\tau)\sin(\gamma_k + b\tau)\,d\tau && (8.87)\end{aligned}$$

The solution to this integral requires the method of integration by parts. The general solution has a singularity at $b = 0$. Therefore, the solution for the $b = 0$ case is found separately by simply integrating the linear velocity expression with a constant flight path angle.

$$h(t)-h(0) = \begin{cases} \frac{1}{2}\sin\gamma_k t\,(at + 2V_k) & b = 0\\ V_k/b\,(\cos\gamma_k - \cos\gamma(t)) + a/b^2\,(\sin\gamma(t) - \sin\gamma_k - bt\cos\gamma(t)) & b \neq 0 \end{cases} \tag{8.88}$$

For notational convenience, we can compactly write this altitude expression as:

$$\Delta h_{k+1}(t) = H_{PL}(V_k, \gamma_k, V_{k+1}, \gamma_{k+1}, t)$$

where the PL subscript refers to the piecewise linear dependence on V, γ. This describes the altitude variation over time from $t = 0$ at k to $t = \Delta t_{k+1}$.

Now consider the horizontal distance travelled $s(t)$, which is the integral of the horizontal velocity:

$$\begin{aligned} s(t) &= \int_0^t V(\tau)\cos\gamma(\tau)d\tau && (8.89)\\ &= \int_0^t (V_k + a\tau)\cos(\gamma_k + b\tau)\,d\tau && (8.90)\end{aligned}$$

The solution for $s(t)$ is found in the same fashion as the altitude.

$$s(t)-s(0) = \begin{cases} \frac{1}{2}\cos\gamma_k t\,(at + 2V_k) & b = 0\\ V_k/b\,(\sin\gamma(t) - \sin\gamma_k) + a/b^2\,(\cos\gamma(t) - \cos\gamma_k + bt\sin\gamma(t)) & b \neq 0 \end{cases} \tag{8.91}$$

Once again, for notational convenience, we can compactly write this distance expression as:

$$\Delta s_{k+1}(t) = S_{PL}(V_k, \gamma_k, V_{k+1}, \gamma_{k+1}, t)$$

Just as with the altitude function $H_{PL}()$ above, this describes the horizontal distance variation over time from $t = 0$ at k to $t = \Delta t_{k+1}$.

Lateral Motion with Piecewise Constant Segments of Turning Radius R

Lateral motion is modeled with each segment following a constant turning radius. The heading rate is proportional to the horizontal velocity and inverse of the turning radius.

$$\dot{\psi} = \frac{V \cos\gamma}{R} \tag{8.92}$$

Noting that $\dot{\psi} = \Delta\psi/\Delta t$ and $\dot{s} = \Delta s \Delta t = V\cos\gamma$, we can multiply both sides of Eq. (8.92) by Δt to give the change in heading at any time over the segment:

$$\psi(t) - \psi(0) = \frac{s(t) - s(0)}{R_k} \tag{8.93}$$

For notational convenience, the heading angle function for the $(k, k+1)$ segment can be written compactly as:

$$\Delta\psi_{k+1}(t) = S_{PL}(V_k, \gamma_k, V_{k+1}, \gamma_{k+1}, t)/R_k$$

where time varies from $t = 0$ at point k to $t = \Delta t_{k+1}$ at point $k+1$.

The change in east position is computed from the following integral:

$$e(t) - e(0) = \int_0^t V(\tau)\cos\gamma(\tau)\sin\psi(\tau)d\tau \tag{8.94}$$

It is convenient to introduce a change of variable so that we may integrate with respect to ψ rather than time. Note that the definition of $d\psi$ is

$$d\psi = \frac{V(\tau)}{R}\cos\gamma(\tau)d\tau \tag{8.95}$$

Substituting this into Eq. (8.94) we have:

$$\begin{aligned} e(t) - e(0) &= R_k \int_{\psi(0)}^{\psi(t)} \sin\psi d\psi && (8.96) \\ &= R_k \left(\cos\psi(0) - \cos\psi(t)\right) && (8.97) \end{aligned}$$

Similarly, the north position is computed from the integral:

$$n(t) - n(0) = \int_0^t V(\tau)\cos\gamma(\tau)\cos\psi(\tau)d\tau \qquad (8.98)$$

Again, substitution is used to express the integral as a function of ψ, giving:

$$\begin{aligned} n(t) - n(0) &= R_k \int_{\psi(0)}^{\psi(t)} \cos\psi d\psi && (8.99) \\ &= R_k \left(\sin\psi(t) - \sin\psi(0)\right) && (8.100) \end{aligned}$$

1 Minimum-Energy Simple Ascent Profile

The cumulative energy is the integral of the applied power over time. With a propeller, the required power is modeled as $P = \eta TV$. In the simple ascent, we assume constant velocity flight. Thus, thrust equals drag and so $P = \eta DV$. Therefore, the energy is expressed as:

$$E = \eta \int_0^t D(h(\tau))V d\tau \qquad (8.101)$$

assuming constant efficiency across altitude, where τ is the integration variable for time. We can introduce a change of variable by noting that $\dot{h} = dh/d\tau$, and instead integrate across altitude. Define the limits of integration as $h = h_0$ at $\tau = 0$ and $h = h_F$ at $\tau = t$. Using the formula for drag, Eq. (8.101) becomes:

$$\begin{aligned} E &= \frac{1}{\dot{h}} \int_{h_0}^{h_F} \frac{1}{2}\rho(h)V^2 SC_D V dh && (8.102) \\ &= \frac{SC_D V^3}{2\dot{h}} \int_{h_0}^{h_F} \rho(h)dh \\ &= \frac{SC_D V^2}{2\sin\gamma}\overline{\rho}(h_0, h_F) && (8.103) \end{aligned}$$

where the notation $\overline{X}(a,b)$ is used to indicate the integration of the polynomial function X from limits a to b.

The simple ascent profile is modeled as a constant velocity and constant flight path angle ascent, as above, with an optional horizontal cruise segment. The full problem formulation for the minimum-energy simple ascent profile is given below. The energy cost includes the energy consumed during both the ascent and the horizontal cruise segment.

Minimum-Energy Problem Formulation - Simple Ascent

$$\begin{aligned}
\min_{V,\gamma,h_C,V_C,\Delta t_C} \quad & E = \frac{1}{2} S C_D \left(\frac{V^2}{2\sin\gamma} \overline{\rho}(h_0, h_F) + \rho(h_C) V_C^3 \Delta t_C \right) \\
\text{s.t.} \quad & \Delta e^2 + \Delta n^2 - \Delta x^2 \leq 0 \\
& \Delta e = e_T - \frac{\overline{W_E}(h_0, h_F)}{V \sin\gamma} - W_E(h_C)\Delta t_C - e_0 \\
& \Delta n = n_T - \frac{\overline{W_N}(h_0, h_F)}{V \sin\gamma} - W_N(h_C)\Delta t_C - n_0 \\
& \Delta x = (h_T - h_0)/\tan\gamma + V_C \Delta t_C
\end{aligned} \tag{8.104}$$

Here, Δx is the total horizontal distance covered during the combined ascent and cruise segment. The inequality constraint $\Delta e^2 + \Delta n^2 - \Delta x^2 \leq 0$ simply forces this distance to exceed the horizontal distance to the virtual target, ensuring that the target is reachable. If it is possible to satisfy this constraint with no cruise segment ($\Delta t_C = 0$), then this approach is favored as it would reduce the total energy.

It is interesting to note that the first energy term is inversely proportional to $\sin\gamma$, indicating that it is best to climb at the maximum flight path angle. This is intuitive, as climbing at a shallower angle would tend to prolong the flight and lead to increased energy usage. This is also consistent with the findings from extensive numerical optimizations.

2 Minimum-Energy Winding Ascent Profile, $\Delta t_C = 0$

The winding ascent profile is used if the simple ascent plan produces a trajectory with no cruise phase, so that $\Delta t_C = 0$. In this case, the general structure of the minimum energy solution is to climb at the maximum flight path angle and vary the heading.

For this ascent profile, the final time is fixed and the trajectory is divided into N segments of equal time. Each segment is modeled with a constant turn radius and a velocity and flight path angle that vary linearly with time, according to the piecewise linear V, γ segments described previously. The inverse of the turning radius is used for the decision variable, rather than the turning radius itself, because this enables the variable to be more tightly bounded. The bounds on the inverse turning radius are therefore $0 \leq 1/R_k \leq 1/R_{\min}$.

The problem formulation is shown below. The decision variables include the velocity, flight path angle, and inverse turn radius for each segment, as well as the initial heading. It therefore includes $3N + 1$ decision variables. Three equality constraints are applied, forcing each coordinate of the final position to equal the corresponding target station coordinate. In addition, inequality constraints are applied to the time-varying altitude to keep it within bounds.

Minimum-Energy Problem Formulation - Winding Ascent

$$\min_{V_k, \gamma_k, 1/R_k, \psi_0} \quad E = \sum_{k=1}^{N_S} \int_{t_k}^{t_{k+1}} T_{Ck}(t) V_k(t) dt \tag{8.105}$$

$$\text{s.t.} \quad e_0 + \sum_{k=1}^{N_S} \left(\Delta e_k + \int_{t_k}^{t_k+1} W_E(h_k(t)) dt \right) = e_T$$

$$n_0 + \sum_{k=1}^{N_S} \left(\Delta n_k + \int_{t_k}^{t_k+1} W_N(h_k(t)) dt \right) = n_T$$

$$h_0 + \sum_{k=1}^{N_S} \Delta h_k = h_T$$

$$h_k(t) - h_{\max} \leq 0$$

$$h_0 - h_k(t) \leq 0$$

where the piecewise linear segments for velocity and flight path angle are:

$$V_k(t) = V_{k-1} + (V_k - V_{k-1}) \frac{t - t_{k-1}}{t_k - t_{k-1}} \tag{8.106}$$

$$\gamma_k(t) = \gamma_{k-1} + (\gamma_k - \gamma_{k-1}) \frac{t - t_{k-1}}{t_k - t_{k-1}} \tag{8.107}$$

The change in altitude, horizontal distance, and heading over each segment is:

$$\Delta h_k(t) = H_{PL}(V_{k-1}, \gamma_{k-1}, V_k, \gamma_k, t) \tag{8.108}$$

$$\Delta s_k(t) = S_{PL}(V_{k-1}, \gamma_{k-1}, V_k, \gamma_k, t) \tag{8.109}$$

$$\Delta \psi_k(t) = \Delta s_k(t)/R_k \tag{8.110}$$

These are used to determine the altitude and heading over time:

$$\begin{aligned} h_k(t) &= h_0 + \sum_{j=1}^{k} \Delta h_k(t) \\ \psi_k(t) &= \psi_0 + \sum_{j=1}^{k} \Delta \psi_k(t) \end{aligned} \tag{8.111}$$

Example Solutions

Consider the minimum-energy ascent for Scenario 2 in Figure 6.1, where the airship starts its ascent 250 km west of the target station. The same conditions for this scenario are repeated here and an alternative solution is generated using the winding ascent optimization described above.

A simple ascent plan is computed first. Ten different solutions are generated using random initial guesses and the lowest cost solution is chosen. In this scenario, all 10 solutions converge to the same structure, which has an approximate energy cost of 2.4 kW-hrs and a flight time of 4.8 hours. It takes 0.8 seconds to compute all 10 solutions.

Because the simple ascent solution has no cruise phase, a winding ascent plan is computed. The results of the simple ascent trajectory are used to seed the initial guess for the winding ascent optimization. The final time is set to 4.8 hours and the trajectory is divided into 6 segments. For each segment, the velocity is set to the simple ascent velocity of 2.4 m/s, the flight path angle is set to the maximum limit, and a zero inverse turn radius is used.

The direct ascent optimization terminates after 46 major iterations, requiring 950 evaluations of the cost and constraint functions, and takes 35.6 seconds. This is an enormous speed improvement over the full non-linear numerical optimization with SNOPT, which typically required 15-30 minutes to converge for all minimum-energy solutions.

The state and control time histories for this alternative solution are shown in Figure 8.18. Note the large difference between the wind-relative (airspeed) and Earth-relative velocities in the top-left plot. This clearly shows the significant contribution from the wind in its ascent to the station. The flight-path angle, though allowed to vary, is immediately increased to its maximum value and maintains that value throughout the flight. This agrees with the result found in the simple ascent energy approximation, where the energy is found to have an inverse relationship with the flight path angle. The altitude increases gradually, with a faster ascent at the end of the flight. This is most likely due to the reduced energy cost of flying at higher airspeeds in lower density air at high altitude.

The thrust is always less than 0.5 kN. Note that at the 1 hour mark, the thrust drops to zero then rises again. At this time, the thrust angle μ is rotated to -90 deg and held there for about 30 minutes, while the angle of attack increases to about 14 deg. This is the result of the minimum-thrust NDI control law of Eq. (8.38) being applied with a negative $\dot{V}_{des}$. At one point it is possible to achieve the specified $\dot{V}_{des}, \dot{\gamma}_{des}$ pair with zero thrust. Afterwards, α_c is increased so that the lift and drag forces are used and thrust continues to be minimized. The thrust angle jumps to -90 deg in order to keep $\dot{\gamma} = 0$ in the presence of upward lift.

The wind-relative motion in the east / up vertical plane is shown in Figure 8.19. The green lines show the direction and relative magnitude of the wind across altitude, while

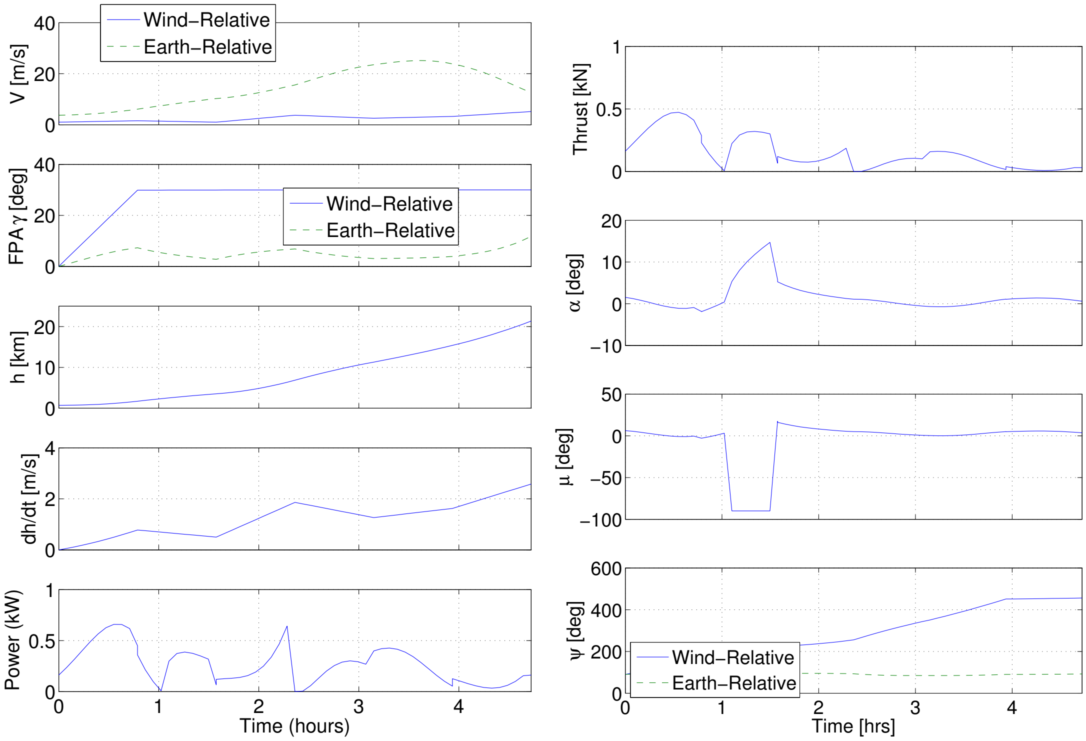

Figure 8.18: Scenario 2, State and Control History for Minimum Energy Solution using the Alternative Winding Ascent Optimization

the red lines show the airspeed velocity. Even though the airship travels 250 km to the east, it only flies 5 km on its own, with the wind taking it the vast majority of the distance.

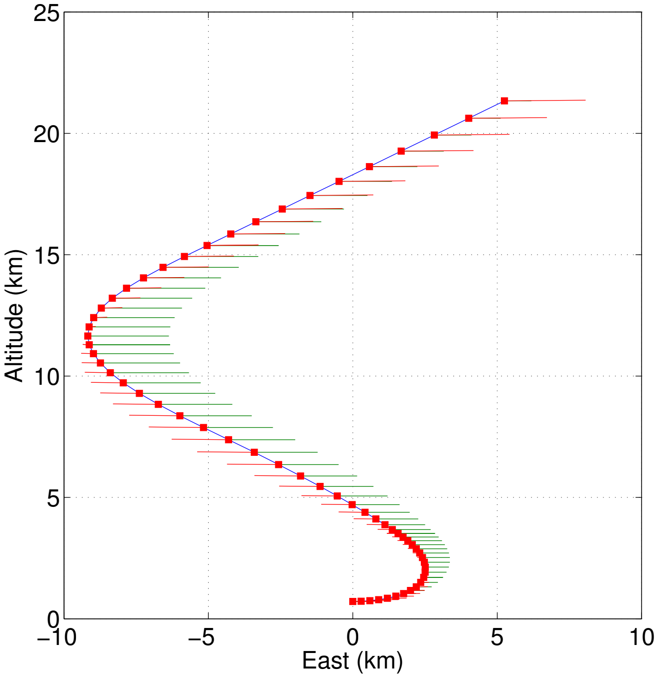

Figure 8.19: Scenario 2, Wind-Relative Motion in East / Up Plane

The wind-relative motion in the east / north horizontal plane is shown in Figure 8.20, along with a time history of the turning radius inverse. The motion starts in the east direction and turns south. The turn radius is at its smallest (highest $1/R$) initially, which can be seen in its path. The motion then approaches a straight line towards the southwest with a large turn radius (low $1/R$) before turning again north and east. Finally, it flies in a nearly straight line towards the east to end the flight.

The cumulative energy over time is plotted in Figure 8.21, and the altitude vs. east profile of the trajectory is plotted in Figure 8.22. The original solution from SNOPT is shown for comparison in both plots. The close agreement in these plots clearly shows that the alternative method is successfully finding a close approximation to the expected

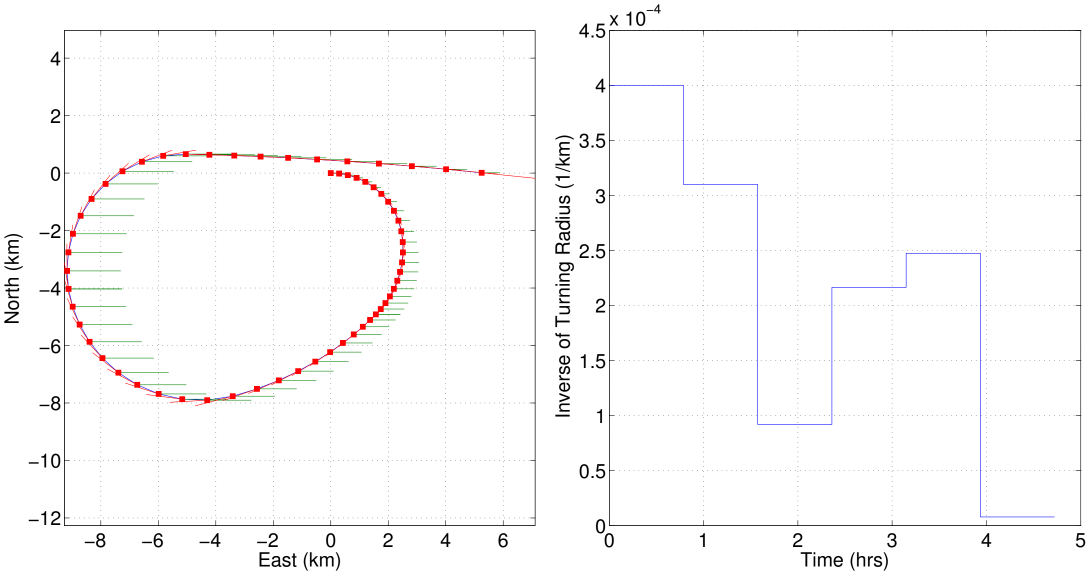

Figure 8.20: Scenario 2, Wind-Relative Motion in East / North Plane

optimal solution.

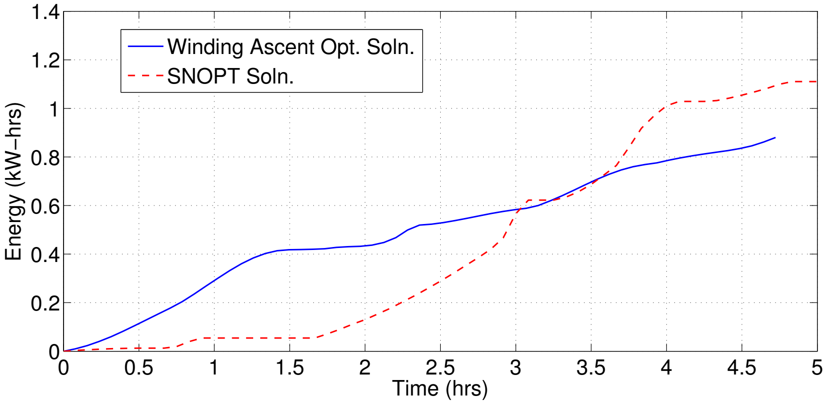

Figure 8.21: Scenario 2, Cumulative Energy History For the Winding Ascent Solution

3 Minimum-Energy Direct Ascent Profile, $\Delta t_C > 0$

The minimum energy solution for direct ascent may be approximated by constructing a series of trajectory segments with constant $\dot{V}$ and $\dot{\gamma}$. The trajectory consists of the

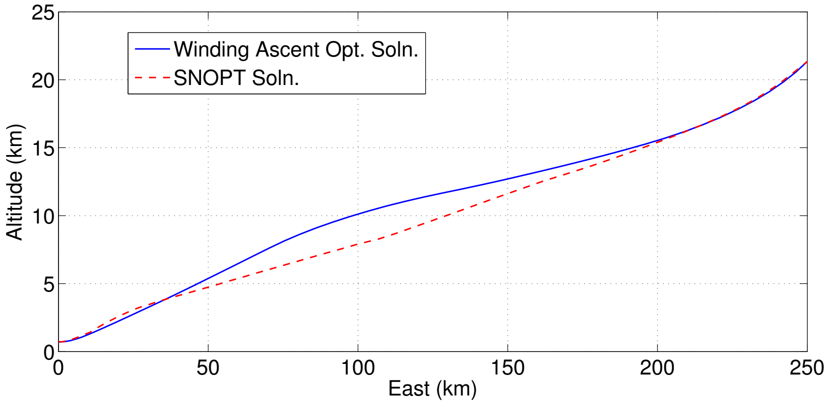

Figure 8.22: Scenario 2, Altitude vs. East Profile

following five segments:

Segment 0-1: Turn up to the maximum flight path angle.

Segment 1-2: Climb at the maximum flight path angle to a cruise altitude.

Segment 2-3: Turn down to zero flight path angle.

Segment 3-4: Cruise at constant altitude towards the target station.

Segment 4-5: Turn up/down to ascend/descend to the target altitude.

The diagram in Figure 8.23 describes the trajectory model. Variables shown in red are decision variables for the optimization problem. All other variables are computed implicitly. For some, the equations are simple enough to be shown in the diagram. Others, shown with a surrounding box, are computed from the equations presented below.

The total flight time is not fixed, but computed as the sum of each segment duration.

$$t_F = \Delta T_1 + \Delta T_2 + \Delta T_3 + \Delta T_4 + \Delta T_5$$

For the first segment, we transition from (V_0, h_0, γ_0) to (V_1, h_1, γ_1) over a time interval ΔT_1. With the initial conditions fixed, we select $\gamma_1 = \gamma_{\max}$ and solve for V_1 as a function of the parameters $\Delta T_1, h_1$.

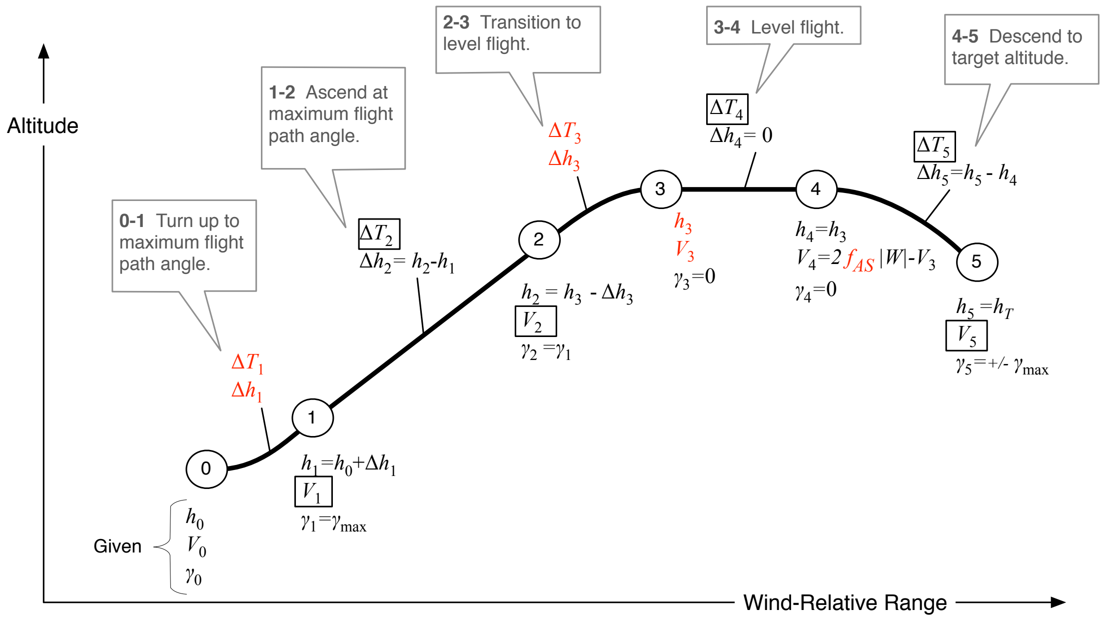

Figure 8.23: Profile of ascent trajectory with linear V, γ segments

$$
\begin{aligned}
b_1 &= (\gamma_1 - \gamma_0) / \Delta T_1 && (8.112) \\
a_1 &= \frac{b_1 \left[(h_1 - h_0) b_1 - V_0 (\cos\gamma_0 - \cos\gamma_1) \right]}{\sin\gamma_1 - \sin\gamma_0 - b_1 \Delta T_1 \cos\gamma_1} && (8.113) \\
V_1 &= V_0 + a_1 \Delta T_1 && (8.114)
\end{aligned}
$$

In the next segment, we climb to condition (V_2, h_2, γ_2). With a constant flight path angle, $b_2 = 0$ and the altitude equation is:

$$h_2 = h_1 + \frac{1}{2} \Delta T_2 \sin\gamma_1 (V_2 - V_1) \quad (8.115)$$

We can use Eq. (8.115) to compute the time interval ΔT_2 in terms of h_2 and V_2:

$$\Delta T_2 = 2 \frac{h_2 - h_1}{(V_2 - V_1) \sin\gamma_1} \quad (8.116)$$

Next, we compute the velocity V_2 necessary to transition from (h_2, γ_2) to (V_3, h_3, γ_3) over the time interval ΔT_3. Knowing that $a_3 = (V_3 - V_2)/\Delta T_3$ and $b_3 = (\gamma_3 - \gamma_2)/\Delta T_3$, we can use Eq. (8.88) to solve for V_2.

$$V_2 = V_3 - \frac{\frac{h_3 - h_2}{\Delta T_3}(\gamma_3 - \gamma_2)^2 - V_3(\gamma_3 - \gamma_2)(\cos\gamma_2 - \cos\gamma_3)}{\sin\gamma_3 - \sin\gamma_2 - \cos\gamma_2(\gamma_3 - \gamma_2)} \tag{8.117}$$

From point 3 to 4 in the trajectory is a constant altitude cruise, so $h_4 = h_3$ and $\gamma_3 = \gamma_4 = 0$. If the virtual target location before the cruise phase is already within the horizontal distance, then no horizontal cruise segment is needed. The coordinates of the virtual target before cruise are found by subtracting the east and north wind drift from the first three flight segments.

$$\Delta e_{0,3} = e_T - \sum_{k=1}^{3} \overline{W_E}(h_{k-1}, h_k) \tag{8.118}$$

$$\Delta n_{0,3} = n_T - \sum_{k=1}^{3} \overline{W_N}(h_{k-1}, h_k) \tag{8.119}$$

Similarly, the wind-relative horizontal range $\Delta s_{0,3}$ traversed by the airship during these segments is found by summing the range of each segment according to Eq. (8.91).

$$\Delta s_{0,3} = \sum_{k=1}^{3} \Delta s_{PL} V_{k-1}, \gamma_{k-1}, V_k, \gamma_k) \tag{8.120}$$

Again, if this range is greater than the distance to the virtual target, no horizontal cruise segment is applied and the result is: $\Delta T_4 = 0, V_4 = V_3$. Otherwise, the airspeed velocity at point 4 must be chosen to define the 3-4 flight segment. The average airspeed for the 3-4 flight segment is:

$$\bar{V}_{3,4} = \frac{1}{2}(V_3 + V_4)$$

Note that if the virtual target is in a direction opposite that of the wind velocity vector, then the airspeed must exceed wind velocity magnitude in order to guarantee that the target can be reached. We therefore set the average 3-4 flight segment velocity equal to the wind velocity magnitude multiplied by an *airspeed factor*, $f_{AS} \geq 0$.

$$\frac{1}{2}(V_3 + V_4) = f_{AS}\sqrt{W_E^2(h_4) + W_N^2(h_4)} \tag{8.121}$$

Rearranging to solve for V_4 gives:

$$V_4 = f_{AS}\sqrt{W_E^2(h_4) + W_N^2(h_4)} - V_3 \tag{8.122}$$

The bound on the airspeed factor is based on the direction of the wind compared to the direction of the virtual target.

$$f_{AS} \geq \begin{cases} 1 & W_E(h_3)\Delta e_{0,3} + W_N(h_3)\Delta n_{0,3} < 0 \\ 0 & \text{otherwise} \end{cases} \tag{8.123}$$

The final phase flight segment 4-5, which is a transition from level flight to the target altitude. Thus $h_5 = h_T$. The final flight path angle is set to the maximum, $\gamma_5 = \pm\gamma_{\max}$, where the sign depends on whether this segment is ascending or descending. First, the time interval ΔT_5 is selected by assuming constant velocity flight at a constant flight path angle. This is similar to Eq. (8.116). The expression is:

$$\Delta T_5 = \frac{h_5 - h_4}{V_4 \sin\gamma_5} \tag{8.124}$$

In the special case that $h_5 = h_4$, then $\Delta T_5 = 0$ and this segment vanishes. Otherwise, we have the following derivation for the final velocity V_5:

$$\begin{aligned} b_5 &= (\gamma_5 - \gamma_4)/\Delta T_5 && (8.125) \\ a_5 &= \frac{b_5\left[(h_5 - h_4)\,b_5 - V_4\left(\cos\gamma_4 - \cos\gamma_5\right)\right]}{\sin\gamma_5 - \sin\gamma_4 - b_5\Delta T_5\cos\gamma_5} && (8.126) \\ V_5 &= V_4 + a_5\Delta T_5 && (8.127) \end{aligned}$$

The problem formulation for minimum-energy direct ascent is written below. It includes 7 decision variables and 9 inequality constraints.

Minimum-Energy Problem Formulation - Direct Ascent, $h_C > 0$

$$\begin{aligned}
\min_{\Delta t_1,\Delta h_1,\Delta t_3,\Delta h_3,h_3,V_3,f_{AS}} \quad & E = \sum_{k=1}^{5} \int_{t_k}^{t_{k+1}} T_{Ck}(t) V_k(t) dt \\
\text{s.t.} \quad & V_{\min} \le V_j \le V_{\max} \quad \forall j \in \{1,2,3,4,5\} \\
& h_1 = h_0 + \Delta h_1 \\
& h_2 = h_3 - \Delta h_3 \\
& h_4 = h_3 \\
& h_5 = h_T \\
& \Delta e_0 = e_T - \sum_{k=1}^{3} \overline{W_E}(h_{k-1}, h_k) \\
& \Delta n_0 = n_T - \sum_{k=1}^{3} \overline{W_N}(h_{k-1}, h_k) \\
& f_{AS} \ge \begin{cases} 1 & W_E(h_3)\Delta e_{0,3} + W_N(h_3)\Delta n_{0,3} < 0 \\ 0 & \text{otherwise} \end{cases}
\end{aligned} \tag{8.128}$$

Example Solutions

Consider once again the minimum-energy ascent in Figure 6.1. This time we focus on Scenario 1, where the airship starts its ascent 20 km east of the target station. The same conditions for this scenario are repeated here and an alternative solution is generated using the direct ascent optimization method described above.

A simple ascent plan is computed first. Ten different solutions are generated using random initial guesses and the lowest cost solution is chosen. In this scenario, the best approach is to cruise at the maximum operational altitude of 24 km. Typically 3-5 of the 10 solutions converge to this structure, which has an approximate energy cost of 29 kW-hrs and a flight time of 18.4 hours. It takes 1.2 seconds to compute all 10 solutions.

The simple ascent plan has a cruise phase of 15.5 hours. Therefore, a direct ascent plan is computed. The results of the simple ascent trajectory are used to seed the initial guess for the direct ascent optimization. The cruise altitude was found to be $h_3 = h_C =$ 24 km, the cruise velocity was $V_3 = V_C = 6.68\ m/s$, and the climbing airspeed was $V = 4.94$ m/s. The initial guess for transition times $\Delta T_1, \Delta T_3$ are approximated as 5% of the total flight time, and the altitude changes $\Delta h_1, \Delta h_3$ are approximated with a linear V, γ profile for those transition times and given boundary velocities.

The direct ascent optimization terminates after 25 major iterations, requiring 305 evaluations of the cost and constraint functions, and takes 34.1 seconds. This is comparable with the winding ascent plan time. Once again, this provides a significant speed improvement over the original, larger optimization problem that used SNOPT.

The state and control time histories for this alternative solution are shown in Figure 8.24. The wind-relative heading is fixed so that it flies directly towards the virtual target, which in this case is due east. The thrust, thrust angle, and angle of attack controls are computed according to the minimum thrust control policy with NDI inner-loop control, according to Eq. (8.38). The velocity increases over the first two hours and reaches a steady value of 6.8 m/s. The thrust and power vary over the first two hours then remain fixed for the remainder of the flight, as the airship flies at constant velocity at 24 km. This is consistent with the minimum-energy state and control history from the original optimization using SNOPT.

The cumulative energy over time is plotted in Figure 8.25, and the altitude vs. east profile of the trajectory is plotted in Figure 8.26. The original solution from SNOPT is shown for comparison in both plots. Note that the original solution is for a 12 hour fixed flight time, while the new solution lasts for 15.5 hours. Once again, the close agreement in these plots indicates that the alternative optimization method is successfully finding a good approximation to the expected optimal trajectory.

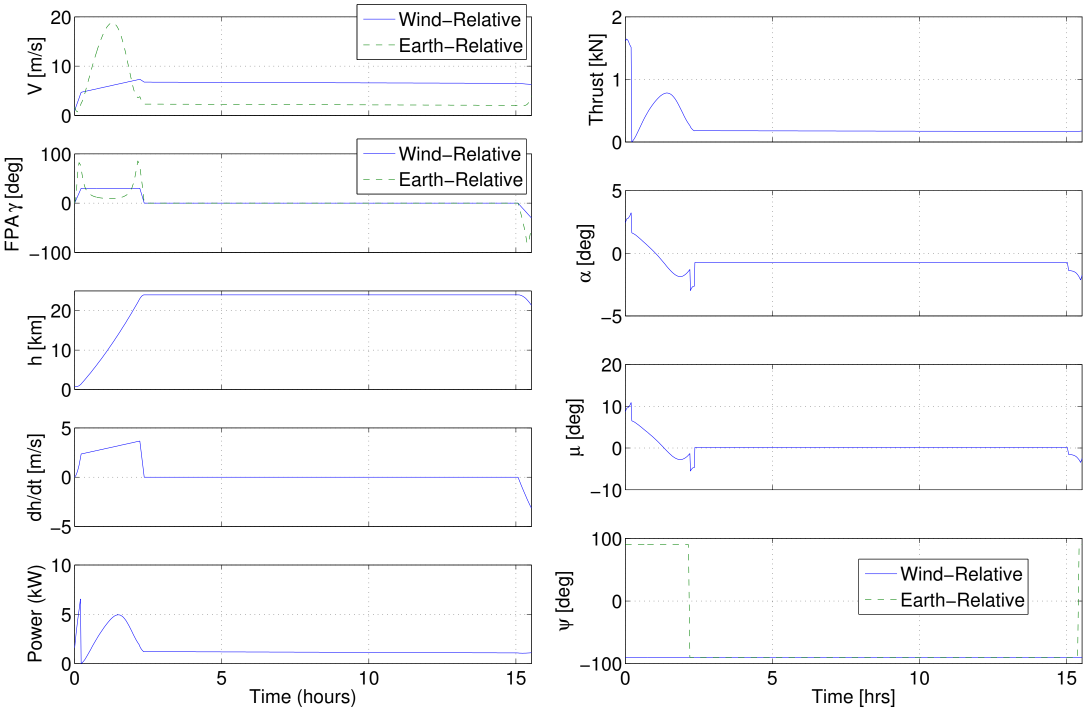

Figure 8.24: Scenario 1, State and Control History for Minimum Energy Solution using the Alternative Direct Ascent Optimization

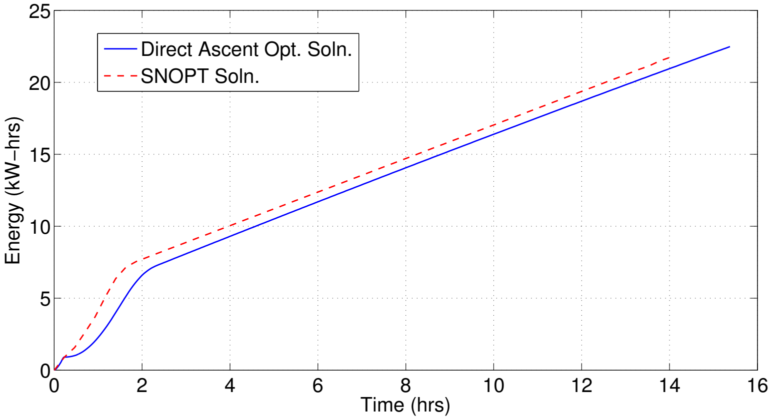

Figure 8.25: Scenario 1, Cumulative Energy History For the Direct Ascent Solution

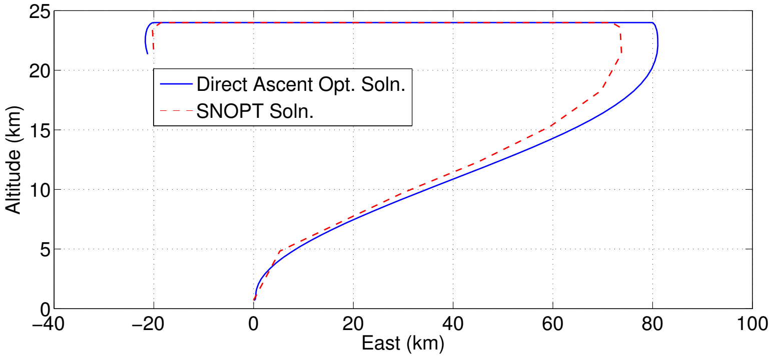

Figure 8.26: Scenario 1, Altitude vs. East Profile

Chapter 9

Conclusions

9.1 Summary

Stratospheric airships are an emerging class of autonomous, lighter-than-air vehicles. With the capability to maintain a fixed geographic station at much lower altitudes than satellites, these vehicles have the potential to perform a variety of long-term missions, such as wireless telecommunications; remote sensing for weather monitoring and scientific study; and imaging surveillance for traffic, border security, military operations and search and rescue missions. The recognition of this potential is evident in the recent widespread research and development of stratospheric airship platforms by academic, military and industrial institutions around the world.

Because of their extremely large surface area to mass ratio, airship flight dynamics are strongly influenced by the wind. A particular challenge for airship operation is the planning of ascent trajectories, as the slow moving vehicle must traverse the high speed winds of the jet stream. Due to the large changes in wind across altitude and the susceptibility of airship motion to wind, the optimization of ascent trajectories is important to ensure that the desired station is reached within acceptable performance bounds of flight time, energy consumption, and lateral excursion.

The goal of this thesis was to perform a systematic study of optimal ascent trajectories for stratospheric airships. A dynamic model of a generic airship configuration was developed to facilitate trajectory analysis and design. The equations of motion were derived for a point-mass model with aerodynamic lift and drag, buoyancy, thrust vector control, added mass effects, and wind rate accelerations. The environment models were developed, including polynomial fits for standard atmospheric density and a steady-state horizontal wind model with altitude dependence. A model for solar power generation was also developed, which describes the potential solar energy accumulation of solar cells on a portion of the hull as a function of latitude, time of the day, day of the year, and the airship orientation. Optimization problem formulations were then developed for both minimum time and minimum energy ascent flights. Numerical solutions were obtained through direct transcription and collocation of the original optimal control problem. Here the dynamics of the system are discretized at a finite number of points, so that the states and controls at each time become decision variables, and the dynamics form equality constraints.

This model was used as the basis for developing different sets of optimal ascent trajectories. Scenarios with fixed initial and final positions were considered and illustrate the range of solutions between minimum-time and minimum-energy flights. We then extended this formulation to study optimal trajectories over a range of initial conditions. This provided crucial insights into the effect of wind gradients, and revealed a general strategy for selecting the launch location.

Performance aspects of the optimal ascent trajectories were then analyzed. A solar production model was developed that includes seasonal and diurnal effects, hull geometry effects, atmospheric losses, and the attitude of the vehicle. This was used in combination with various optimal ascent trajectories to compute net energy profiles resulting from time-varying power production and consumption. It was found that some ascent trajectories, while optimized with respect to the given wind profile, led to significant reductions in power production due to the limited exposure of its top-mounted solar cells to the sun. A sensitivity analysis was also performed, where trajectory optimizations were re-computed across a range of drag coefficients and peak wind magnitudes. The flight time and total energy of the flights were found to change by only a few percent, and the optimal trajectories retained a consistent structure over all parameter values.

Finally, alternative methods were developed to more rapidly compute near-optimal ascent trajectories. This work was motivated by the need to quickly and reliably generate achievable trajectory plans for onboard implementation. The structures and characteristics of previously developed minimum-time and minimum-energy ascent trajectories were studied, which led to the development of simplified trajectory models. These models essentially capture the general structure of the expected optimal ascent, enabling an optimization over a small number of parameters to be performed quickly. Comparison of these alternative solutions to the original SNOPT solutions show excellent agreement, suggesting the alternate formulations are an effective means to develop near-optimal solutions in an onboard setting.

9.2 Contributions

This work provides the first complete study of modeling, trajectory optimization and proposed onboard guidance methods for stratospheric airships. In addition, it is among the first works to develop a dynamic model with buoyancy, added mass and wind rate terms, and to develop optimal trajectories for ascent. The key contributions are summarized below.

- The development and characterization of optimal ascent trajectories for stratospheric airships for minimum-time and minimum-energy flights.
- Sensitivity analysis of optimal solutions with respect to variations in drag and wind model characteristics.
- Modeling of solar irradiance exposure during ascent flights that account for time

of day, time of year, geographic latitude, altitude, and inertial orientation of the airship.

- Modeling of predicted wind profiles that are suitable for use in trajectory planning.
- The development of an ascent guidance method that is amenable for onboard implementation. This method enables computationally efficient re-planning of the optimal trajectory subject to changes in the predicted wind profile.

Chapter 10

Recommendations for Future Work

This thesis has established a foundational airship model and preliminary trajectory optimization results that can be expanded in several different ways. Recommendations for future work are summarized briefly below.

Analysis of the ascent trajectories found that ballast control uses about 10% of the total energy for minimum-energy flights. However, this energy consumption was neglected in the optimization. Adding a model of the power required for ballast control to the numerical optimization would enable us to minimize the total energy. It could also lead to different characteristics for minimum energy flights, as the power required for ballast control varies with altitude and climb rate.

The scope of trajectory optimization has been limited to ascent flights. It would be interesting to plan optimal descent flights using the same model. I suspect that the structure of optimal solutions identified for ascent flights would also be present in descent trajectories. For descent, however, additional altitude constraints would need to be enforced so that the airship only descends to the ground once it is sufficiently close to the landing site.

Long distance transfers between high-altitude stations is another interesting problem. Developing trajectories for a long-distance transfer would require the wind model to account for variations in the wind profile over latitude, longitude and time. A particularly interesting problem would be to utilize changes in the wind direction to cover large but bounded geographic areas with minimal energy.

The ascent trajectories computed in this thesis have been based on a few different representative wind profiles. The same planning methodologies can be applied with wind profiles that are based on real-time winds aloft data provided by NOAA (National Oceanic and Atmospheric Administration). This approach could be used with a set of potential wind profiles to determine the best initial heading and approximate flight duration. Alternatively, it would be interesting to develop a stochastic optimization technique that guarantees certain performance metrics, such as flight time or energy, remain within stated bounds subject to bounded changes in the assumed wind profile.

Finally, further work should be done to design and integrate a complete feedback control policy that tracks the commanded angle of attack and heading throughout the flight.

References

[1] G. A. Khoury and J. D. Gillett. *Airship Technology.* Cambridge Aerospace Series: 10, 1999.

[2] S. Lee and H. Bang. Three-Dimensional Ascent Trajectory Optimization for Stratospheric Airship Platforms in the Jet Stream. *Journal of Guidance, Control, and Dynamics*, 30(5):1341–1352, 2007. doi: 10.0731-5090/07.

[3] D. K. Schmidt, J. Stevens, and J. Roney. Near-Space Station-Keeping Performance of a Large High-Altitude Notional Airship. *Journal of Aircraft*, 44(2):611 – 615, April 2007. doi: 10.0021-8669/07.

[4] D. K. Schmidt. Modeling and Near-Space Stationkeeping Control of a Large High-Altitude Airship. *Journal of Guidance, Control, and Dynamics*, 30(2):540–547, 2007.

[5] A. Colozza. Initial Feasibility Assessment of a High Altitude Long Endurance Airship. Technical Report NASA CR-2003-212724, NASA, Dec. 2003.

[6] T. C. Tozer and D. Grace. High Altitude Platforms for Wireless Communications. *Electronics and Communications Journal*, 13(3):127–137, June 2001.

[7] C. Miller, J. Sullivan, and S. McDonald. High Altitude Airship Simulation Control and Low Altitude Flight Demonstration. In *AIAA Infotech@Aerospace 2007*

Conference and Exhibit, number AIAA 2007-2766, Rohnert Park, CA, May 2007. AIAA Infotech@Aerospace.

[8] Th. Lutz and S. Wagner. Drag Reduction and Shape Optimization of Airship Bodies. *Journal of Aircraft*, 35(3):345–351, 1997.

[9] S. Gomes and J. Ramos. Airship Dynamic Modeling for Autonomous Operation. In *IEEE International Conference on Robotics & Automation*, Leuven, Belgium, May 1998. IEEE.

[10] M. Battipede and P. Gil. Peculiar Performance of a New Lighter-Than-Air Platform for Monitoring. In *3rd Unmanned Unlimited Technical Conference, Workshop & Exhibit*, number AIAA-6448, Chicago, IL, Sep 20-22 2004.

[11] S. Lee, H. Lee, D. Won, and H. Bang. Backstepping Approach of Trajectory Tracking Control for the Mid-Altitude Unmanned Airship. In *AIAA Guidance, Navigation and Control Conference and Exhibit*, number AIAA-2007-6319, Hilton Head, SC, Aug. 2007.

[12] F. Repoulias and E. Papadopoulos. Dynamically feasible trajectory and open-loop control design for unmanned airships. In *Mediterranean Conference on Control & Automation*, pages 1–6, June 2007. doi: 10.1109/MED.2007.4433820.

[13] N. Rooz and E. Johnson. Design and Modelling of An Airship Station Holding Controller for Low Cost Satellite Operations. In *AIAA Guidance, Navigation, and Control Conference and Exhibit*, number AIAA-2005-6200, San Francisco, CA, Aug. 2005.

[14] J. Kim, J. Keller, and V. Kumar. Design and verification of controllers for airships. In *IEEE/RSJ International Conference on Intelligent Robots and Systems*, volume 1, pages 54–60, Oct. 2003. doi: 10.1109/IROS.2003.1250605.

[15] E. Hygounenc and P. Soueres. Automatic airship control involving backstepping techniques. In *IEEE International Conference on Systems, Man and Cybernetics*, Oct. 2002.

[16] Y. J. Zhao, W. L. Garrard, and J. B. Mueller. Benefits of Trajectory Optimization in Airship Flights. In *AIAA 3rd "Unmanned Unlimited" Technical Conference, Workshop and Exhibit*, pages 1–14, 2004.

[17] J. B. Mueller, Y. J. Zhao, and W. L. Garrard. Optimal Ascent Trajectories for Stratsospheric Airships Using Wind Energy. *Journal of Guidance, Control, and Dynamics*, 32(4):1232–1245, July–Aug 2009.

[18] A. Colozza. Airships for Planetary Exploration. Technical Report NASA/CR-2004-213345, NASA, Nov 2004.

[19] Ely de Paiva José Azinheira, Alexandra Moutinho. Airship Hover Stabilization Using a Backstepping Control Approach. *Journal of Guidance, Control, and Dynamics*, 29(4):903–914, 2006.

[20] E. de Paiva, F. Benjovengo, S. Bueno, J. Azinheira, and A. Moutinho. Nonlinear Control Approaches for an Autonomous Unmanned Robotic Airship. In *7th AIAA ATIO Conf, 2nd CEIAT Int'l Conf on Innov. and Integr. in Aero. Sciences,17th LTA Systems Tech. Conf.*, Belfast, Northern Ireland, Sep. 2007.

[21] S. Sharma, E.A. Kulczycki, and A. Elfes. Trajectory generation and path planning for autonomous aerobots. In *Jet Propulsion Lab., California Inst. of Technology*, Pasadena, CA, 2007. NASA Jet Propulsion Laboratory.

[22] S. Hima and Y. Bestaoui. Motion generation on trim trajectories for an autonomous underactuated airship. In *4th International Airship Convention and Exhibition* , Cambridge England, July 2002.

[23] T. Kampke and A. Elfes. Optimal aerobot trajectory planning for wind-based opportunistic flight control. In *IEEE/RSJ International Conference on Intelligent Robots and Systems*, volume 1, pages 67–74, Oct. 2003.

[24] J. B. Mueller and Y. J. Zhao. Development of an Aerodynamic Model and Control Law Design for a High-Altitude Airship. In *AIAA 3rd "Unmanned Unlimited" Technical Conference, Workshop and Exhibit*, number AIAA-6479, Chicago, IL, 2004. AIAA.

[25] L. B. Tuckerman. Inertia factors of ellipsoids for use in airship design. NACA Report No. 210, 1926.

[26] U.S. Standard Atmosphere, 1976. Technical Report (NOAA-S/T 76-15672): Supt. of Docs., US Govt. Print. Off.(Stock No. 003-017-00323-0), National Oceanic and Atmospheric Administration, Washington, DC, 1976.

[27] A. E. Hedin, E. L. Fleming, A. H. Manson, F. J. Schmidlin, S. K. Avery, R. R. Clark, S. J. Franke, G. J. Fraser, T. Tsuda, F. Vial, and R. A. Vincent. Empirical Wind Model for the Upper, Middle and Lower Atmosphere. *Journal of Atmospheric and Terrestrial PhysicsVolume*, 58(13):1421–1447, Sep. 1996.

[28] Horizontal Wind Model, HWM-93. `http://uap-www.nrl.navy.mil/uap/`.

[29] H. Wang, B. Song, and L. Zuo. Effect of High-Altitude Airship's Attitude on Performance of its Energy System. *Journal Of Aircraft*, 44(6):2077–2079, 2007.

[30] J.T. Betts. Survey of numerical methods for trajectory optimization. *Journal of Guidance, Control, and Dynamics*, 21(2):193–207, 1998.

[31] D. Hull. Conversion of Optimal Control Problems Into Parameter Optimization Problems. *Journal of Guidance, Control, and Dynamics*, 20(1):57–60, 1997.

[32] A.L. Herman and B.A. Conway. Direct Optimization Using Collocation Based on High-Order Gauss-Lobatto Quadrature Rules. *Journal of Guidance, Control, and Dynamics*, 19:592–599, 1996.

[33] P. E. Gill, W. Murray, and M. A. Saunders. SNOPT: An SQP Algorithm for Large-Scale Constrained Optimization. *SIAM Journal of Optimization*, 12:979–1006, 2002.

[34] R. Walterscheid. High-Altitude Wind Prediction and Measurement Technology Assessment. Technical Report ATR-2009(5427)-1, Aerospace Corporation, 2009.

[35] MM5 Community Model, May 2010. `http://www.mmm.ucar.edu/mm5/`.

[36] The Weather Research and Forecasting Model, May 2010. `http://www.wrf-model.org`.

Appendix A

Glossary and Acronyms

This appendix defines various terms and acronyms that are used throughout the thesis.

A.1 Glossary

- **Ascent Cone** - A right circular cone with its vertex at the airship, representing a geometric region that can only be accessed by varying the heading.
- **Ballonet** – An airbag contained within the exterior envelope of the airship. An airship uses ballonets to regulate buoyancy. Ballast air is pumped into the ballonet to increase vehicle weight, and it is pumped out to reduce the vehicle weight.
- **Virtual Target** (**VT**) – The coordinates of the target station for the airship defined in a wind-relative frame. This is a predicted target after applying the expected cumulative drift from the wind.

A.2 Acronyms

Table A.1: Acronyms

Acronym	Meaning
ENU	East-North-Up coordinate frame
HWM	Horizontal Wind Model
LTA	Lighter-than-air
NDI	Nonlinear dynamic inversion
SNOPT	Sparse Nonlinear Optimization
VT	Virtual Target

Appendix B

Wind Prediction Model

This appendix summarizes the model used in this thesis for predicting wind profiles.

In order to plan the airship's ascent trajectory, some prediction must be made of the future winds to be encountered across different altitudes. The current wind profile may be estimated using radar equipment or rapid ascent balloons [34]. However, these methods may not be available, and even if they are, the winds may change from this initial estimate by the time the airship reaches higher altitudes. In order to develop the best possible prediction of winds aloft in real-time, existing wind modeling tools may be used, such as the Mesoscale Model 5 [35] and the Weather and Research Forecast (WRF) Model [36]. While these models have been found to provide a precision as good as 5 m/s up to 20 km altitude [34], it is not known if they are suitable for a real-time, onboard implementation.

Rather than focusing on a particular forecasting approach, the present objective is to develop a representative model of a wind prediction method. From the perspective of the guidance system, it is important that the wind prediction model has: 1) periodic updates of the predicted wind profile during ascent, and 2) model mismatch between the predicted and true wind profiles. In this section, we develop a relatively simple method for computing and updating a predicted wind profile during ascent by incorporating recorded measurements of the wind speeds across altitude.

The east and north components of the predicted wind profile are modeled as independent polynomial functions of altitude. A weighted least squares solution is used to compute the polynomial coefficients of each component of the wind model. Let $\boldsymbol{w} \in \mathbb{R}^N$ be a vector of wind velocity data over an altitude range contained in $\boldsymbol{h} \in \mathbb{R}^N$. Define the non-dimensional altitude matrix $H \in \mathbb{R}^{N \times P}$ as:

$$H = \left[\begin{array}{cccccc} \bar{\boldsymbol{h}}^P & \bar{\boldsymbol{h}}^{P-1} & \cdots & \bar{\boldsymbol{h}} & \mathbf{1}_N \end{array} \right] \tag{B.1}$$

where the non-dimensional altitude vector is $\bar{\boldsymbol{h}} = \boldsymbol{h}/d_C$, the exponents are applied element-wise to each vector, and $\mathbf{1}_N$ is an N-length vector of all 1's. We wish to find a vector of polynomial coefficients $\boldsymbol{p} \in \mathbb{R}^P$ that satisfies the equation:

$$UH\boldsymbol{p} = U\bar{\boldsymbol{w}} \tag{B.2}$$

where $\bar{\boldsymbol{w}} = \boldsymbol{w}/v_c$ is the non-dimensional wind data, and $U \in \mathbb{R}^{P \times P}$ is a diagonal weighting matrix whose elements on the diagonal are selected to prioritize the fitting of the model at certain altitudes over others. The solution for $\boldsymbol{p}$ is obtained by pre-multiplying both sides by H^T then inverting the linear system of equations, as follows:

$$H^T U H \boldsymbol{p} = H^T U \bar{\boldsymbol{w}} \tag{B.3}$$

$$\boldsymbol{p} = \left(H^T U H\right)^{-1} H^T U \bar{\boldsymbol{w}} \tag{B.4}$$

Note that this solution requires the $(H^T U H)$ matrix to be full rank.

At the start of the flight, the initial polynomial coefficients are selected to fit the best available prediction of the wind profile. As the airship ascends, wind measurements are recorded at regular altitude intervals. Consider the airship at some altitude h_k where the k^{th} wind measurement is recorded, and denote the total number of recorded measurements as $N_m < N$. The complete wind data vector to be fit includes two separate components, combining both measurements and predictions. The wind data vector and associated altitude vector are defined as:

$$\bar{\boldsymbol{w}} = \begin{bmatrix} \bar{\boldsymbol{w}}_{\boldsymbol{m}} \\ \bar{\boldsymbol{w}}_{\boldsymbol{p}} \end{bmatrix}^T \qquad \bar{\boldsymbol{h}} = \begin{bmatrix} \bar{\boldsymbol{h}}_{\boldsymbol{m}} \\ \bar{\boldsymbol{h}}_{\boldsymbol{p}} \end{bmatrix}^T \tag{B.5}$$

where $\bar{\boldsymbol{w}}_{\boldsymbol{m}} \in \mathbb{R}^{N_m}$ is the recorded array of normalized wind measurements for altitudes $\bar{\boldsymbol{h}}_{\boldsymbol{m}}$, and $\bar{\boldsymbol{w}}_{\boldsymbol{p}} \in \mathbb{R}^{N_p}$ is the remaining set of predicted (normalized) winds for altitudes $\bar{\boldsymbol{h}}_{\boldsymbol{p}}$. Note that the measurement altitude vector contains values up to h_k, while the prediction altitude vector is for $h_k < h \leq h_F$. Also, before any measurements are taken, $N_m = 0, N_p = N$, and $\bar{\boldsymbol{w}} = \bar{\boldsymbol{w}}_{\boldsymbol{p}}$.

The objective of the wind prediction model is to closely match the current wind measurement data, while providing a prediction of the wind profile for future altitudes ($h > h_k$) that changes gradually as measurements are added. The weighting matrix U is used to achieve this behavior by prioritizing the fitting of certain measurement and prior prediction data points over others. In particular, we place the highest weight on the current and most recent measurements, reducing the weights for measurements at lower altitudes. For predictions, we ramp up the weights as the altitude approaches the target altitude. These trends are captured precisely in the definition of the j^{th} diagonal element:

$$U(j,j) = \begin{cases} u_1 \left(\frac{h(j)-h(1)}{h(N_m)-h(1)} \right)^{q_1} & j \in [1, N_m] \\ u_2 \left(\frac{h(j)-h(N_m+1)}{h(N)-h(N_m+1)} \right)^{q_2} & j \in [N_m+1, N] \end{cases} \tag{B.6}$$

where u_1 and u_2 are scalar parameters that define the largest weight for measurements and predictions, respectively. Similarly, the exponents q_1 and q_2 determine the rate at which the weights change with altitude. The example in Figure B.1 illustrates the separate variations of the weights for measurement and prediction data across altitude.

The altitude vector is predefined with N increments from the launch site up to the target station. Let the superscript (k) index the measurement taken when altitude h_k in this vector is reached. The polynomial wind models for each component of the horizontal wind are updated according to the following steps.

Figure B.1: Variation of Weights in U for Measurement and Prediction Data Across Altitude

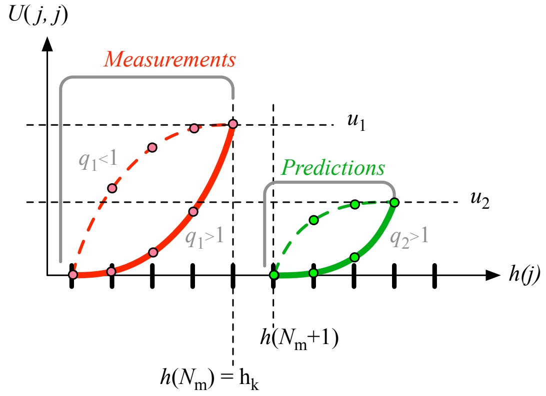

1. Increment the number of measurements, N_m and update the U matrix using Eq. (B.6).

2. Append the new measurement data to the wind measurement vector

$$\bar{\boldsymbol{w}}_{\boldsymbol{m}}{}^{(k)} = \left[\ \bar{\boldsymbol{w}}_{\boldsymbol{m}}{}^{(k-1)},\quad \bar{w}_m^{(k)}\ \right]^T \tag{B.7}$$

3. Update the wind prediction vector for upper altitudes. In general, the new prediction is based upon the previous model $\boldsymbol{p}^{(k-1)}$ and current measurements $\bar{\boldsymbol{w}}_{\boldsymbol{m}}{}^{(k)}$.

$$\bar{\boldsymbol{w}}_{\boldsymbol{p}}{}^{(k)} = F(\boldsymbol{p}^{(k-1)}, \bar{\boldsymbol{w}}_{\boldsymbol{m}}{}^{(k)}) \tag{B.8}$$

4. Recompute the wind prediction model using Eq. (B.4).

$$\boldsymbol{p}^{(k)} = \left(H^T U H\right)^{-1} H^T U \begin{bmatrix} \bar{\boldsymbol{w}}_{\boldsymbol{m}}{}^{(k)} \\ \bar{\boldsymbol{w}}_{\boldsymbol{p}}{}^{(k)} \end{bmatrix}$$

The third step in this process involves updating the wind prediction vector for higher altitudes based upon the current model and recent wind measurements during flight. This particular step in the process may be best accomplished by utilizing sophisticated weather models, such as the MM5 or WRF discussed previously in this section. However, the implementation of these methods and the development of any new forecasting methods is beyond the scope of this work. Because our present goal is to evaluate the effect of wind model mismatch, we define the wind prediction vector as the true wind plus some error. The following formulation is used:

$$\bar{\boldsymbol{w}}_{\boldsymbol{p}}{}^{(k)} = (\alpha_k)\,\bar{\boldsymbol{w}}_{\boldsymbol{T}} + (1-\alpha_k)\,\bar{\boldsymbol{w}}_{\boldsymbol{p}}{}^{(k-1)} \tag{B.9}$$

where $\bar{\boldsymbol{w}}_{\boldsymbol{T}}$ is the true wind and $0 \leq \alpha_k \leq 1$ is a weighting parameter that can be varied across altitude. For the present analysis, we choose $\alpha_k = k/N$, which allows the predicted wind speeds to steadily approach the true values as the airship ascends. At the final altitude where a wind measurement is taken before reaching the station, we have $k = N$, $\alpha_N = 1$ and $\bar{\boldsymbol{w}}_{\boldsymbol{p}}{}^{(N)} = \bar{\boldsymbol{w}}_{\boldsymbol{T}}$.